Full-Wave Simulation of High-Frequency Electromagnetic Propagation Through Inhomogeneous Plasma

Thomas Williams

Doctor of Philosophy

UNIVERSITY OF YORK

PHYSICS

SEPTEMBER 2014

Abstract

The propagation of EM radiation past wavelength-sized inhomogeneities is not well understood, yet is of importance for both microwave heating and diagnostic applications in tokamaks. The work presented in this thesis improves this understanding; for this purpose, EMIT-3D, a new finite-difference time-domain (FDTD) code implementing a cold-plasma model has been written to extend full-wave simulations of propagation in magnetized plasmas to 3D. The numerical development of the algorithm is presented and supported with a new stability analysis.

Studies of propagation past density filaments ('blobs') are presented and compared with 2D simulations. The synergistic effects of blob density and width on scattering angle are investigated, resulting in the conclusion that even filaments of densities below beam critical density can cause significant deviation in beam paths over a wide frequency range. Further to this, the case of oblique incidence is an explicitly 3D interaction, and its effects have been calculated.

The broadening and defocusing effect on microwave beams caused by realistic edge turbulence, observed in all magnetic fusion devices, is also investigated. A fluid model for edge turbulence is used to produce realistic turbulent profiles, which in turn are used to initialise a set of microwave propagation simulations. The effect of propagation through a turbulent layer is observed even at low fluctuation amplitude, and observed to have a peak when eddy sizes approach beam wavelength.

This work supports MAST experiments using the SAMI diagnostic to image microwave emission from the plasma edge due to mode conversion from electron Bernstein waves; however, it has relevance for numerous microwave diagnostic, heating and current drive applications in plasmas.

Contents

List of Figures

Acknowledgements

I would like to thank: Roddy Vann and Martin O'Brien for your knowledge, enthusiasm and patience in supervising me. All of my colleagues past and present at the York Plasma Institute for providing a superb learning and working environment over the last four years. Everyone else who has been part of the Fusion Doctoral Training Network. Alf Köhn for being a great collaborator and host.

The UK EPSRC and the European Communities under the contract of Association between EURATOM and CCFE for funding this work, as well as the University of York for granting me a teaching scholarship.

Every student I had the pleasure of tutoring; the experience will stay with me and I hope at least some of the material stays with you! Alnegator and Samba York for the many opportunities to make noise in a controlled fashion. Everyone involved in the Sun Dome project; keep spreading the word!

My parents Julie and Nick for having taught me to be curious in the first place and for giving me 27 years of love and support. Lastly, Oju Akinyemi for always being on my team and giving me the strength to make it through the most difficult parts. I truly appreciate everything.

Declaration

I declare that the work presented in this thesis, except where it is otherwise stated, is based on my own research and has not been submitted previously for a degree in this or any other university. Parts of the work presented in this thesis have been published in:

T.R.N. Williams, A. Köhn, M.R. O'Brien and R.G.L. Vann, "*Propagation in 3D of microwaves through density perturbations*", Plasma Physics and Controlled Fusion **56**, 075010 (2014)

The simulation results in Chapters 5 and 6 which I did not obtain personally were produced by Alf Köhn (2D full-wave results from Chapter 5 generated using the code IPF-FDMC) and Jarrod Leddy (turbulent density profiles from Chapter 6 generated using the code BOUT++). These were obtained as part of a collaboration which I initiated and helped to direct.

Chapter 1

Introduction

1.1 Magnetic confinement fusion

1.1.1 Context and basic concept

The economically sustainable production of energy from a controlled nuclear fusion reaction has been the objective of an international research effort for 65 years. Most research has focused on the D-T reaction between deuterium and tritium due to its relatively high cross-section:

$$ {}^{2}_{1}\mathrm{D} +^{3}_{1} \mathrm{T} \rightarrow {}^{4}_{2}\mathrm{He} +^{1}_{0} \mathrm{n} + 17.6\mathrm{MeV} \tag{1.1} $$

In a fusion device, the goal of ignition is achieved when this reaction becomes self-sustaining - sufficient heating to maintain the required temperature is provided by the α particles and external heating is no longer required. This will occur under the condition that the product of number density n, temperature T and energy confinement time τ_E satisfies the inequality [1]

$$ nT\tau_E > 5 \times 10^{21}\mathrm{m}^{-3}\mathrm{keVs} \tag{1.2} $$

One of the two principal approaches to fusion energy is that of magnetic confinement fusion (MCF); the D-T fuel is heated to $T \sim 10\mathrm{keV}$ and thus ionised to form a plasma, which is confined using strong magnetic fields in order to achieve the necessary τ_E. Although ignition has not yet been achieved in this way, continued advances in device design, engineering, materials science, diagnostics and theoretical understanding have seen incremental progress made towards this goal. The ITER device, currently under construction, is expected to achieve $Q = 10$; that is, an output power ten times greater than the input power, an important step towards ignition.

1.1.2 The tokamak

ITER, along with other, smaller experimental devices already in operation, uses the tokamak design, a toroidal configuration first devised in the 1950s. A current is passed through a central solenoid, which acts as the primary circuit in a transformer, causing a change in magnetic flux through the torus and hence inducing a toroidal current through a plasma within the tokamak vessel; in addition to heating the plasma ohmically, this generates a poloidal magnetic field, shown schematically in Figure 1.1. External poloidal field coils are used to add an additional poloidal component for greater control over the position and shaping of the plasma.

External toroidal field coils are used to add a toroidal magnetic field component, resulting in a helical field. This confines the plasma while avoiding the consequences of fundamental particle drifts which had reduced the confinement of earlier devices. The ions and electrons confined in a tokamak with a purely toroidal field, due to the field gradient in the radial direction, will experience a $\nabla \mathbf{B}$ drift in opposite vertical directions [2], setting up a vertical electric field which results in an $\mathbf{E} \times \mathbf{B}$ drift in the radial direction. This results in a large net loss of particles radially outwards from the device. This is avoided with a helical field; since the top and bottom of the plasma are connected by fieldlines, particles will flow along them to balance any vertical $\nabla \mathbf{B}$ drift and prevent an electric field being established.

This field structure allows a magnetohydrodynamic (MHD) equilibrium to be achieved, supporting a pressure gradient in the plasma which results in a sufficiently

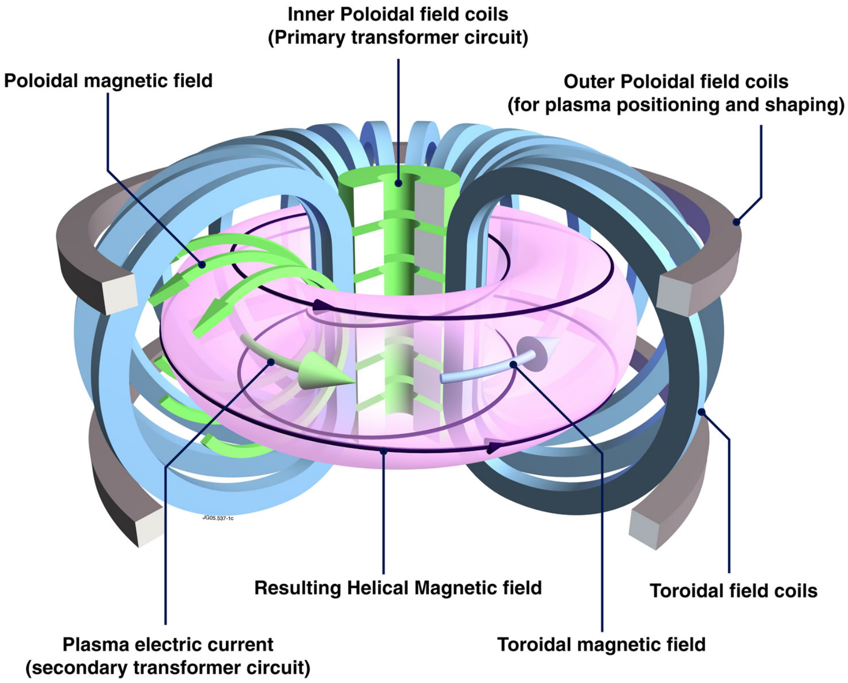

Figure 1.1: Schematic of the electromagnetic fields and coils of the JET tokamak, showing the resulting helical magnetic field. Image taken from EFDA

high core temperature for fusion.

MHD equilibrium, once achieved, is threatened by numerous classes of instability driven by the steep gradients of the plasma, which can reduce energy and particle confinement, cause damage to structural components and lead to disruptions which end the tokamak pulse. A great deal of research, both experimental and theoretical, has focused on the understanding, mitigation and control of instabilities to achieve a longer-lasting equilibrium.

1.1.3 The spherical tokamak

While ITER has a ‘conventional’ aspect ratio (ratio of major radius to minor radius of the torus) of ~ 3, alternative tokamak designs have been produced with aspect ratios of half this or less, as shown in Figure 1.2. The outboard last closed flux surface of the plasma therefore approaches the shape of a sphere, giving these designs the name of ‘spherical tokamak’ or ST.

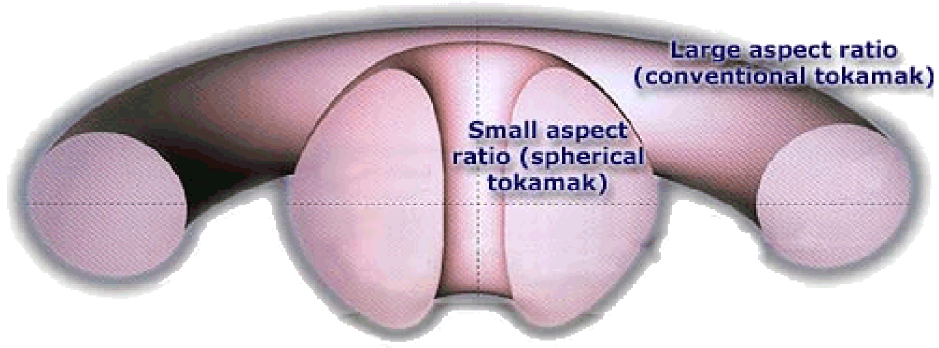

Figure 1.2: Schematic of conventional and spherical tokamak aspect ratios. Image taken from UKAEA

The low aspect ratio design allows operation at a higher β, or ratio of plasma pressure to magnetic pressure:

$$\beta = \frac{nk_BT}{(B^2/2\mu_0)} \tag{1.3}$$

This was predicted by theoretical scalings implying that a combination of low aspect ratio and high plasma shaping maximise the achievable β, and has been verified experimentally over a wide range of tokamaks [3].

This has the consequence that a given temperature and pressure can be achieved using a significantly smaller magnetic field, making such a device more economical to build and operate; in addition, the compact structure is cheaper to construct and the spherical geometry provides inherent suppression of certain instabilities.

The ST was first proposed in the 1980s by Peng and Strickler [4]; a number have been constructed globally, including START at Culham Centre for Fusion Energy (CCFE) in the UK, superseded by MAST, the Mega-Amp Spherical Tokamak, in 1999. MAST, presently undergoing a major upgrade, achieves toroidal β (calculated using the volume-averaged plasma pressure and value of B at the plasma's geometric centre) $\sim$ 3 times those in conventional aspect ratio tokamaks, with a relatively low magnetic field, high flow shear and strong variation in toroidal field across the minor radius. This has allowed the testing of theory in new operational regimes and provided new insight into tokamak physics [5].

1.2 The tokamak plasma edge

1.2.1 Confinement modes

Additional heating and current drive beyond that generated ohmically can be supplied by the use of either radio frequency antennas or the injection of energetic neutral particles. It has been observed, beginning in the early 1980s [6], that under certain conditions, as the heating power is increased, a transition takes place from the standard low-confinement (L) mode to high-confinement (H) mode. An edge transport barrier is formed, impeding the flow of particles across the plasma boundary and supporting steep ‘pedestal’ gradients in temperature and pressure at the plasma edge [7]; the resulting difference in density profiles is sketched in Figure 1.3. The pedestal supports higher core temperatures and pressures which causes an increase in the confinement time by a factor of two [8]; the usefulness of this for achieving reactor conditions mean that H-mode is now seen as the most likely operating scenario for future tokamak experiments and reactors (including ITER).

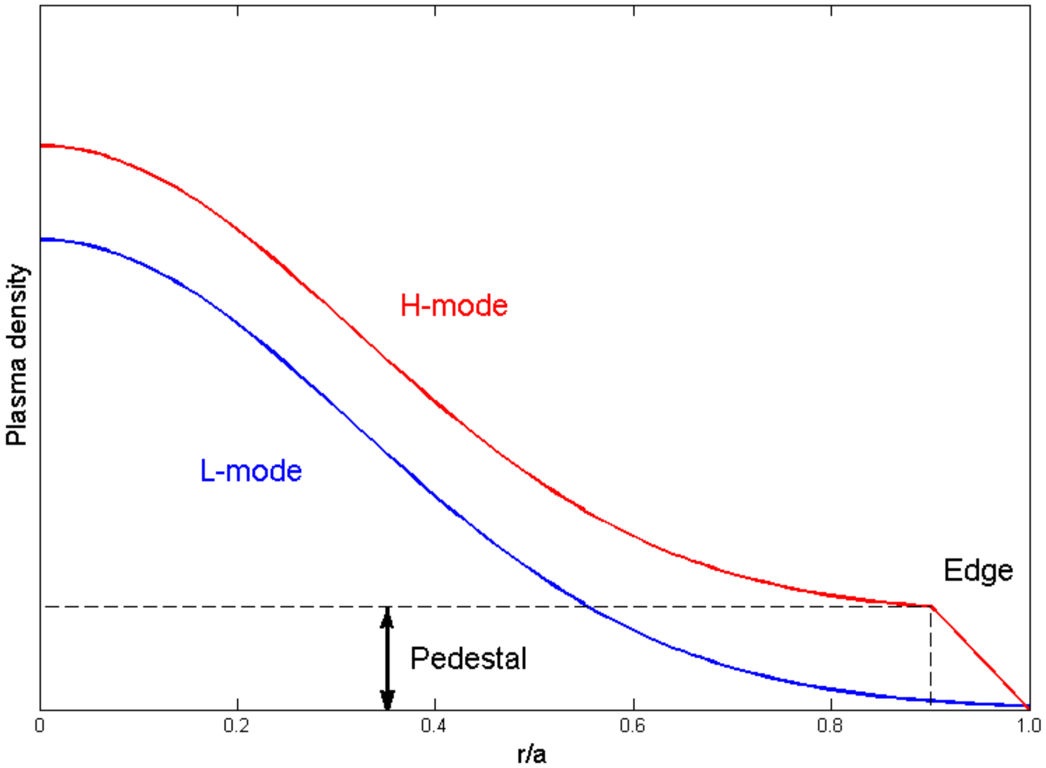

Figure 1.3: Sketch of L and H-mode density profiles along a radial cut from the core to the edge of the tokamak where a is its minor radius; pedestal shown

1.2.2 Edge localised modes

However, the steep edge pressure gradient in H-mode makes the plasma susceptible to instabilities known as edge localised modes (ELMs). These are transient bursts from the edge on a microsecond timescale, and can occur repeatedly during H-mode. ELMs are problematic for several reasons: they create extremely high transient heat loads on plasma-facing components such as the divertor [9], and are associated with a loss of confinement since energy is lost from the plasma.

The heat loading issue becomes more serious with the larger ELMs which will be present on ITER, presenting a significant engineering challenge in constructing materials to withstand them. Experimental studies have found strong evaporation of divertor materials including the currently planned tungsten, leading to significant erosion over the reactor's lifetime [10].

A theoretical understanding of the causes of ELMs will be crucial in developing techniques to mitigate or suppress them, but is incomplete at present. At present, the role of the current density (**J**) profile at the edge is thought to be important, but measuring it experimentally at the required spatial and temporal resolution is extremely challenging. A system for making routine measurements of the edge **J** profile would provide much-needed data to constrain future ELM models.

1.2.3 Filaments and turbulence

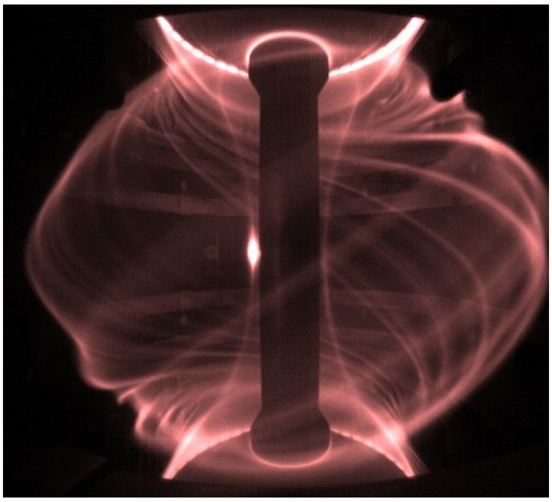

Figure 1.4: Fast camera (visible spectrum) image of MAST filaments. Image taken from UKAEA

ELMs have a filamentary structure which tends to follow the magnetic field-lines, but there is also evidence for the presence of filamentary blob structures between ELMs and in L-mode at the edge of nearly all tokamaks, as well as alternative toroidal configurations such as stellarators and reversed-field pinches; they are thought to be responsible for a significant fraction of cross-field transport at the edge of fusion-relevant plasmas [11]. They have been observed between ELMs on MAST, where extensive experimental work has been carried out to characterise their structure and properties [12]. Fast camera diagnostics have enabled these detailed studies - see Figure 1.4.

More generally, edge turbulence has been commonly observed on tokamaks and other devices for many years, with similar characteristics in all cases [13]. Perpendicular to the magnetic field, turbulent fluctuations have length scales in the 'drift wave' range of scales (~ 0.1 — 10 cm) and frequencies (~ 10 — 1000 kHz); parallel length scales are on the order of tens of metres, meaning that the general structure of edge turbulence is close to that of 2D filaments.

The amplitude of this turbulence can be extremely high, with $\delta n/n \sim 1$ — 100%, and thus it can have important consequences. Theoretical models relating this turbulence to drift wave dynamics, with a multi-scale distribution of $\mathbf{E} \times \mathbf{B}$ velocity perturbations driven by the free energy from steep background pressure gradients [14], have had success in explaining many features of tokamak edge turbulence, but direct comparison of theory to experiment is still difficult due to the complex nonlinear physics involved.

1.3 Microwave diagnostics

1.3.1 Electron cyclotron emission

Electron cyclotron diagnostics rely on the emission from electron gyrations around magnetic field lines in the plasma. For harmonics which allow the plasma to be treated as optically thick, the intensity per unit frequency of this emission is directly proportional to the plasma electron temperature T_e [2]:

$$I(\omega) = \frac{\omega^2 T_e(R)}{8\pi^3 c^2} \tag{1.4}$$

This technique is used widely as a diagnostic for temperature in fusion devices. A 1D ECE diagnostic can provide a radial temperature profile. Further, by analysing the emitted spectrum to find the frequencies at which cutoffs (explained in Section 2.1.4) occur, a radial profile of electron density n_e can be inferred [15]. In the last 10 years, ECE systems have been developed using arrays of detectors which allow 2D images of T_e and n_e to be obtained. These have been used to study edge temperature and density fluctuations on the TEXTOR [16], KSTAR [17] and ASDEX Upgrade [18] tokamaks - see Figure 1.5.

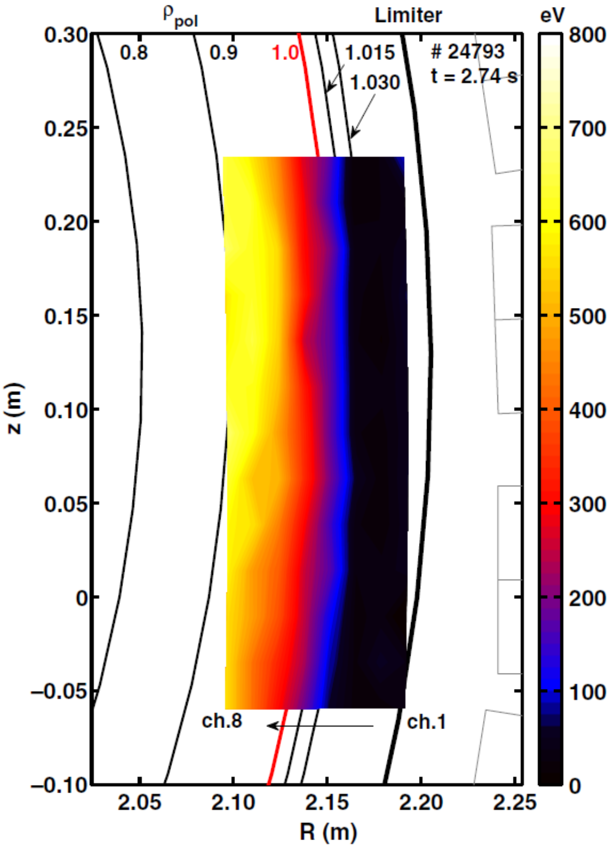

Figure 1.5: A 2D edge T_e map from ASDEX Upgrade during an inter-ELM period, superimposed on calculated equilibrium flux surfaces (separatrix labelled as 1.0). Obtained using 2D ECE imaging [18]

However, in a spherical tokamak, due to the low field and high plasma density, the high-density cutoff for the O-mode microwave emission generally lies outside the resonances at which cyclotron emission is generated, preventing it from being imaged outside the plasma. This makes such diagnostics difficult to operate and sometimes useless.

1.3.2 Synthetic aperture microwave imaging

A diagnostic known as SAMI (Synthetic Aperture Microwave Imaging) has been developed in order to take advantage of microwave emission due to mode conversion from electron Bernstein waves (EBWs) [19]. For further details on this physical process, see Chapter 2.

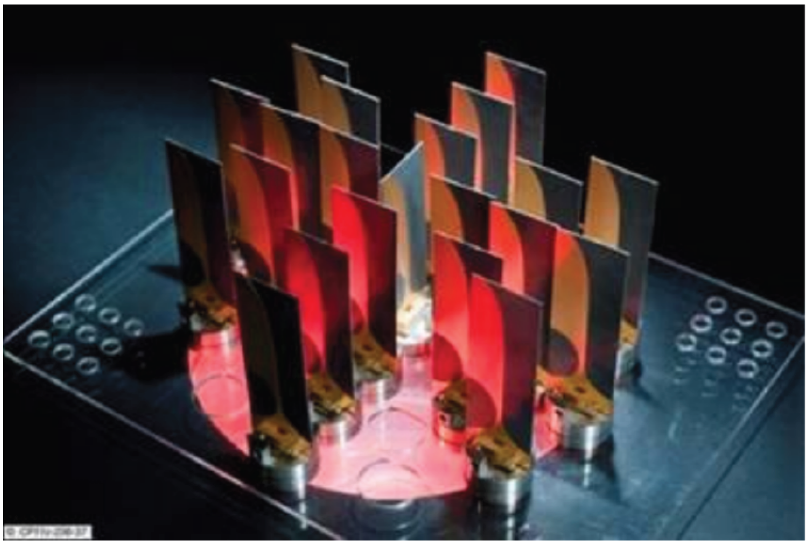

Figure 1.6: SAMI array of 21 antipodal Vivaldi antennas [19]

SAMI uses an aperture synthesis technique, with phase differences compared between an array of receiving antennas (using no optical components - the layout is shown in Figure 1.6) in order to obtain a map in Fourier space of microwave emission. This is then converted to a 2D image in real space.

Installed on MAST, this diagnostic produces high time-resolution ($\sim 10\mu$s) images of O-mode emission due to EBWs generated at EC harmonics in the plasma core. These are measured in the 10 - 35 GHz range, with a sub-range of these frequencies corresponding to a radial position through the plasma edge [20].

The eventual aim of these measurements is to obtain highly time- and spatially-resolved measurements of the plasma edge **J**-profile in order to constrain and test predictive theoretical models of ELM onset. This is possible since the emission is coplanar with the electron density profile and background magnetic field vector.

Since density profiles can be measured accurately using diagnostics such as Thomson scattering, the magnetic fieldline pitch can be deduced at a range of radii. The toroidal field strength is known and hence the poloidal field profile can be extracted from this. This allows an edge **J**-profile to be calculated.

However, large fluctuations have been observed in the measured signal during inter-ELM periods; these demand explanation. A candidate for the cause of these fluctuations is the scattering effect of inter-ELM filaments.

This is the original motivation for the development of the code described in this thesis. Beyond this, it has developed into a framework for the investigation of the interaction between microwaves and multiple types of plasma inhomogeneity (filaments, turbulence, magnetic shear, electron flows).

Chapter 2 explains the background physics underpinning most of the work in this thesis. Chapter 3 provides some background information on the numerical techniques used, while Chapter 4 uses them to develop a new method and presents a stability analysis. Chapters 5 and 6 contain results from two investigations of different classes of plasma inhomogeneity and Chapter 7 draws conclusions and looks ahead to future work in this vein.

Chapter 2

Electromagnetic waves in cold plasma

In this chapter, the theory underpinning the work in this thesis is introduced and developed. First, the cold plasma dispersion relation is derived, and used to obtain the dispersion relations for the electromagnetic O and X-modes as well as the conditions for conversion between these modes. A discussion of warm plasma modes is also presented, with the electrostatic electron Bernstein mode covered. An understanding of these modes provides the necessary background for the following chapters.

2.1 Waves in cold plasmas

2.1.1 The ionosphere

Historically, the development of "cold plasma" or "magneto-ionic" theory has been motivated by the problem of radio wave propagation in the ionosphere [21]. This is the region, $\sim 50 - 1000$ km above the Earth's surface, in which cosmic and solar radiation cause sufficient ionisation to atmospheric gases in order to affect the dispersion of radio waves. Generally, for frequencies below 30 MHz its presence is essential for propagation, as the lower ionosphere and ground act as a waveguide; however, at frequencies above 50 MHz used in satellite communications, it can be a source of error as the signal loses coherence due to scattering from ionospheric inhomogeneities [22].

From the original formulation of the theory in the 1920s and 30s, an explanation was sought for the reflection and scattering processes affecting a radio wave as it propagates into the ionosphere. This was achieved, with parameters being the local values of electron and ion density and Earth's magnetic field strength, as well as the frequency, polarization and angle of propagation of the wave. An early account of this can be found in Appleton (1932) [23]. It was found that the thermal motion and resulting finite Larmor radius of the electrons can be neglected for most ionospheric applications, with this "cold plasma" approximation reproducing the principal modes of propagation and their cutoffs.

Since the first successful attempts to heat a magnetically confined plasma with RF antennas in the 1960s [24], magneto-ionic theory has been applied to problems of propagation and mode conversion of EM waves in magnetised fusion plasma. Although it does not provide for absorption mechanisms such as cyclotron harmonic damping, it retains broad applicability in many cases.

2.1.2 The plasma frequency

During the derivation of the cold plasma dispersion relation, the electron and ion plasma frequencies ω_{pe} and ω_{pi} become significant and so it is helpful to discuss them first.

A plasma consisting of electrons and a single ion species, assumed to be quasineutral ($n_i \simeq n_e \equiv n$) over macroscopic lengthscales, is considered. Any perturbation of one species away from this quasineutral starting position will result in an accumulation of charge, creating an electric field which provides a restoring force, leading to an oscillation at the plasma frequency.

Since an electron has a mass at least three orders of magnitude lower than any ion, the timescales over which the two species accelerate and thus oscillate are different enough that the species not being considered can be treated as a static neutralising background.

To illustrate the plasma oscillation: if a slab of electrons are displaced by a distance x, a surface charge density $\sigma = nex$ builds up on the face of the slab which is furthest in the x-direction due to accumulation of negative charge. The space left behind the slab no longer contains electrons and hence is positively charged; a charge density $\sigma = -nex$ therefore builds up on the opposite face.

This charge separation results in an electric field $E_x = -nex/\varepsilon_0$ within the slab. Applying Newton's second law to an electron in the slab therefore results in a simple harmonic oscillator equation:

$$m_e \frac{d^2x}{dt^2} = \frac{-ne^2x}{\varepsilon_0} \tag{2.1}$$

with the solution

$$x(t) = x_0 \cos(\omega_{pe}) \tag{2.2}$$

where

$$\omega_{pe} = \left(\frac{ne^2}{\varepsilon_0 m_e}\right)^{(1/2)} \tag{2.3}$$

This analysis can be repeated for ion species, resulting in the ion plasma frequency:

$$\omega_{pi} = \left(\frac{nZ^2e^2}{\varepsilon_0 m_i}\right)^{(1/2)} \tag{2.4}$$

where Z is the ion atomic number.

2.1.3 The dispersion relation

The analysis in this section draws from that found in several reference books [25, 26, 27]. We consider a plasma containing electrons and a single species of ions, confined by an equilibrium background magnetic field $\mathbf{B}_0$ of arbitrary strength and orientation.

We begin with Maxwell's equations, which are written in full here for later reference:

$$\nabla \cdot \mathbf{E} = \frac{\rho}{\varepsilon_0} \tag{2.5}$$

$$\nabla \cdot \mathbf{B} = 0 \tag{2.6}$$

$$\nabla \times \mathbf{E} = -\frac{\partial \mathbf{B}}{\partial t} \tag{2.7}$$

$$\nabla \times \mathbf{B} = \mu_0 \mathbf{J} + \mu_0 \varepsilon_0 \frac{\partial \mathbf{E}}{\partial t} \tag{2.8}$$

We now linearise Equations 2.7 and 2.8. The equilibrium $\mathbf{B}_0$-field is assumed to be uniform so $\frac{\partial \mathbf{B}_0}{\partial t} = 0, \nabla \times \mathbf{B}_0 = 0$. Perturbed quantities are written without subscripts.

We also assume plane-wave solutions, i.e. that $\mathbf{E}, \mathbf{B} \sim \exp(i(\mathbf{k} \cdot \mathbf{r} - \omega t))$, so $\nabla \to i\mathbf{k}$ and $\frac{\partial}{\partial t} \to -i\omega$.

We therefore obtain

$$\mathbf{k} \times \mathbf{E} = \omega \mathbf{B} \tag{2.9}$$

$$\mathbf{k} \times \mathbf{B} = -i\mu_0 \mathbf{J} - \frac{\omega}{c^2}\mathbf{E} \tag{2.10}$$

The relation between **J** and **E** is expressed using the conductivity tensor $\underline{\underline{\sigma}}$, modifying Equation 2.10:

$$\mathbf{J} = \underline{\underline{\sigma}} \cdot \mathbf{E} \tag{2.11}$$

$$\Rightarrow \mathbf{k} \times \mathbf{B} = -i\mu_0 \underline{\underline{\sigma}} \cdot \mathbf{E} - \frac{\omega}{c^2}\mathbf{E} \tag{2.12}$$

The dielectric permittivity tensor $\underline{\underline{\varepsilon}}$ is defined as follows:

$$\underline{\underline{\varepsilon}} = \underline{\underline{I}} + \frac{i}{\varepsilon_0 \omega}\underline{\underline{\sigma}} \tag{2.13}$$

So we can write

$$\mathbf{k} \times \mathbf{B} = -\frac{\omega}{c^2}\underline{\underline{\varepsilon}} \cdot \mathbf{E} \tag{2.14}$$

Substituting in Equation 2.9 for **B**, we obtain:

$$\left[\mathbf{kk} - k^2 \underline{\underline{I}} + \frac{\omega^2}{c^2}\underline{\underline{\varepsilon}}\right] \cdot \mathbf{E} = \underline{\underline{M}} \cdot \mathbf{E} = 0 \tag{2.15}$$

A solution exists where $\det\left(\underline{\underline{M}}\right) = 0$.

Now, $\underline{\underline{\sigma}}$ and hence $\underline{\underline{\varepsilon}}$ must be evaluated. To do this, the relation between **J** and **E** in a non-relativistic approximation to a cold plasma must be found. Starting with the linearised fluid equations of motion for electrons and ions (of atomic number Z) in a plasma and neglecting the pressure and collision term, we obtain:

$$m_e \frac{\partial \mathbf{v}_e}{\partial t} = -e\left(\mathbf{E} + \mathbf{v}_e \times \mathbf{B}_0\right) \tag{2.16}$$

$$m_i \frac{\partial \mathbf{v}_i}{\partial t} = Ze\left(\mathbf{E} + \mathbf{v}_i \times \mathbf{B}_0\right) \tag{2.17}$$

We decompose these into Cartesian components and let $\mathbf{B}_0$ be in the z-direction, without loss of generality. As before, we let $\frac{\partial}{\partial t} \rightarrow -i\omega$. First, for the electrons:

$$v_{xe} = -\frac{ie}{\omega m_e}\left[E_x + v_{ye}B_0\right] \tag{2.18}$$

$$v_{ye} = -\frac{ie}{\omega m_e}\left[E_y - v_{xe}B_0\right] \tag{2.19}$$

$$v_{ze} = -\frac{ie}{\omega m_e}E_z \tag{2.20}$$

Solving for v_{xe} and v_{ye}:

$$v_{xe} = -\frac{ie}{\omega m_e}\frac{\left[E_x + i\frac{\omega_{ce}}{\omega}E_y\right]}{\left[1 - \left(\frac{\omega_{ce}}{\omega}\right)^2\right]} \tag{2.21}$$

$$v_{ye} = -\frac{ie}{\omega m_e}\frac{\left[E_y - i\frac{\omega_{ce}}{\omega}E_x\right]}{\left[1 - \left(\frac{\omega_{ce}}{\omega}\right)^2\right]} \tag{2.22}$$

where the electron cyclotron frequency $\omega_{ce} = -\frac{eB_0}{m_e}$.

Repeating this analysis for the ions yields:

$$v_{xi} = \frac{iZe}{\omega m_i}\frac{\left[E_x + i\frac{\omega_{ci}}{\omega}E_y\right]}{\left[1 - \left(\frac{\omega_{ci}}{\omega}\right)^2\right]} \tag{2.23}$$

$$v_{yi} = \frac{iZe}{\omega m_i}\frac{\left[E_y - i\frac{\omega_{ci}}{\omega}E_x\right]}{\left[1 - \left(\frac{\omega_{ci}}{\omega}\right)^2\right]} \tag{2.24}$$

$$v_{zi} = \frac{iZe}{\omega m_i}E_z \tag{2.25}$$

where $\omega_{ci} = \frac{ZeB_0}{m_i}$.

Now, to obtain the plasma current $\mathbf{J}$, we multiply these velocities by the density and charge of their respective species and sum over both species; that is,

$$\mathbf{J} = Zen_{0i}\mathbf{v}_i - en_{0e}\mathbf{v}_e \tag{2.26}$$

So for J_x, substituting in the plasma frequencies $\omega_{pe}^2 = \frac{n_{0e}e^2}{\varepsilon_0 m_e}$ and $\omega_{pi}^2 = \frac{n_{0i}Z^2e^2}{\varepsilon_0 m_i}$, we obtain

$$\frac{i}{\varepsilon_0\omega}J_x = -\frac{\omega_{pi}^2}{\omega^2}\frac{\left[E_x + i\frac{\omega_{ci}}{\omega}E_y\right]}{\left[1-\left(\frac{\omega_{ci}}{\omega}\right)^2\right]} - \frac{\omega_{pe}^2}{\omega^2}\frac{\left[E_x + i\frac{\omega_{ce}}{\omega}E_y\right]}{\left[1-\left(\frac{\omega_{ce}}{\omega}\right)^2\right]} \tag{2.27}$$

At this point, we make the reasonable approximation that $\omega \gg \omega_{ci}$, since we are interested in higher frequencies. Hereafter ion motion is neglected altogether. With some algebraic identities, this becomes

$$\frac{i}{\varepsilon_0\omega}J_x = -\frac{\omega_{pe}^2}{2\omega^2}\left[\left(\frac{\omega}{\omega+\omega_{ce}} + \frac{\omega}{\omega-\omega_{ce}}\right)E_x + \left(\frac{\omega}{\omega-\omega_{ce}} - \frac{\omega}{\omega+\omega_{ce}}\right)iE_y\right] \tag{2.28}$$

and, for y and z:

$$\frac{i}{\varepsilon_0\omega}J_y = -\frac{\omega_{pe}^2}{2\omega^2}\left[\left(\frac{\omega}{\omega+\omega_{ce}} + \frac{\omega}{\omega-\omega_{ce}}\right)E_y + \left(\frac{\omega}{\omega+\omega_{ce}} - \frac{\omega}{\omega-\omega_{ce}}\right)iE_x\right] \tag{2.29}$$

$$\frac{i}{\varepsilon_0\omega}J_z = -\frac{\omega_{pe}^2}{\omega^2}E_z \tag{2.30}$$

We now have the relation between $\mathbf{J}$ and $\mathbf{E}$ in all 3 dimensions, giving us the conductivity tensor $\underline{\underline{\sigma}}$ and hence the dielectric permittivity:

$$\begin{aligned}\underline{\underline{\varepsilon}} &= \underline{\underline{I}} + \frac{i}{\varepsilon_0\omega}\underline{\underline{\sigma}} \\ &= \begin{pmatrix} S & -iD & 0 \\ iD & S & 0 \\ 0 & 0 & P \end{pmatrix}\end{aligned} \tag{2.31}$$

where

$$\begin{aligned}
R &= 1-\frac{\omega_{pe}^2}{\omega^2}\left(\frac{\omega}{\omega+\omega_{ce}}\right)\\
L &= 1-\frac{\omega_{pe}^2}{\omega^2}\left(\frac{\omega}{\omega-\omega_{ce}}\right)\\
P &= 1-\frac{\omega_{pe}^2}{\omega^2}\\
S &= \frac{R+L}{2}, D=\frac{R-L}{2} \qquad (2.32)
\end{aligned}$$

If the direction of $\mathbf{B}_0$ is made arbitrary, and a vector cyclotron frequency with components $(\omega_{ce,x}, \omega_{ce,y}, \omega_{ce,z})$ is introduced, this can be written in general tensor form:

$$\varepsilon_{ij} = \delta_{ij} - \frac{\omega_{pe}^2}{\omega^2-\omega_{ce}^2}\left(\delta_{ij} - \omega_{ce,i}\omega_{ce,j}/\omega^2 + i\varepsilon_{ijk}\omega_{ce,k}/\omega\right) \qquad (2.33)$$

where δ_{ij} and ε_{ijk} are the Kronecker delta and Levi-Civita symbols respectively. We now reinstate our assumption that $\mathbf{B_0} = B_0\hat{\mathbf{z}}$, and substitute Equation 2.31 into Equation 2.15 to obtain $\underline{\underline{M}}$:

$$\begin{aligned}
\underline{\underline{M}} &= \left[\mathbf{kk} - k^2\underline{\underline{I}} + \frac{\omega^2}{c^2}\underline{\underline{\varepsilon}}\right]\\
&= \begin{pmatrix} k_x^2-k^2+\frac{\omega^2}{c^2}S & k_xk_y - i\frac{\omega^2}{c^2}D & k_xk_z \\ k_yk_x + i\frac{\omega^2}{c^2}D & k_y^2-k^2+\frac{\omega^2}{c^2}S & k_yk_z \\ k_zk_x & k_zk_y & k_z^2-k^2+\frac{\omega^2}{c^2}P \end{pmatrix} \qquad (2.34)
\end{aligned}$$

Now, we also choose $\mathbf{k}$ to be in the xz plane, so that $k_y = 0$, and define θ to be the angle between $\mathbf{k}$ and $\hat{\mathbf{z}}$. We then define a vector $\mathbf{n}$, with magnitude equal to the refractive index n:

$$\mathbf{n} = \frac{\mathbf{k}c}{\omega} \qquad (2.35)$$

$$\Rightarrow n_x = n\sin\theta, n_y = 0, n_z = n\cos\theta \tag{2.36}$$

Multiplying $\underline{\underline{M}}$ by $\frac{c^2}{\omega^2}$, using the identity $\cos^2\theta + \sin^2\theta = 1$ and substituting for **n** in Equation 2.34 gives

$$\underline{\underline{M}} = \begin{pmatrix} S - n^2\cos^2\theta & -iD & n^2\sin\theta\cos\theta \\ iD & S - n^2 & 0 \\ n^2\sin\theta\cos\theta & 0 & P - n^2\sin^2\theta \end{pmatrix} \tag{2.37}$$

Solutions of Equation 2.15 exist where $\det\left(\underline{\underline{M}}\right) = 0$. Some algebraic manipulation results in equations in $\sin^2\theta$ and $\cos^2\theta$, which can be divided through and factored to give the cold plasma dispersion relation

$$\tan^2\theta = \frac{-P\left(n^2 - R\right)\left(n^2 - L\right)}{\left(Sn^2 - RL\right)\left(n^2 - P\right)} \tag{2.38}$$

2.1.4 Cold plasma modes

Several distinct wave modes can then be obtained from this model; here, we will classify those propagating either parallel or perpendicular to the magnetic field. Modes have *cutoffs* (i.e. enter a region of evanescence and are unable to propagate further) in the case where $n \to 0$ and *resonances* (i.e. are absorbed, although the cold plasma theory does not provide a physical mechanism for absorption) in the case where $n \to \infty$.

To find the two modes which propagate parallel to B_0 we set $\theta = 0$, which can be seen to result in the following:

$$n_{\|}^2 = R, L = 1 - \frac{\omega_{pe}^2}{\omega^2}\left(\frac{\omega}{\omega \pm \omega_{ce}}\right) \tag{2.39}$$

These are the right- and left-handed circularly polarised modes respectively. This can be seen from their eigenvectors in the matrix equation; $(E_x, iE_x, 0)$ for R-polarised and $(E_x, -iE_x, 0)$ for L. Their respective cutoffs lie where

$$\omega = \frac{1}{2}\left([4\omega_{pe}^2 + \omega_{ce}^2]^{1/2} \pm \omega_{ce}\right) \tag{2.40}$$

and, since ω_{ce} was defined as negative, the R-polarisation has a resonance at $\omega = \omega_{ce}$. This is the electron cyclotron resonance, where the electric field of the wave oscillates with the same frequency and in the same direction as electrons gyrating in the equilibrium magnetic field, leading to strong absorption. The L-polarised wave does not experience this resonance since it oscillates in the opposite direction to the electrons' gyromotion.

To investigate perpendicular propagation, we set $\theta = \pi/2$, giving first, straightforwardly,

$$n_\perp^2 = P = 1 - \frac{\omega_{pe}^2}{\omega^2} \tag{2.41}$$

with eigenvector $(0, 0, E_z)$. This is therefore a transverse wave, linearly polarised with its electric field vector parallel to $\mathbf{B}_0$ and the particle motions therefore unaffected. This mode is known as the ordinary or O-mode, and is essentially light-like, with its dispersion modified by the dielectric property of the plasma. This is plotted in Figure 2.1.

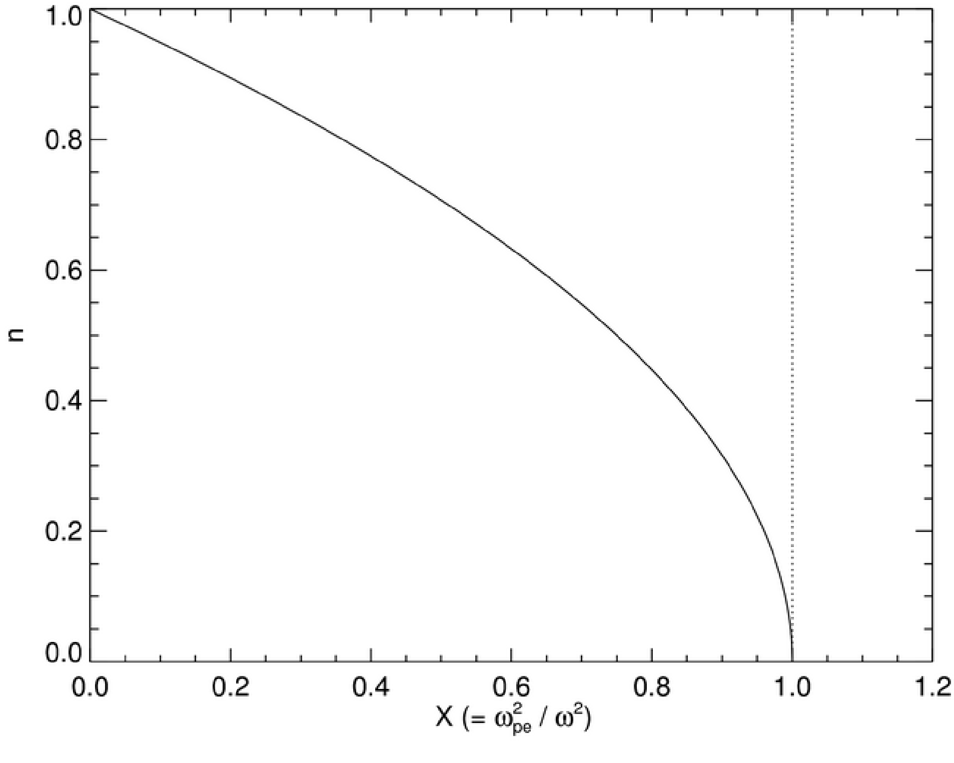

Figure 2.1: O-mode dispersion relation (see Equation 2.41) where wave vector $\mathbf{k} \perp \mathbf{B_0}$. Refractive index n plotted against squared ratio of plasma frequency to wave frequency. High density cutoff shown by dotted line.

The O-mode encounters a cutoff where $\omega = \omega_{pe}$. As $\omega_{pe} \propto n_e^{1/2}$, this has the result that an O-mode of given frequency propagating into a plasma of increasing density will reach a critical density n_c at which it is reflected. This fact is exploited by some plasma diagnostic techniques such as reflectometry [28], in which the phase shift of reflected radiation at a range of frequencies is used to determine the position of a range of density layers.

This cutoff can cause problems of accessibility for techniques such as electron cyclotron resonance heating (ECRH), where an O-mode wave is injected into the plasma edge to heat cyclotron harmonics. These are the layers in the plasma at which the resonance condition $\omega = n\omega_{ce}$ where n is a non-zero integer is satisfied (for O-mode, this resonance does not appear in the cold plasma theory, but will if finite Larmor radius effects are taken into account - see section 2.2.1).

As $\omega_{ce} \propto B_0$, the relative positions of the cyclotron resonances and the O-mode cutoff in the plasma depend on the ratio of n_e to B_0^2. This can be obtained from the plasma parameter beta, the ratio of plasma pressure to magnetic pressure; $\beta \propto \frac{n_e}{B_0^2}$.

Spherical tokamaks run at high beta, which carries advantages for economical operation but results in the O-mode cutoff typically lying outside the harmonic, closer to the edge, preventing the wave from penetrating. As an example, on MAST, the high beta requires ECRH absorption at the fifth or sixth harmonic [29], at which the damping is very low, which introduces additional complications and has motivated the development of alternative heating schemes using electron Bernstein waves (EBWs) [30].

Likewise, electron cyclotron emission (ECE) diagnostics, which detect the radiation emitted at cyclotron harmonics to measure plasma temperature, are less effective in spherical tokamaks since the emitted radiation is unable to propagate out from the plasma. This problem has motivated the development of electron Bernstein wave diagnostics [31].

Returning to the case of perpendicular propagation and carrying out some further algebra, another mode with the dispersion relation

$$n_\perp^2 = \frac{RL}{S} = \frac{\left(1 - \frac{\omega_{pe}^2}{\omega^2} - \frac{\omega_{ce}}{\omega}\right)\left(1 - \frac{\omega_{pe}^2}{\omega^2} + \frac{\omega_{ce}}{\omega}\right)}{\left(1 - \frac{\omega_{pe}^2}{\omega^2} - \frac{\omega_{ce}^2}{\omega^2}\right)} \tag{2.42}$$

is obtained. Its eigenvector is $\left(E_x, -\frac{iS}{D}E_x, 0\right)$, meaning that its electric field is perpendicular to the equilibrium field but the wave is partly transverse and partly longitudinal. This results in an elliptical polarisation, varying according to the ratio $\frac{S}{D}$, which depends on frequency. This mode, plotted in Figure 2.2, is known as the extraordinary or X-mode.

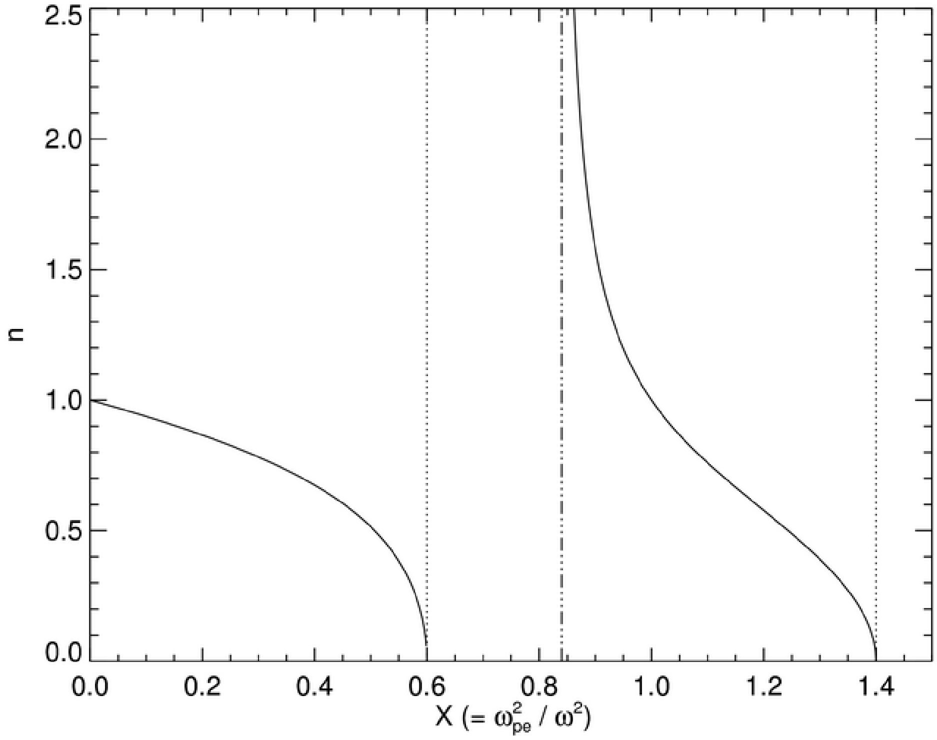

Figure 2.2: X-mode dispersion relation (see Equation 2.42) where wave vector $\mathbf{k} \perp \mathbf{B_0}$. Refractive index n plotted against squared ratio of plasma frequency to wave frequency, for a ratio of cyclotron frequency to wave frequency (ω_{ce}/ω) of 0.4. R- and L-polarised cutoffs shown by dotted lines; upper hybrid resonance shown by dot-dashed line.

Here, $n_\perp \to 0$ if $R, L \to 0$, so the X-mode experiences the cutoffs of both the R- and L-polarised parallel modes previously discussed (Equation 2.40). It also has a resonance at $S \to 0$, which is satisfied if $\omega^2 = \omega_{ce}^2 + \omega_{pe}^2$. This is known as the *upper hybrid* frequency.

The electric field components for O and X-modes propagating perpendicular to B_0 are sketched in Figure 2.3.

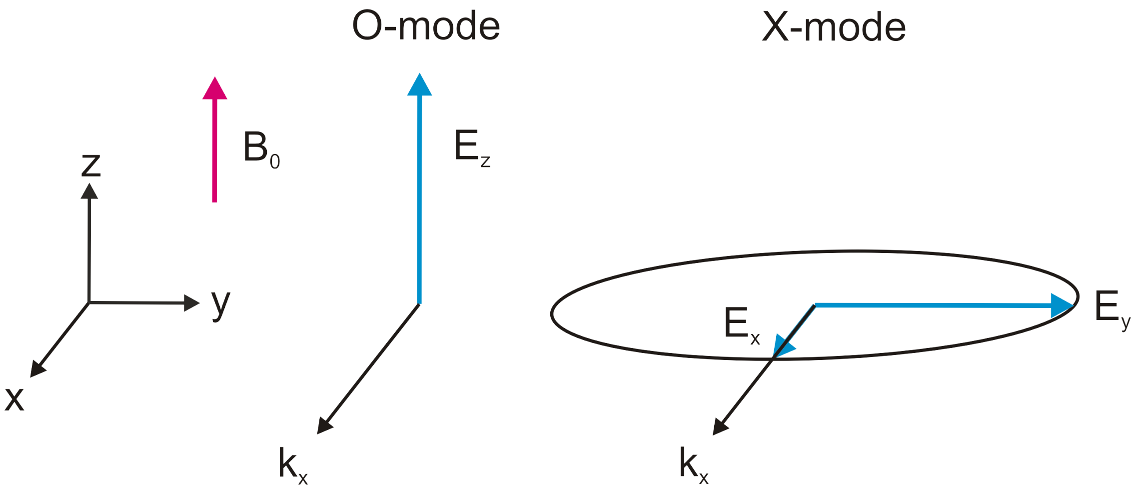

Figure 2.3: Electric field orientations for O and X-modes propagating in x-direction perpendicular to background magnetic field B_0. O-mode is transverse and linearly polarised perpendicular to B_0; X-mode is elliptically polarised with both transverse (E_y) and longitudinal (E_x) components.

2.1.5 Ordinary to Extraordinary mode conversion

In the more general case of oblique propagation at an angle θ to $\mathbf{B_0}$, the cold plasma dispersion relation (Equation 2.38) can be rewritten in terms of n^2 :

$$n^2 = n_\perp^2 + n_\parallel^2 = 1 - \frac{2X\left(1-X\right)}{2\left(1-X\right) - Y^2\sin^2\theta \pm \Gamma} \tag{2.43}$$

$$\Gamma = \left[Y^4\sin^4\theta + 4\left(1-X\right)^2 Y^2\cos^2\theta\right]^{1/2} \tag{2.44}$$

This is known as the Appleton-Hartree formula. For clarity, the convention now adopted is that $X = \frac{\omega_{pe}^2}{\omega^2}$ and $Y = \frac{|\omega_{ce}|}{\omega}$. If the sign before Γ is positive, then it describes the obliquely propagating O-mode; if negative, it describes the obliquely propagating X-mode.

At the O-mode density cutoff, $X = 1$. If it is also the case that $\theta = 0$, i.e. the wave vector $\mathbf{k}$ is parallel to $\mathbf{B_0}$, then $\Gamma = 0$ and the two modes are degenerate. In this case a complete conversion from one electromagnetic mode to the other can occur. This will happen for an optimum value of $n_{\parallel}$ given by

$$n_{\parallel}^2 = \frac{Y}{Y+1} \tag{2.45}$$

If an O-mode propagating into a plasma of increasing density satisfies this relation at the density cutoff, conversion into an X-mode will occur with 100% efficiency. Away from this angle, an evanescent layer interferes with this coupling, but for small angular deviations the wave can tunnel through so that conversion still occurs at a reduced efficiency. This causes an elliptical 'mode conversion window' about this angle.

2.2 Waves in warm plasmas

So far, only cold plasma theory has been discussed. In this approximation, electrons have zero thermal velocity so the Larmor radius of their gyro-orbits around magnetic fieldlines is zero. However, the plasmas of interest have a finite temperature and thus their electrons have thermal velocity v_{th}. This means that their Larmor radius ρ_e becomes finite:

$$\rho_e = \frac{m_e v_{th}}{|e|B} \tag{2.46}$$

New physics is introduced due to these ‘finite Larmor radius’ (FLR) effects. The fluid equations used previously in this chapter no longer describe all the mode dynamics, so to obtain a dispersion relation, a kinetic treatment must be adopted, solving the Vlasov equation:

$$\frac{\partial f_s}{\partial t} + \mathbf{v} \cdot \frac{\partial f_s}{\partial \mathbf{x}} + \frac{q_s}{m_s} \left[\mathbf{E} + \frac{1}{c} \mathbf{v} \times \mathbf{B} \right] \cdot \frac{\partial f_s}{\partial \mathbf{v}} = 0 \tag{2.47}$$

where f_s is the distribution function of particle species s. This derivation is quite involved and will not be presented here; for more details, see Stix [26]. This gives rise to a hot dielectric tensor, which is equivalent to Equation 2.31 but significantly more complicated.

2.2.1 Warm plasma modes

If the modes propagating perpendicular to $\mathbf{B_0}$, where $k_\parallel = 0$, are investigated as in 2.1.4, with the additional prescription that they have frequencies away from the harmonic resonances, i.e. $\omega \neq n\omega_{ce}$, the following non-zero components of the hot dielectric tensor are obtained:

$$\varepsilon_{xx} = 1 - \frac{\omega_{pe}^2}{\omega} \sum_{n=-\infty}^{\infty} e^{-\lambda} \frac{n^2 I_n(\lambda)}{\lambda} \frac{1}{\omega - n\omega_{ce}} \tag{2.48}$$

$$\varepsilon_{xy} = 2 - \varepsilon_{yx} = 1 + i \frac{\omega_{pe}^2}{\omega} \sum_{n=-\infty}^{\infty} n e^{-\lambda} \left[I_n(\lambda) - I_n'(\lambda) \right] \frac{1}{\omega - n\omega_{ce}} \tag{2.49}$$

$$\varepsilon_{yy} = 1 - \frac{\omega_{pe}^2}{\omega} \sum_{n=-\infty}^{\infty} e^{-\lambda} \left[\frac{n^2 I_n(\lambda)}{\lambda} + 2\lambda I_n(\lambda) - 2\lambda I_n'(\lambda) \right] \frac{1}{\omega - n\omega_{ce}} \tag{2.50}$$

$$\varepsilon_{zz} = 1 - \frac{\omega_{pe}^2}{\omega} \sum_{n=-\infty}^{\infty} e^{-\lambda} I_n(\lambda) \left[1 - \frac{n\omega_{ce}}{\omega} \frac{T_\perp - T_\parallel}{T_\perp} \right] \frac{1}{\omega - n\omega_{ce}} \tag{2.51}$$

where $\lambda = \frac{1}{2}k_{\perp}^{2}\langle\rho_{L}^{2}\rangle = \frac{k_{\perp}^{2}\kappa T_{\perp}}{m_e\omega_{ce}^{2}}$, I_n is the modified Bessel function of the nth order and $T_{\perp}, T_{\parallel}$ are the perpendicular and parallel electron temperatures respectively.

If Equation 2.15 is solved using this version of the dielectric tensor, two equations corresponding to Equations 2.41 and 2.42 are obtained:

$$n_x^2 = \varepsilon_{zz} \tag{2.52}$$

$$n_x^2 = \varepsilon_{yy} - \frac{\varepsilon_{xy}\varepsilon_{yx}}{\varepsilon_{xx}} \tag{2.53}$$

This shows that the O- and X-mode dispersion relations have been recovered. A new physical effect obtained is that of harmonic cyclotron damping: the resonant denominator of all terms of the dielectric tensor means that these modes are strongly damped at harmonics of the cyclotron frequency, $\omega = n\omega_{ce}$. At these cyclotron harmonics, the resonant particle “sees” the first-order electric field at zero frequency in the reference frame of its own zero-order motion. Energy is thus resonantly transferred from the field to the particle; this is the mechanism by which the ECRH technique heats a plasma.

It should be noted that in the cold plasma limit, where $T \to 0$ and therefore $\lambda \to 0$, the hot dielectric tensor components in Equations 2.48 - 2.51 reduce to their cold-plasma equivalents, and therefore the dispersion relations for O and X-mode (Equations 2.52 and 2.53) reduce to Equations 2.41 and 2.42.

2.2.2 The electron Bernstein mode

Having investigated electromagnetic modes, we now turn to electrostatic modes in a hot plasma. To do this, we approximate the wave electric field in terms of an electrostatic potential: $\mathbf{E}(\mathbf{r}, t) = -\nabla\phi(\mathbf{r}, t)$. This simplifies the calculation of the dispersion relation.

If propagation perpendicular to $\mathbf{B_0}$ is investigated, with the assumption that $k_{\perp}$ is sufficiently large (i.e. wavelength sufficiently small with respect to ρ_e), solutions to the electrostatic dispersion relation can be obtained. The spectrum of modes that emerge are known as electron Bernstein waves (EBWs) after their discoverer [32].

EBWs are longitudinal electrostatic plasma waves, caused by collective gyromotion of the electrons resulting in oscillations in charge density. They are backwards waves in that their phase and group velocities have opposite sign.

If $k_\perp$ is allowed to become smaller and the dispersion relation is more carefully investigated, it can be seen that the Bernstein and X-modes become coupled at the upper hybrid resonance. As an X-mode approaches this resonance, its wavelength becomes increasingly short until it is on the same order as the electron Larmor radius. At this point FLR effects can no longer be ignored and an 'X-B' mode conversion occurs to a Bernstein mode.

This O-X-B conversion process has been investigated as a potential means of heating and current drive in overdense fusion plasmas (in which EC resonances are otherwise inaccessible to conventional microwave heating techniques), such as stellarators [33] and spherical tokamaks [34]. In addition, the emission due to the inverse B-X-O conversion process is now being used as a basis for tokamak diagnostics such as SAMI (see Subsection 1.3.2).

Chapter 3

Numerical background

3.1 Cold plasma simulation

The study of electron cyclotron frequency range EM wave propagation in magnetised plasmas has broad relevance, from ionospheric radio wave studies [21] to heating and current drive [35] and diagnostics [36] in magnetically confined fusion plasmas.

In order to numerically simulate interactions between EM waves and a cold plasma dielectric, several main approaches are possible; ray tracing, scalar wave equations such as the paraxial wave equation and full-wave simulation, of which an example approach is the finite-difference time-domain (FDTD) method. The fundamentals of these approaches are discussed in this chapter.

3.1.1 Ray tracing

This technique allows the evolution in space and time of a single ray through a plasma to be tracked. This ray exists as a unique solution to the dispersion relation of interest at a given point in space and time.

For ray tracing to be valid, it must be assumed that spatial and temporal variations in the refractive index of the plasma are slow, and the wave vector field therefore depends only weakly on position and time. The lowest-order WKB (Wentzel–Kramers–Brillouin) approximation can therefore be applied.

We start from a general wave equation:

$$\underline{\underline{M}}\left(i\frac{\partial}{\partial t}, -i\nabla, \mathbf{r}, t\right)\psi = 0 \tag{3.1}$$

where $\underline{\underline{M}}$ is a matrix describing the plasma dispersion relation and ψ is a vector containing the wave field components. The lowest-order WKB approximation allows us to make the assumption that $\psi\left(\mathbf{r}, t\right) = \psi \exp(i\phi(t + \mathbf{r}))$, resulting in the approximation [25]:

$$\underline{\underline{M}}\left(\omega, \mathbf{k}, \mathbf{r}, t\right)\psi = 0 \tag{3.2}$$

where $\omega = -\partial\phi/\partial t$ and $\mathbf{k} = \nabla\phi$. Solutions to this will now satisfy

$$\mathcal{M} \equiv \det\left(\underline{\underline{M}}\right) = 0 \tag{3.3}$$

The choice of $\underline{\underline{M}}$ determines the mode physics. An example is the magnetised cold-plasma dispersion relation given in chapter 2, but ray tracing can also be carried out for the hot plasma dispersion relation.

The ray equations are

$$\frac{d\mathbf{r}}{dt} = \frac{\partial\Omega}{\partial\mathbf{k}} \tag{3.4}$$

$$\frac{d\mathbf{k}}{dt} = -\nabla\Omega \tag{3.5}$$

$$\frac{d\omega}{dt} = \frac{\partial\Omega}{\partial t} \tag{3.6}$$

where $\omega = \Omega\left(\mathbf{k}, \mathbf{r}, t\right)$ is the frequency given by the desired solution to the dispersion relation for a given wavevector $\mathbf{k}$, spatial point $\mathbf{r}$ and time t.

From an initial condition, $\mathbf{r}$, $\mathbf{k}$ and ω can therefore be evolved in time over a sufficiently short distance, $\mathcal{M}$ updated using their new values and this process then iterated over the full trajectory of the ray.

When (as is generally true) there is more than one solution to Equation 3.3 and thus more than one mode present, each mode can be tracked independently as it propagates away from its starting position. Different modes can be characterised and identified by their trajectories and wavelengths.

The WKB assumption breaks down in regions where fast variations occur, for example near resonances and cutoffs as well as for cases where background scale lengths are comparable to the wavelength. In such regions, the additional computational expense of full-wave modelling is necessary to obtain a full physical picture (see Section 3.1.3).

The application of ray-tracing methods to plasma physics dates back to studies of ionospheric cold-plasma mode propagation of the late 1950s [37], when the birth of high-performance computing had made the iterative solution of these equations feasible. Later, the technique began to be applied to magnetically confined fusion plasmas; in the late 1970s, ray-tracers solving the hot-plasma dispersion relation began to be applied to ICRH [38] and ECRH [39] problems in a tokamak geometry, with both electromagnetic and mode-converted Bernstein modes investigated.

To circumvent the issue of the WKB approximation's inapplicability in regions of steep density gradient, a more recent approach has been to couple a ray tracing code to a full-wave solver [40]. This has been used to model the full O-X-B conversion process in a tokamak plasma, by switching to a finite-element solver when the mode conversion region is reached and using the ray tracer's output as an input at this point.

3.1.2 The paraxial wave equation

We begin with the Helmholtz equation for an inhomogeneous plasma:

$$\left(\nabla^2 + k^2 n^2(\mathbf{r})\right)\psi = 0 \tag{3.7}$$

where n is the refractive index. If propagation is assumed to be along or at small angles to the z-axis, the paraxial approximation can be made that $\psi(x, y, z) \simeq \psi'(x, y, z)\exp(ikz)$; it is also assumed that n varies slowly along the direction of propagation, as for the WKB approximation. Substituting this into Equation 3.7 and cancelling terms results in the paraxial wave equation

$$\left(\frac{\partial^2}{\partial x^2} + \frac{\partial^2}{\partial y^2}\right)\psi + 2ik\frac{\partial \psi}{\partial z} + (n^2(\mathbf{r}) - 1)k^2\psi = 0 \tag{3.8}$$

which can then be solved numerically. This is a common approach to modelling laser pulse propagation in a plasma; however, like ray tracing, it loses validity for regions of fast variation of refractive index and therefore is not appropriate for the work in this thesis. Furthermore, it neglects backscattering, which is predicted to be a significant effect for the models of interest. A full-wave approach was therefore adopted.

3.1.3 Full-wave modelling

Full-wave simulations give direct solutions of Maxwell's equations plus extra equations to describe the dielectric response of the plasma, and do not rely on the WKB approximation for validity. This approach can therefore be applied to regions of the plasma which cannot be treated using ray tracing, and is needed for the work on EC interactions with inhomogeneity described in this thesis.

Full-wave modelling is a broad topic, and so the discussion in this section will be limited to the EC frequency range (although it has also been extensively applied to ion cyclotron [41] and lower hybrid waves [42]). Further, although finite element methods have been applied in this area (e.g. [40]), finite differencing schemes have seen more use and are therefore the focus.

Two major classes of approach have been used for incorporating plasma background into the FDTD scheme described in Section 3.2. Firstly, direct integration (DI) or auxiliary differential equation (ADE) methods, which solve Equations 3.20 - 3.25 plus a differential equation for the current density term in Equations 3.23 - 3.25 [43]. For a cold magnetised plasma, this takes the form:

$$\frac{\partial \mathbf{J}}{\partial t} = \varepsilon_0 \omega_{pe}^2 \mathbf{E} - \omega_{ce} \mathbf{J} \times \hat{\mathbf{b}}_0 - \nu \mathbf{J} \tag{3.9}$$

which is the linearised fluid equation of motion for the electrons. Here ω_{pe} and ω_{ce} are the local electron plasma frequency and cyclotron frequency, $\hat{\mathbf{b}}_0$ is the unit vector parallel to the background magnetic field and ν is the electron collision frequency. The method used to solve this can vary widely depending on the implementation.

The second class is that of recursive convolution (RC) methods, which are derived by relating the electric flux density to a time-domain convolution of the electric field intensity with the plasma susceptibility [44]:

$$\mathbf{D}|^n = \varepsilon_0 \varepsilon_\infty \mathbf{E}|^n + \varepsilon_0 \int_{\tau=0}^{n\Delta t} \underline{\underline{\chi}}(\tau) \cdot \mathbf{E}(n\Delta t - \tau) d\tau \tag{3.10}$$

resulting similarly in a set of extra equations to be solved at each timestep. Here ε_∞ is the dielectric constant at infinite frequency and $\underline{\underline{\chi}}$ is the susceptibility, which is a tensor for magnetised plasma but a scalar for unmagnetised plasma. It is related to the dielectric tensor as $\underline{\underline{\varepsilon}} = \varepsilon_0(\underline{\underline{\chi}} + I)$.

Historically, the choice of method resulted from a tradeoff between generally less computationally demanding RC and generally more accurate DI, but the introduction of the piecewise linear recursive convolution (PLRC) method brought improved accuracy while retaining lower computational cost [45]. This improvement was obtained by replacing the assumption of a constant electric field over Δt with a piecewise linear approximation over this interval:

$$\mathbf{E}(t) = \mathbf{E}|^n + \frac{\mathbf{E}|^{n+1} - \mathbf{E}|^n}{\Delta t}(t - n\Delta t) \tag{3.11}$$

The RC method was originally implemented for unmagnetised plasma simulations but was later modified [46] to cover magnetised plasma, resulting in a more complex system of equations.

An example of an early application of a DI method FDTD model to a tokamak plasma is Irby *et al.* (1993) [47]. This was a 2D study of O-mode reflectometry; the background magnetic field was neglected, reducing the linearised fluid equation of motion to

$$\frac{\partial \mathbf{J}}{\partial t} = \varepsilon_0 \omega_{pe}^2 \mathbf{E} \tag{3.12}$$

Time-dependent perturbations to the plasma background such as a propagating density pulse and oscillatory modes were made at timescales much longer than those of the propagating mode, and the variations in amplitude and phase of the scattered signal recorded.

If a background magnetic field is considered, a problem is posed by the coupling of the three components of Equation 7.2 due to the $\mathbf{J} \times \hat{\mathbf{b}}_0$ term. When stepping from $t = n\Delta t$ to $t = (n+1)\Delta t$, the resulting equations take the form

$$\begin{aligned} J_x|^{n+1} &= f(\mathbf{E}|^{n+\frac{1}{2}}, J_y|^n, J_z|^n) \\ J_y|^{n+1} &= f(\mathbf{E}|^{n+\frac{1}{2}}, J_x|^n, J_z|^n) \\ J_z|^{n+1} &= f(\mathbf{E}|^{n+\frac{1}{2}}, J_x|^n, J_y|^n) \end{aligned} \tag{3.13}$$

If these are solved simultaneously in this way (as e.g. in [48]), copies of J_x and J_y at $t = n\Delta t$ must be stored during calculation and additional memory is therefore required. Another approach, adopted in [49], is to simply discard the old values and solve in this way, equivalent to a symplectic Euler method:

$$\begin{aligned} J_x|^{n+1} &= f(\mathbf{E}|^{n+\frac{1}{2}}, J_y|^n, J_z|^n) \\ J_y|^{n+1} &= f(\mathbf{E}|^{n+\frac{1}{2}}, J_x|^{n+1}, J_z|^n) \\ J_z|^{n+1} &= f(\mathbf{E}|^{n+\frac{1}{2}}, J_x|^{n+1}, J_y|^{n+1}) \end{aligned} \tag{3.14}$$

where f are linear functions. This, however, results in a loss of the FDTD scheme's second-order accuracy. An alternative method of solution will be developed in the following chapter.

Recently, hot-plasma dispersion effects have been implemented in FDTD. Köhn *et al.* (2008) [49] added a correction (obtained from [50]) to the dielectric tensor of a cold-plasma model which allowed electron Bernstein modes to propagate in the vicinity of the upper hybrid resonance. This allowed the visualisation of the full 2D O-X-B mode conversion process in a tokamak plasma for the first time. Elsewhere, the full warm-plasma dielectric tensor has been implemented in a 1D FDTD model [51].

3.2 The FDTD method

3.2.1 Introduction

The FDTD technique allows numerical time-domain solutions to Maxwell's equations over a spatially discretised grid. It enables the simulation of a very wide range of electromagnetic wave scattering phenomena in structures which can be large and volumetrically complex, and can include effects such as nonlinear polarisation. Its computational requirements can be quite high, but with both hardware and programming advances in high performance parallel computing (to which the technique is well suited) this is increasingly becoming less of a limitation [52].

The time-domain (as opposed to frequency-domain) solutions obtained allow a broad range of frequencies to be studied with a single simulation, with effects such as Doppler shift automatically accounted for. It also allows time-marched visualisations to be produced, providing a more intuitive understanding of physical processes.

The technique was originally formulated by Yee in 1966 [53], and has become increasingly popular in research and engineering applications since around 1990. This has included full-wave simulation of EM waves in plasma, as seen in section 3.1.3. Comprehensive background can be found in Taflove & Hagness [52], as well as the guide written by Schneider [54].

In this chapter, the standard derivation of the 3D FDTD scheme for the case of vacuum background is presented, followed by a discussion of the simulation of EM modes in plasma (both using the FDTD method and other techniques).

3.2.2 3D derivation

Direct numerical solutions for the evolution of **B** and **E** are sought by substituting finite difference formulae for the field derivatives in both space and time into Equations 2.7 and 2.8:

$$\frac{\partial \mathbf{B}}{\partial t} = -\nabla \times \mathbf{E} \tag{3.15}$$

$$\frac{\partial \mathbf{E}}{\partial t} = c^2 \nabla \times \mathbf{B} - \frac{1}{\varepsilon_0}\mathbf{J} \tag{3.16}$$

In order to facilitate this, the electric and magnetic field components are discretised over a staggered spatial grid, as shown in Figure 3.1, such that no two components are evaluated at the same point. This arrangement is known as the Yee cell after its originator. It is assumed here (although alternative non-Cartesian or unstructured grids are possible) that the cell is cubic with sides of length Δx. Centred differences can be then be taken at each field component from the 4 components of other fields at a separation of $\frac{1}{2}\Delta x$ in the spatial domain.

In addition to this, the fields are staggered in time, such that **E** is calculated, **B** is calculated one half time-step later, then **E** is calculated again after one full time-step and so on. This allows a leapfrog scheme to be used such that centred differences are taken at a separation of $\frac{1}{2}\Delta t$ in the time domain, where one timestep is Δt.

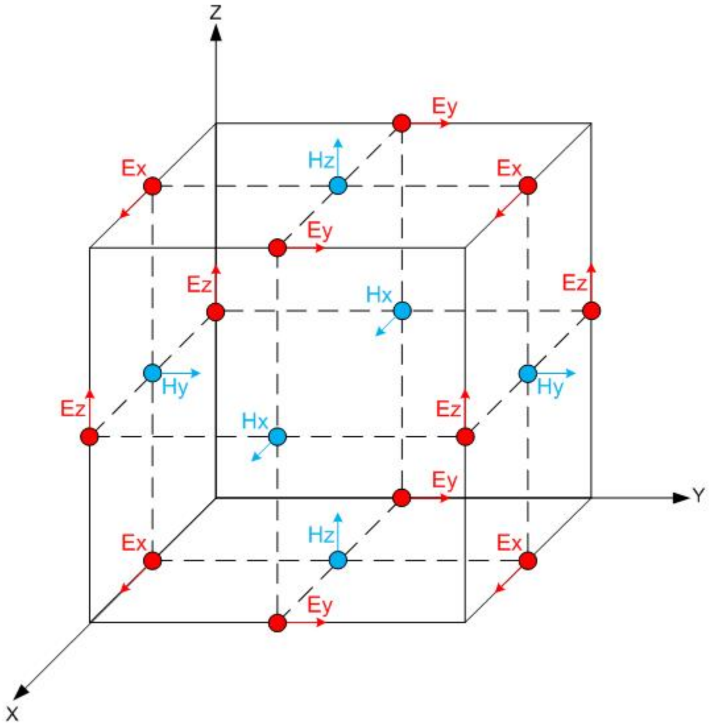

Figure 3.1: The Yee cell - spatial discretisation of 3D electric and magnetic fields as used in the FDTD scheme[55]

In the notation used here, the numerical solution for a scalar field component u at a given grid location and time will be written

$$u\left(i\Delta x, j\Delta x, k\Delta x, n\Delta t\right) = u|^{n}_{i,j,k} \tag{3.17}$$

where i, j, k, n are integers corresponding to the number of steps in the (x, y, z, t) dimensions respectively.

The following centred difference formulae are then used:

$$\frac{\partial}{\partial x}u|^n_{i,j,k} = \frac{1}{\Delta x}(u|^n_{i+\frac{1}{2},j,k} - u|^n_{i-\frac{1}{2},j,k}) + O\left[\Delta x^2\right] \tag{3.18}$$

$$\frac{\partial}{\partial t}u|^n_{i,j,k} = \frac{1}{\Delta t}(u|^{n+\frac{1}{2}}_{i,j,k} - u|^{n-\frac{1}{2}}_{i,j,k}) + O\left[(\Delta t)^2\right] \tag{3.19}$$

thus giving second-order accuracy in both time and space. These are substituted into Equation 3.15 for each component of $\mathbf{B}$. For all components, temporal differencing is about timestep n, but the spatial midpoint is permuted for each due to the staggered grid; B_x about gridpoint $\left(i, j+\frac{1}{2}, k+\frac{1}{2}\right)$, B_y about $\left(i+\frac{1}{2}, j, k+\frac{1}{2}\right)$ and B_z about $\left(i+\frac{1}{2}, j+\frac{1}{2}, k\right)$. Solving these for the newer values of $\mathbf{B}$:

$$\begin{aligned} B_x|^{n+\frac{1}{2}}_{i,j+\frac{1}{2},k+\frac{1}{2}} &= B_x|^{n-\frac{1}{2}}_{i,j+\frac{1}{2},k+\frac{1}{2}} \\ &+ \frac{\Delta t}{\Delta x}\left[E_y|^n_{i,j+\frac{1}{2},k+1} - E_y|^n_{i,j+\frac{1}{2},k}\right. \\ &\qquad \left. -E_z|^n_{i,j+1,k+\frac{1}{2}} + E_z|^n_{i,j,k+\frac{1}{2}}\right] \end{aligned} \tag{3.20}$$

$$\begin{aligned} B_y|^{n+\frac{1}{2}}_{i+\frac{1}{2},j,k+\frac{1}{2}} &= B_y|^{n-\frac{1}{2}}_{i+\frac{1}{2},j,k+\frac{1}{2}} \\ &+ \frac{\Delta t}{\Delta x}\left[E_z|^n_{i+1,j,k+\frac{1}{2}} - E_z|^n_{i,j,k+\frac{1}{2}}\right. \\ &\qquad \left. -E_x|^n_{i+\frac{1}{2},j,k+1} + E_x|^n_{i+\frac{1}{2},j,k}\right] \end{aligned} \tag{3.21}$$

$$\begin{aligned} B_z|^{n+\frac{1}{2}}_{i+\frac{1}{2},j+\frac{1}{2},k} &= B_z|^{n-\frac{1}{2}}_{i+\frac{1}{2},j+\frac{1}{2},k} \\ &+ \frac{\Delta t}{\Delta x}\left[E_x|^n_{i+\frac{1}{2},j+1,k} - E_x|^n_{i+\frac{1}{2},j,k}\right. \\ &\qquad \left. -E_y|^n_{i+1,j+\frac{1}{2},k} + E_y|^n_{i,j+\frac{1}{2},k}\right] \end{aligned} \tag{3.22}$$

These are fully explicit update equations for $\mathbf{B}$, using stored values of $\mathbf{B}$ from timestep $\left(n-\frac{1}{2}\right)$ and stored values of E_x, E_y, E_z from timestep n. The advantages of the leapfrog scheme and staggered grid now become evident; only one timestep needs to be stored at a time, so only one array per field component is required. The temporal midpoint is then advanced to timestep $\left(n+\frac{1}{2}\right)$ and differences taken by repeating these substitutions on Equation 3.16 to obtain solutions for $\mathbf{E}$. Spatially, E_x is differenced about the gridpoint $\left(i+\frac{1}{2},j,k\right)$, E_y about $\left(i,j+\frac{1}{2},k\right)$ and E_z about $\left(i,j,k+\frac{1}{2}\right)$. This yields

$$\begin{aligned}
E_x\big|^{n+1}_{i+\frac{1}{2},j,k} &= E_x\big|^{n}_{i+\frac{1}{2},j,k} \\
&- \frac{c^2\Delta t}{\Delta x}\left[B_y\big|^{n+\frac{1}{2}}_{i+\frac{1}{2},j,k+\frac{1}{2}} - B_y\big|^{n+\frac{1}{2}}_{i+\frac{1}{2},j,k-\frac{1}{2}} - B_z\big|^{n+\frac{1}{2}}_{i+\frac{1}{2},j+\frac{1}{2},k} + B_z\big|^{n+\frac{1}{2}}_{i+\frac{1}{2},j-\frac{1}{2},k}\right] \\
&- \frac{\Delta t}{\varepsilon_0} J_x\big|^{n+1}_{i+\frac{1}{2},j,k}
\end{aligned} \tag{3.23}$$

$$\begin{aligned}
E_y\big|^{n+1}_{i,j+\frac{1}{2},k} &= E_y\big|^{n}_{i,j+\frac{1}{2},k} \\
&- \frac{c^2\Delta t}{\Delta x}\left[B_z\big|^{n+\frac{1}{2}}_{i+\frac{1}{2},j+\frac{1}{2},k} - B_z\big|^{n+\frac{1}{2}}_{i-\frac{1}{2},j+\frac{1}{2},k} - B_x\big|^{n+\frac{1}{2}}_{i,j+\frac{1}{2},k+\frac{1}{2}} + B_x\big|^{n+\frac{1}{2}}_{i,j+\frac{1}{2},k-\frac{1}{2}}\right] \\
&- \frac{\Delta t}{\varepsilon_0} J_y\big|^{n+1}_{i,j+\frac{1}{2},k}
\end{aligned} \tag{3.24}$$

$$\begin{aligned}
E_z\big|^{n+1}_{i,j,k+\frac{1}{2}} &= E_z\big|^{n}_{i,j,k+\frac{1}{2}} \\
&- \frac{c^2\Delta t}{\Delta x}\left[B_x\big|^{n+\frac{1}{2}}_{i,j+\frac{1}{2},k+\frac{1}{2}} - B_x\big|^{n+\frac{1}{2}}_{i,j-\frac{1}{2},k+\frac{1}{2}} - B_y\big|^{n+\frac{1}{2}}_{i+\frac{1}{2},j,k+\frac{1}{2}} + B_y\big|^{n+\frac{1}{2}}_{i-\frac{1}{2},j,k+\frac{1}{2}}\right] \\
&- \frac{\Delta t}{\varepsilon_0} J_z\big|^{n+1}_{i,j,k+\frac{1}{2}}
\end{aligned} \tag{3.25}$$

These are similar to Equations 3.20 - 3.22, but no longer fully explicit due to the current density term $\mathbf{J}$ being evaluated at timestep $(n+1)$. In vacuum with no current sources or sinks, **J** can be ignored, but the plasma dielectric tensor causes a **J** term to arise. This is the point at which care must be taken in the implementation of an appropriate plasma model; the treatment used in the new EMIT-3D code, developed as part of this thesis, will be covered in the following chapter.

It is seen, however, that a pair of update equations have been derived for each spatial dimension, which can be applied at each timestep to arrays of **E** and **B** components in order to solve the equations of evolution for **E** and **B** (3.15) and (3.16). It can be shown [52] that **E** and **B** will remain divergence-free in the absence of charges so that Equations 2.5 and 2.6 are also implicitly satisfied. An FDTD code can therefore be written in which some initial geometry and appropriate boundary conditions are specified, a source term is introduced and timestepping continues until a steady state has been reached and the scattered field patterns can be recorded.

The principal numerical stability constraint on the FDTD is the Courant condition (for derivation by complex-frequency analysis, see Taflove & Hagness [52]). For propagation in free space on a 3D grid, this sets an upper limit on the ratio of the timestep to the spatial step:

$$S_{\mathrm{lim,3D}} = \frac{c\Delta t}{\Delta x} = \frac{1}{\sqrt{3}} \tag{3.26}$$

Beyond this value, the numerical waves begin to grow exponentially, reaching a very large amplitude in a few timesteps and resulting in instability. The Courant number S is therefore fixed at a lower value at the beginning of each simulation.

The modification of the FDTD algorithm to include plasma dispersion results in a modification of this condition, and generally a more restrictive stability bound. This is discussed for the case of the EMIT-3D code in the following chapter.

3.3 Choice of technique

The method used in this work is the 3D ADE-FDTD technique. This was adopted for developing the EMIT-3D code for several reasons, which will now be outlined.

While propagation through a homogeneous or slowly-varying monotonic plasma density profile is well understood and can be calculated analytically or using a ray-tracing method, turbulent or otherwise perturbed profiles require detailed numerical modelling using a full-wave method.

A time-domain, as opposed to frequency-domain, method was chosen. This permits a model in which no knowledge of the modelled frequency is assumed. By using the ADE approach described in Section 3.1.3, frequency-independent simulation can be achieved; this is desirable since no assumption of constant frequency must be made. The future development of this code is planned to include time-dependent plasma densities; this will allow the modelling of moving plasma surfaces, causing Doppler effects which lead to frequency-shifted signals.

An additional benefit of a time-domain code is the possibility of visualisation of scattering processes by animating timesteps. EMIT-3D was used to produce several 3D animations allowing improved insight into microwave propagation through inhomogeneities.

The choice was made to write a 3D code, as an advance on previous work using 2D simulations. This was taken in order to allow modelling of microwave interaction in 3 dimensions with 3D inhomogeneities (e.g. those described in [30], [56]). When studying filament interactions (see Chapter 5), this allowed the assumption of zero out-of-plane scattering to be tested and cases of oblique incidence to be easily tested.

The computational expense of 3D FDTD is significant, requiring the storage and iteration over multiple very large arrays for each timestep. However, the applicability of parallel programming techniques to FDTD and the availability of clusters allowing runs with 100 or more parallel processes meant that these problems could be circumvented.

An investigation was made into the use of the commercially available COMSOL Multiphysics finite element simulation software package as an alternative to a code developed specifically for the project. However, attempts to use the RF module for time-domain simulations using this package were unsuccessful; evanescent regions in the plasma with negative permittivity led to an unstable solution. After discussion with COMSOL's technical support, it became clear that this would not be possible without a frequency-dependent material model being required.

A return was therefore made to code development. Additional benefits motivating this choice over the use of commercial software were flexibility, ease of modification and significant scope for optimisation.

Chapter 4

Algorithm & code development

4.1 Algorithmic development

4.1.1 Solving for plasma response

For propagation through free space, the current density $\mathbf{J} = 0$; however, it is nonzero in a plasma. In this chapter, a first-order perturbed current density $\mathbf{J}_1$ is added to the FDTD algorithm in order to model plasma dispersion effects. The method presented here was developed as part of this thesis work.

In order to calculate $\mathbf{J}$, the linearised fluid equation of motion for the electrons must be solved at each timestep:

$$\frac{\partial \mathbf{J}}{\partial t} = \varepsilon_0 \omega_{pe}^2 \mathbf{E} - \omega_{ce} \mathbf{J} \times \hat{\mathbf{b}}_0 - \nu \mathbf{J} \tag{4.1}$$

where ω_{pe} and ω_{ce} are the local electron plasma frequency and cyclotron frequency, $\hat{\mathbf{b}}_0$ is the unit vector parallel to the background magnetic field and ν is the electron collision frequency, set to zero on the main grid of the simulation but nonzero in the boundary regions to damp outgoing waves.

It should be pointed out here that no $\mathbf{J}_0 \times \mathbf{B}_1$ term is present, since a background current $\mathbf{J}_0$ is not included at this stage; for further development in this direction, see Chapter 7. In Equation 7.2, the convention adopted (as in the rest of this chapter) is that $\mathbf{J} = \mathbf{J}_1$, to match the first-order variables $\mathbf{E} = \mathbf{E}_1$ and $\mathbf{B} = \mathbf{B}_1$.

To obtain discretised solutions to this 3D system of equations, Equation 7.2 is written in matrix form:

$$\dot{\mathbf{J}}(t) = P\mathbf{J}(t) + \varepsilon_0\omega_{pe}^2\mathbf{E}(t) \tag{4.2}$$

where

$$P = \begin{bmatrix} -\nu & -b_z\omega_{ce} & b_y\omega_{ce} \\ b_z\omega_{ce} & -\nu & -b_x\omega_{ce} \\ -b_y\omega_{ce} & b_x\omega_{ce} & -\nu \end{bmatrix} \quad , \quad \hat{\mathbf{b}}_0 = (b_x, b_y, b_z)$$

This has the solution:

$$\mathbf{J}(t) = e^{P(t-t_0)}\mathbf{J}(t_0) + \varepsilon_0\omega_{pe}^2\int_{t_0}^{t} e^{P(t-\tau)}\mathbf{E}(\tau)\mathrm{d}\tau \tag{4.3}$$

In this discretisation scheme, $\mathbf{J}$ is calculated in phase with $\mathbf{B}$, i.e. at $t = (\frac{1}{2}, \frac{3}{2}, \frac{5}{2}, ...)\Delta t$, and so a value of $\mathbf{E}$ at $t = (0, 1, 2, ...)\Delta t$ is available. This is used as a midpoint approximation (valid for sufficiently small Δt) to the value of $\mathbf{E}$ over the interval $[t_0, t]$, allowing $\mathbf{E}$ to be removed from the convolution in Equation 4.3.

A simple integration results. After carrying this out and discretising ($\Delta t = t - t_0$), we obtain:

$$\mathbf{J}|^{n+\frac{1}{2}} = e^{P\Delta t}\mathbf{J}|^{n-\frac{1}{2}} + \varepsilon_0\omega_{pe}^2 P^{-1}\left(e^{P\Delta t} - I\right)\mathbf{E}|^{n} \tag{4.4}$$

Matrix exponentials must therefore be evaluated; inverse Laplace transforms were used to do this exactly, since $e^{P\Delta t} = \mathcal{L}^{-1}\{(sI-P)^{-1}\}^{t=\Delta t}$, although lower-order expansions could also be employed. Following this method through:

$$e^{P\Delta t} = \mathcal{L}^{-1}\left\{\begin{bmatrix} s+\nu & b_z\omega_{ce} & -b_y\omega_{ce} \\ -b_z\omega_{ce} & s+\nu & b_x\omega_{ce} \\ b_y\omega_{ce} & -b_x\omega_{ce} & s+\nu \end{bmatrix}^{-1}\right\}^{t=\Delta t} \tag{4.5}$$

After inverting the matrix, its components can be evaluated individually using these three identities:

$$\mathcal{L}^{-1}\left\{\frac{s+\nu}{(s+\nu)^2+\omega_{ce}^2}\right\}^{t=\Delta t} = e^{-\nu\Delta t}\cos(\omega_{ce}\Delta t) \tag{4.6}$$

$$\mathcal{L}^{-1}\left\{\frac{a\omega_{ce}}{(s+\nu)^2+\omega_{ce}^2}\right\}^{t=\Delta t} = ae^{-\nu\Delta t}\sin(\omega_{ce}\Delta t) \tag{4.7}$$

$$\mathcal{L}^{-1}\left\{\frac{a\omega_{ce}^2}{(s+\nu)\left[(s+\nu)^2+\omega_{ce}^2\right]}\right\}^{t=\Delta t} = ae^{-\nu\Delta t}\left(1-\cos(\omega_{ce}\Delta t)\right) \tag{4.8}$$

This results in a current density update equation in the form

$$\mathbf{J}|^{n+\frac{1}{2}} = e^{-\nu\Delta t}\Theta\mathbf{J}|^{n-\frac{1}{2}} + \frac{\varepsilon_0\omega_{pe}^2}{(\nu^2+\omega_{ce}^2)\Delta t}\Xi\mathbf{E}|^n \tag{4.9}$$

where

$$\Theta_{ij} = b_ib_j\left[1-\cos(\omega_{ce}\Delta t)\right] - \varepsilon_{ijk}b_k\sin(\omega_{ce}\Delta t) + \delta_{ij}\cos(\omega_{ce}\Delta t) \tag{4.10}$$

$$\Xi_{ij} = b_ib_j\alpha - \varepsilon_{ijk}b_k\beta + \delta_{ij}\gamma \tag{4.11}$$

$$\alpha = \frac{\omega_{ce}^2 \Delta t}{\nu} + \Delta t e^{-\nu \Delta t} \left[\nu \left(\cos(\omega_{ce} \Delta t) - 1 \right) - \omega_{ce} \sin(\omega_{ce} \Delta t) - \frac{\omega_{ce}^2}{\nu} \right] \tag{4.12}$$

$$\beta = \omega_{ce} \Delta t - \Delta t e^{-\nu \Delta t} \left[\omega_{ce} \cos(\omega_{ce} \Delta t) + \nu \sin(\omega_{ce} \Delta t) \right] \tag{4.13}$$

$$\gamma = \nu \Delta t + \Delta t e^{-\nu \Delta t} \left[\omega_{ce} \sin(\omega_{ce} \Delta t) - \nu \cos(\omega_{ce} \Delta t) \right] \tag{4.14}$$

and, as before, δ_{ij} and ε_{ijk} are the Kronecker delta and Levi-Civita symbols respectively.

This gives explicit update coefficients for J_x, with no storage of old components required after a timestep. After rearrangement and substitution of the update equations, the same equations are obtained for J_y and J_z. As static backgrounds are assumed over the timescale of a single simulation, these update coefficients can be calculated once at the beginning of a simulation and do not require updating.

A benchmarking test of the code is its ability to reproduce the analytic dispersion relations for the O- (ordinary) and X- (extraordinary) modes observed in a magnetised plasma. In order to carry this out for the case of perpendicular propagation, one-dimensional runs were carried with the field components E_x, E_z, B_y, J_x, J_z and a background magnetic field $\mathbf{B_0} = B_0\hat{\mathbf{x}}$ for O-mode and $\mathbf{B_0} = B_0\hat{\mathbf{y}}$ for X-mode.

A vacuum wavelength $\lambda_0 = 50\Delta z$ was used in a domain of length $1000\Delta z$ containing a homogeneous plasma background of given density n_e, terminated at either end by a lossy boundary region. A courant number $S = 0.5$ was used. A wave was excited using a point source, then allowed to propagate in the z-direction until reaching a steady state. The electric field components along the z-direction were recorded, and analysed by finding zero-crossing points and calculating the average wavelength over the length of the domain.

Over a set of runs, the plasma parameters n_e and B_0 were scanned, with the analysis repeated for each combination of factors. Very close agreement was observed for both modes; O-mode is plotted in Figure 4.1 and an example X-mode for one background magnetic field strength in Figure 4.2.

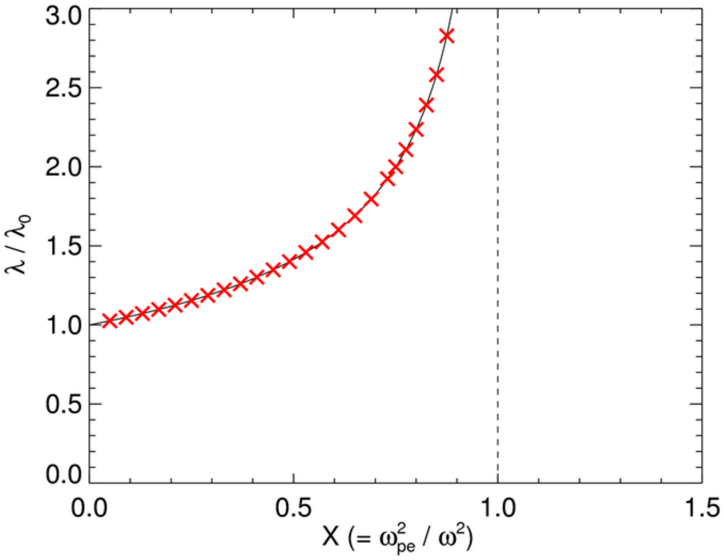

Figure 4.1: O-mode dispersion relation where wave vector $\mathbf{k} \perp \mathbf{B_0}$, calculated from averaged wavelength in EMIT-3D output. Wavelength normalised to vacuum wavelength plotted against density normalised to critical density. Red crosses: numerical, black line: analytic

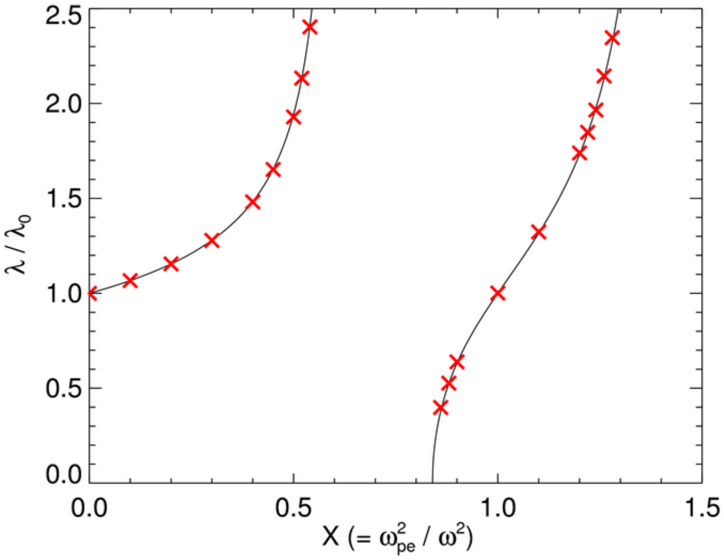

Figure 4.2: X-mode dispersion relation for $Y = |\omega_{ce}|/\omega = 0.4$ where wave vector $\mathbf{k} \perp \mathbf{B_0}$, calculated from averaged wavelength in EMIT-3D output. Wavelength normalised to vacuum wavelength plotted against density normalised to critical density. Red crosses: numerical, black line: analytic

4.1.2 Lossy layer boundary conditions

An absorbing boundary condition is required at the edges of the computational domain in order that reflections from outgoing waves do not affect the simulation results. One approach to this is with an artificial lossy layer; in the boundary regions, the electron collision frequency ν in Equations 4.12 — 4.14 is ramped linearly upwards from its edge value (zero in most cases) in order to avoid discontinuities.

After a specified boundary thickness, the grid is terminated with a Perfect Electrical Conductor (PEC) layer in which the condition $E = 0$ is enforced. Without a lossy layer, this results in 100% reflection, but with a layer of sufficient thickness, reflections can be effectively nullified.

The thickness of the layer is the main drawback to this method; for effective absorption, it must be on the order of several wavelengths, which presents a significant additional computational burden in 3D.

However, this is the method that is used in this work, since it is straightforward to implement and can also easily provide a measure of the power leaving the domain edge by summing the total absorption. With effective parallelisation on large machines, the computational cost becomes acceptable.

4.1.3 Perfectly matched layer boundary conditions

Another commonly used approach requiring a thinner absorbing layer and therefore reducing the requirement of memory storage is the Perfectly Matched Layer or PML boundary condition. This method was first proposed by Bérenger in 1994 [57], but this was in a 'split-field' formulation effectively doubling storage requirements. An unsplit PML was developed by Chew and Weedon [58].

A PML absorber is a non-physical, anisotropic medium designed to have the correct phase velocity and conductivity to completely eliminate reflections at the grid—PML boundary (although this only applies for a continuous physical picture; in the discretised formulation of FDTD, small reflections still occur).

PMLs cause exponential decay in waves travelling outwards and require only a thin layer for full absorption; ~ 10 gridpoints are required.

4.1.4 Stability

The stability constraint on FDTD schemes is given by a Courant condition. The Courant number $S = \frac{c\Delta t}{\Delta x}$ must be less than or equal to a critical value which, for the basic free-space algorithm as presented in section 3.1.2, depends simply on the dimensionality of the model [52] as follows:

$$\begin{aligned} S \leq &\quad 1 && \text{(1D)} \\ S \leq &\quad \tfrac{1}{\sqrt{2}} && \text{(2D)} \\ S \leq &\quad \tfrac{1}{\sqrt{3}} && \text{(3D)} \end{aligned}$$

However, once an auxiliary equation to solve for **J** is introduced, the constraint on this number is modified. A method for investigating this is to carry out von Neumann analysis on the system of equations being solved.

This is a standard mathematical technique used to investigate the numerical stability of linear finite difference schemes. First presented in 1950 by Charney et al. [59] for the case of a single equation being evolved, it can be generalised using a matrix formulation for methods such as FDTD which involve the iteration of multiple coupled equations. It has been applied to the stability of FDTD schemes containing dispersive media [60]; the presence of dispersive media (such as plasma) has previously been found to result in a more restrictive stability constraint.

Having developed a new application of the FDTD scheme in the previous section, it is necessary to check whether it will be numerically stable, and whether its stability constraints have been altered. Here, a new von Neumann analysis of the scheme developed above is presented, which was carried out as part of this thesis work. Due to the prohibitive difficulty of carrying this out in full 3D, a 1D analysis is carried out which can be generalised to higher dimensions.

4.1.4.1 No background magnetic field

First, for the purposes of this analysis, we obtain a 1D form of the FDTD equations in which the only spatial direction is z, the background magnetic field is zero and hence $\omega_{ce} = 0$ and so the only fields required for modes to propagate are E_x, B_y and J_x. However, a finite background plasma density (which can be taken to be either homogeneous throughout the domain or present at a single point) of ω_{pe} is present. This results in the update equations:

$$E_x\Big|_{j+\frac{1}{2}}^{n+1} = E_x\Big|_{j+\frac{1}{2}}^{n} - \frac{c^2\Delta t}{\Delta z}\left[B_y\Big|_{j+1}^{n+\frac{1}{2}} - B_y\Big|_{j}^{n+\frac{1}{2}}\right] - \frac{\Delta t}{\varepsilon_0}J_x\Big|_{j+\frac{1}{2}}^{n+\frac{1}{2}} \tag{4.15}$$

$$B_y\Big|_{j}^{n+\frac{1}{2}} = B_y\Big|_{j}^{n-\frac{1}{2}} - \frac{\Delta t}{\Delta z}\left[E_x\Big|_{j+\frac{1}{2}}^{n} - E_x\Big|_{j-\frac{1}{2}}^{n}\right] \tag{4.16}$$

$$J_x\Big|_{j+\frac{1}{2}}^{n+\frac{1}{2}} = e^{-\nu\Delta t} J_x\Big|_{j+\frac{1}{2}}^{n-\frac{1}{2}} + \varepsilon_0 \Delta t \omega_{pe}^2 \left(\frac{1-e^{-\nu\Delta t}}{\nu\Delta t}\right) E_x\Big|_{j+\frac{1}{2}}^{n} \tag{4.17}$$

Since the value of $\nu\Delta t$ used in simulations is very small ($\sim 10^{-12}$), limits are taken:

$$\lim_{\nu\Delta t\to 0} e^{-\nu\Delta t} = 1, \quad \lim_{\nu\Delta t\to 0} \frac{1-e^{-\nu\Delta t}}{\nu\Delta t} = 1$$

Equation 4.17 therefore reduces to:

$$J_x\Big|_{j+\frac{1}{2}}^{n+\frac{1}{2}} = J_x\Big|_{j+\frac{1}{2}}^{n-\frac{1}{2}} + \varepsilon_0 \Delta t \omega_{pe}^2 E_x\Big|_{j+\frac{1}{2}}^{n} \tag{4.18}$$

To proceed with the von Neumann analysis, it is first pointed out that the round-off error associated with each of the discretised field quantities will grow or decay over time in the same way as their numerical solution.

The spatial variation of error on each field quantity can be expanded as a Fourier series:

$$E_x\Big|_j^n = \sum_{m=1}^{M} \hat{E}_x^n e^{ik_m z_j}, \quad B_y\Big|_j^n = \sum_{m=1}^{M} \hat{B}_y^n e^{ik_m z_j}, \quad J_x\Big|_j^n = \sum_{m=1}^{M} \hat{J}_x^n e^{ik_m z_j}$$

and since the equations being investigated are linear, a single typical Fourier mode with wavenumber k can be substituted for each:

$$E_x\Big|_j^n = \hat{E}_x^n e^{ikz_j}, \quad B_y\Big|_j^n = \hat{B}_y^n e^{ikz_j}, \quad J_x\Big|_j^n = \hat{J}_x^n e^{ikz_j}$$

Elimination, rearrangement and substitution between timesteps is then used to recast the update equations in matrix form:

$$\mathbf{U}^{n+1} = G\mathbf{U}^n \tag{4.19}$$

where $\mathbf{U}^{n+1} = (\hat{E}_x^{n+1}, \hat{B}_y^{n+\frac{1}{2}}, \hat{J}_x^{n+\frac{1}{2}})$ is a vector of the updated Fourier mode amplitudes, $\mathbf{U}^n = (\hat{E}_x^n, \hat{B}_y^{n-\frac{1}{2}}, \hat{J}_x^{n-\frac{1}{2}})$ is a vector of the old field quantities and G is an amplification matrix.

The identities $e^{ik\Delta z} + e^{-ik\Delta z} - 2 = -4\sin^2(\frac{k\Delta z}{2})$ and $e^{\frac{ik\Delta z}{2}} + e^{-\frac{ik\Delta z}{2}} = 2i\sin(\frac{k\Delta z}{2})$ are used, resulting in:

$$G = \begin{bmatrix} 1 - \omega_{pe}^2\Delta t^2 - 4S^2\sin^2(\frac{k\Delta z}{2}) & -\frac{2ic^2\Delta t}{\Delta z}\sin(\frac{k\Delta z}{2}) & -\frac{\Delta t}{\varepsilon_0} \\ -\frac{2i\Delta t}{\Delta z}\sin(\frac{k\Delta z}{2}) & 1 & 0 \\ \varepsilon_0\Delta t\omega_{pe}^2 & 0 & 1 \end{bmatrix} \tag{4.20}$$

In order that unstable Fourier modes cannot grow over time, we require that the absolute value of the real part of each eigenvalue of the amplification matrix G is less than or equal to 1. A cubic equation for the eigenvalue λ is obtained by setting $\det(G - \lambda I) = 0$:

$$\begin{aligned} -\lambda^3 &+ \lambda^2(3 - \omega_{pe}^2\Delta t^2 - 4S^2\sin^2(\frac{k\Delta z}{2})) \\ &- \lambda(3 - \omega_{pe}^2\Delta t^2 - 4S^2\sin^2(\frac{k\Delta z}{2})) + 1 = 0 \end{aligned} \tag{4.21}$$

which has the roots

$$\begin{aligned} \lambda = 1, \quad \lambda = 1 &- 2S^2\sin^2(\frac{k\Delta z}{2}) - \frac{1}{2}\omega_{pe}^2\Delta t^2 \\ &\pm \frac{1}{2}\sqrt{(\omega_{pe}^2\Delta t^2 + 4S^2\sin^2(\frac{k\Delta z}{2}) - 2)^2 - 4} \end{aligned} \tag{4.22}$$

The real part of these can be plotted against S for a given value of $\omega_{pe}^2\Delta t^2$ and $\sin^2(\frac{k\Delta z}{2})$; see Figure 4.3. For the first two roots, $|\Re(\lambda)| \leq 1$ for all S at any reasonable value of $\omega_{pe}^2 \Delta t^2$. However, for the third root, $\Re(\lambda) < -1$ after some critical value of S, providing a stability limit. Rearranging in terms of Courant number, the stability condition is obtained:

$$S \sin(\frac{k\Delta z}{2}) \leq \frac{\sqrt{4 - \omega_{pe}^2 \Delta t^2}}{2} \tag{4.23}$$

where ω_{pe} is the maximum value of plasma frequency (and hence highest density) present in the simulation. Since the maximum value of $\sin(\frac{k\Delta z}{2}) = 1$, this can be simplified to

$$S \leq \frac{\sqrt{4 - \omega_{pe}^2 \Delta t^2}}{2} \tag{4.24}$$

The maximum stable value of S is thus linearly dependent on $\omega_{pe}\Delta t$. For the vacuum case, $\omega_{pe} = 0$ and so the 1D vacuum result of $S \leq 1$ is recovered.

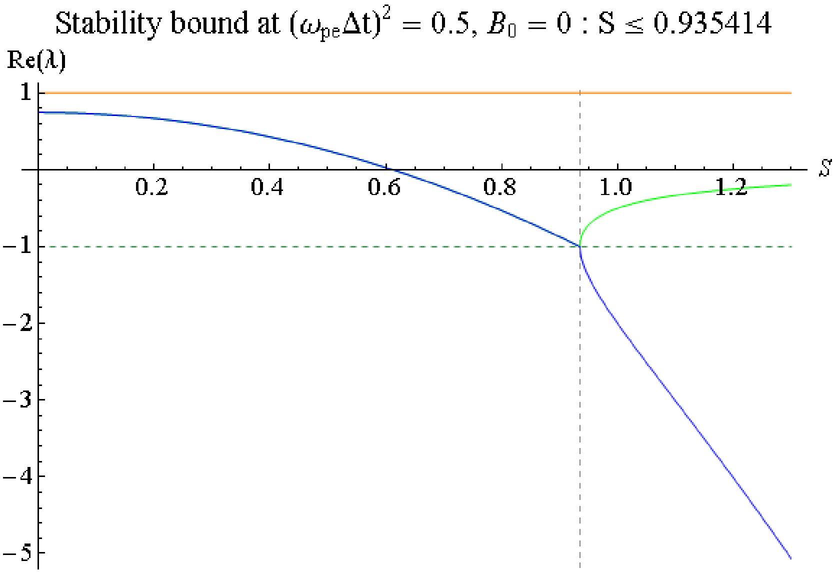

Figure 4.3: Real part of λ against Courant number S for $\omega_{pe}^2 \Delta t^2 = 0.5$, $\sin^2(\frac{k\Delta z}{2}) = 1$

4.1.4.2 Finite background magnetic field

To investigate the effect on this stability bound of a background magnetic field, we now extend the 1D model to allow $\omega_{ce} \neq 0$. A constant magnetic field in the y-direction is introduced, i.e. $\hat{\mathbf{b}}_0 = (0, 1, 0)$. Spatial derivatives are still only possible in the z-direction.

This introduces a coupling between J_x, E_z and J_z and hence additional update equations must be added to include these additional fields. Equations 4.15 and 4.16 for E_x and B_y are retained unaltered. The new equation for E_z is

$$E_z\big|_j^{n+1} = E_z\big|_j^{n} - \frac{\Delta t}{\varepsilon_0} J_z\big|_j^{n+\frac{1}{2}} \tag{4.25}$$

Equation 4.17 is modified due to the presence of B_0 and added alongside a new equation for J_z:

$$\begin{aligned} J_x\big|_{j+\frac{1}{2}}^{n+\frac{1}{2}} &= e^{-\nu\Delta t}\left[\cos(\omega_{ce}\Delta t) J_x\big|_{j+\frac{1}{2}}^{n-\frac{1}{2}} + \sin(\omega_{ce}\Delta t) J_z\big|_j^{n-\frac{1}{2}}\right] \\ &+ \frac{\varepsilon_0 \omega_{pe}^2}{(\nu^2 + \omega_{ce}^2)\Delta t}\left[\gamma E_x\big|_{j+\frac{1}{2}}^{n} + \beta E_z\big|_j^{n}\right] \end{aligned} \tag{4.26}$$

$$\begin{aligned} J_z\big|_j^{n+\frac{1}{2}} &= e^{-\nu\Delta t}\left[-\sin(\omega_{ce}\Delta t) J_x\big|_{j+\frac{1}{2}}^{n-\frac{1}{2}} + \cos(\omega_{ce}\Delta t) J_z\big|_j^{n-\frac{1}{2}}\right] \\ &+ \frac{\varepsilon_0 \omega_{pe}^2}{(\nu^2 + \omega_{ce}^2)\Delta t}\left[-\beta E_x\big|_{j+\frac{1}{2}}^{n} + \gamma E_z\big|_j^{n}\right] \end{aligned} \tag{4.27}$$

where β and γ are as defined in Section 4.1.1. This system of five equations is again written in matrix form as in Equation 4.19, with the vectors redefined such that $\mathbf{U}^{n+1} = (\hat{E}_x^{n+1}, \hat{E}_z^{n+1}, \hat{B}_y^{n+\frac{1}{2}}, \hat{J}_x^{n+\frac{1}{2}}, \hat{J}_z^{n+\frac{1}{2}})$ and $\mathbf{U}^{n} = (\hat{E}_x^{n}, \hat{E}_z^{n}, \hat{B}_y^{n-\frac{1}{2}}, \hat{J}_x^{n-\frac{1}{2}}, \hat{J}_z^{n-\frac{1}{2}})$. Using identities as before, G is now 5×5:

$$
\mathrm{G} = \begin{bmatrix}
1 - \frac{\gamma\omega_{pe}^2}{\nu^2+\omega_{ce}^2} - 4S^2\sin^2(\frac{k\Delta z}{2}) & -\frac{\beta\omega_{pe}^2 e^{-i\frac{k\Delta z}{2}}}{\nu^2+\omega_{ce}^2} & -\frac{2ic^2\Delta t}{\Delta z}\sin(\frac{k\Delta z}{2}) & -\delta\frac{\Delta t}{\varepsilon_0} & -\epsilon\frac{\Delta t}{\varepsilon_0}e^{-i\frac{k\Delta z}{2}} \\
\frac{\beta\omega_{pe}^2 e^{-i\frac{k\Delta z}{2}}}{\nu^2+\omega_{ce}^2} & 1 - \frac{\gamma\omega_{pe}^2}{\nu^2+\omega_{ce}^2} & 0 & \epsilon\frac{\Delta t}{\varepsilon_0}e^{i\frac{k\Delta z}{2}} & -\delta\frac{\Delta t}{\varepsilon_0} \\
-\frac{2i\Delta t}{\Delta z}\sin(\frac{k\Delta z}{2}) & 0 & 1 & 0 & 0 \\
\frac{\varepsilon_0}{\Delta t}\cdot\frac{\gamma\omega_{pe}^2}{\nu^2+\omega_{ce}^2} & \frac{\varepsilon_0}{\Delta t}\cdot\frac{\beta\omega_{pe}^2 e^{-i\frac{k\Delta z}{2}}}{\nu^2+\omega_{ce}^2} & 0 & \delta & \epsilon e^{-i\frac{k\Delta z}{2}} \\
-\frac{\varepsilon_0}{\Delta t}\cdot\frac{\beta\omega_{pe}^2 e^{i\frac{k\Delta z}{2}}}{\nu^2+\omega_{ce}^2} & \frac{\varepsilon_0}{\Delta t}\cdot\frac{\gamma\omega_{pe}^2}{\nu^2+\omega_{ce}^2} & 0 & -\epsilon e^{i\frac{k\Delta z}{2}} & \delta
\end{bmatrix}
$$

where

$$\delta = e^{-\nu\Delta t}\cos(\omega_{ce}\Delta t) \tag{4.28}$$

$$\epsilon = e^{-\nu\Delta t}\sin(\omega_{ce}\Delta t) \tag{4.29}$$

As before, the limit $\nu\Delta t \to 0$ is taken (so that $\delta \to \cos(\omega_{ce}\Delta t)$ and $\epsilon \to \sin(\omega_{ce}\Delta t)$ and the substitution $\sin^2(\frac{k\Delta z}{2}) = 1$ is made. This time, the eigenvalue equation is quintic:

$$-\lambda^5 + \Gamma\lambda^4 + \Lambda\lambda^3 - \Lambda\lambda^2 - \Gamma\lambda + 1 = 0 \tag{4.30}$$

where

$$\Gamma = 3 + 2\cos(\omega_{ce}\Delta t) - \frac{2\sin(\omega_{ce}\Delta t)}{\omega_{ce}\Delta t}\omega_{pe}^2\Delta t^2 - 4S^2 \tag{4.31}$$

$$
\begin{aligned}
\Lambda &= -4 - 6\cos(\omega_{ce}\Delta t) + (6 - 4S^2)\frac{\sin(\omega_{ce}\Delta t)}{\omega_{ce}\Delta t}\omega_{pe}^2\Delta t^2 \\
&- \frac{2 - 2\cos(\omega_{ce}\Delta t)}{(\omega_{ce}\Delta t)^2}\omega_{pe}^4\Delta t^4 + 4S^2 + 8S^2\cos(\omega_{ce}\Delta t)
\end{aligned} \tag{4.32}
$$

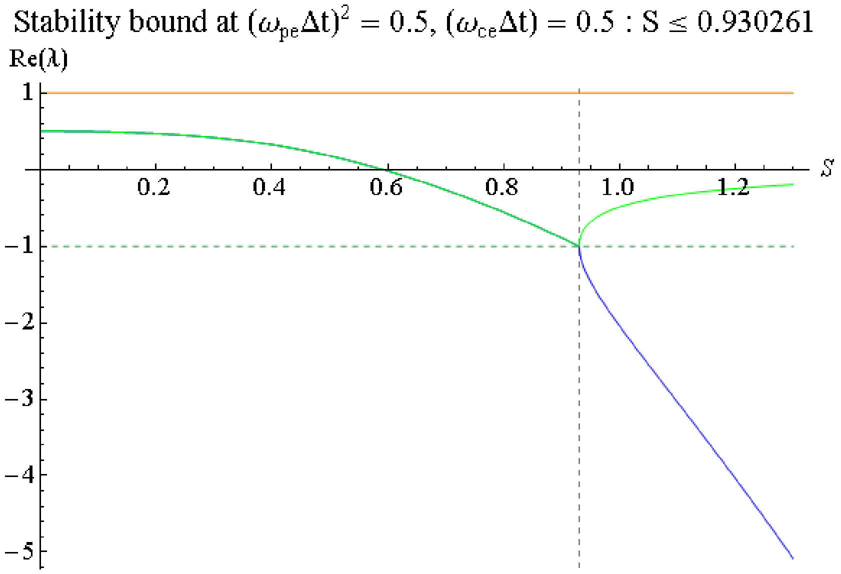

Figure 4.4: Real part of λ against Courant number S for $\omega_{pe}^2\Delta t^2 = 0.5$, $\omega_{ce}\Delta t = 0.5$

Aside from $\lambda = 1$, the other four roots of this equation are extremely unwieldy to express. However, the two newly arisen roots are found to have $|\Re(\lambda)| \le 1$ for all S at any reasonable value of $\omega_{pe}^2\Delta t^2$ and thus do not contribute to the stability bound.

The final two roots are seen to reduce to the second two in Equation 4.22 for the case that $B_0 = 0$; otherwise, their value is modified by the background magnetic field strength. These are plotted against S for extremely high sample values of ω_{pe} and ω_{ce} in Figure 4.4.

It can be seen from this plot that the presence of a magnetic field has a weak effect on the threshold value of S; compared to the previous case that $\omega_{pe}^2\Delta t^2 = 0.5$, $\omega_{ce}\Delta t = 0$, the introduction of a magnetic field with strength $\omega_{ce}\Delta t = 0.5$ causes a 0.55% reduction of the stability bound.

In order to rearrange the conditionally unstable root to a simple expression for the stability condition as in Equation 4.23, a small angle approximation is applied to the trigonometric functions of $\omega_{ce}\Delta t$. This is valid for all practical values of B_0 used in simulation.

$$\sin(\omega_{ce}\Delta t) \simeq \omega_{ce}\Delta t, \quad \cos(\omega_{ce}\Delta t) \simeq 1 - \frac{(\omega_{ce}\Delta t)^2}{2}$$

This results in the stability condition

$$S \leq \frac{1}{2}\sqrt{\frac{16 + (\omega_{pe}\Delta t)^4 - 8(\omega_{pe}\Delta t)^2 - 4(\omega_{ce}\Delta t)^2}{4 - (\omega_{pe}\Delta t)^2 - (\omega_{ce}\Delta t)^2}} \tag{4.33}$$

which is plotted as a surface in Figure 4.5.

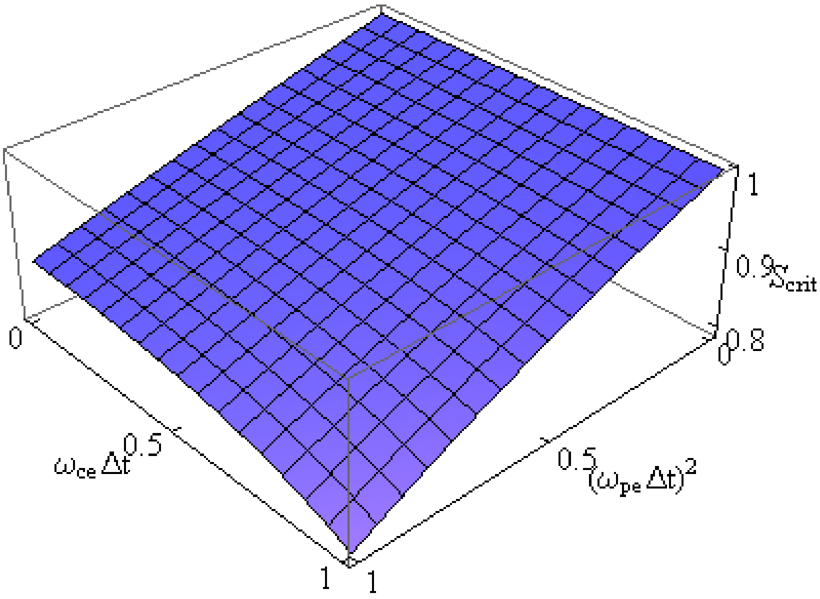

Figure 4.5: Dependence of maximum stable value of Courant number, S_{crit}, on maximum plasma and electron cyclotron frequencies in simulation

Von Neumann stability analysis has therefore shown that this adaptation of the FDTD method will be stable, as long as a Courant condition is obeyed. The maximum values of plasma and electron cyclotron frequencies present within the simulation domain dictate the value of this condition, but outside of extreme cases this dependence is weak. In practice, this condition can easily be satisfied without undue computational expense.

4.2 EMIT-3D

A code was written in the C programming language using the method developed in Section 4.1.1 and given the name EMIT-3D (**E**mission of **M**icrowaves past **I**nhomogeneities in the **T**ime-domain in **3** **D**imensions). Some further details are discussed in this section.

4.2.1 Source term

In order to excite waves on the grid, a 'soft' current density source which adds an oscillating current density component to cells at the source plane is used (as opposed to a 'hard' source in which electric or magnetic field values on the grid are directly specified). This has the advantage of being transparent to backscattered waves. The source is only applied at a single plane at the grid edge.

In order to avoid exciting spurious modes at the beginning of an FDTD simulation, the source amplitude must begin at zero and be ramped to its full value over several wave periods. At the beginning of an EMIT-3D simulation, an exponential function of time is convoluted with the expressions given here for this purpose.

For a mode excited in the xy plane and polarised in the x direction, the source current density term is of the form:

$$J_{x,\mathrm{s}}(x,y,t) = J_{x,\mathrm{s}}(x,y)\sin(\omega t + \phi_{\mathrm{s}}(x,y)) \tag{4.34}$$

where ω is the source frequency and $J_{x,\mathrm{s}}(x,y)$ and $\phi_{\mathrm{s}}(x,y)$ are the source current density amplitude and phase which can vary within the xy plane. This term is added directly to the non-source current term in Equation 3.23.

The Gaussian beams used in this thesis have amplitudes at the source plane:

$$J_{x,\mathrm{s}}(x,y) = J_{x,\mathrm{s}} \exp\left(\frac{-(x-x_0)^2-(y-y_0)^2}{w^2}\right) \tag{4.35}$$

where x_0, y_0 are the beam origin and w is the beam width at the source plane.

In order to focus a Gaussian beam at a desired distance from the source plane, $\phi_{\mathrm{s}}(x,y)$ can be varied across the plane to produce the correct beamfront curvature.

4.2.2 Parallelisation

Parallelisation was required in order to make 3D FDTD computationally tractable. The system used to achieve this is the Message Passing Interface (MPI). This is a widely used protocol for sending and receiving data between computational processes.

The parallelisation technique chosen was data-level decomposition due to its suitability for FDTD. The entire computational domain is broken up into evenly sized chunks, each of which is assigned to a process. During each timestep, each process independently iterates over its assigned data 'chunk' and then communicates with its neighbouring processes, only sending or receiving the datapoints necessary for calculations to proceed.

For each process, the data required from neighbouring processes in order to update the field quantities within its chunk is stored in 'ghost cells'. Since the numerical curl calculated in the FDTD update equations (3.20—3.25) dictates that the update of each discretised field quantity only relies on its nearest gridpoints in each spatial direction, only a single Yee cell thickness of ghost cells is required; see Figures 4.6 and 4.7.

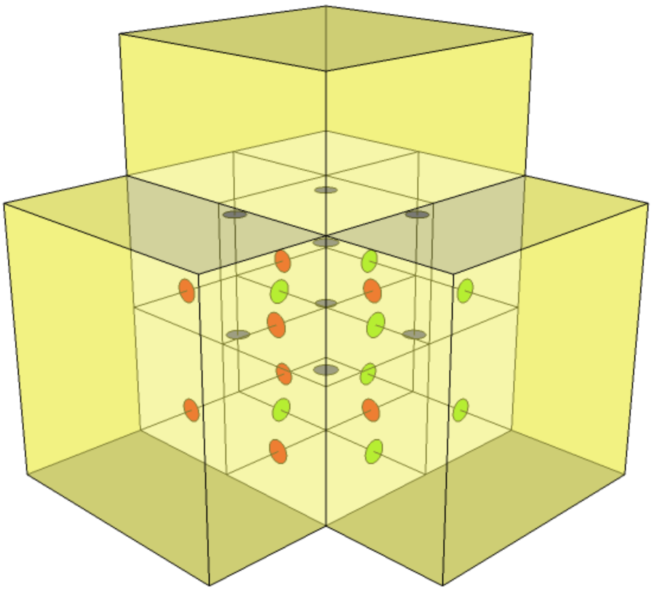

Figure 4.6: Ghost cells (yellow) of E-components required to calculate B-components in a 2x2x2 data chunk

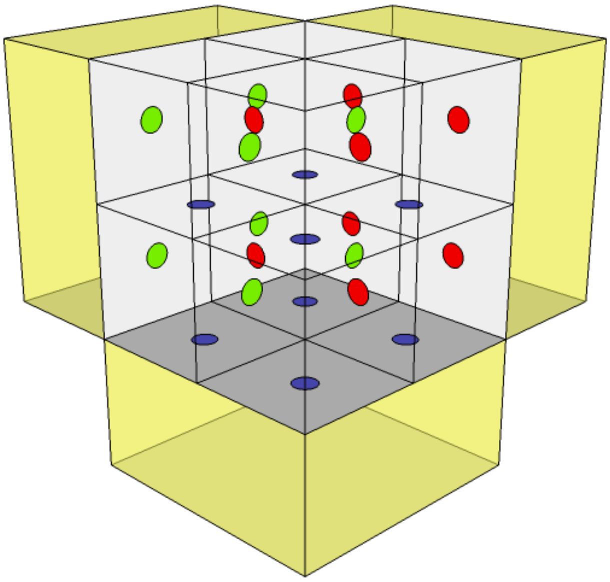

Figure 4.7: Ghost cells (yellow) of B-components required to calculate E-components in a 2x2x2 data chunk

In order to send and receive chunk faces, derived MPI datatypes are used. The following order of operations is used for each timestep:

1. Update J components from $t = n\Delta t \Rightarrow (n+1)\,\Delta t$ using Equation 4.9
2. Update B components from $t = n\Delta t \Rightarrow (n+1)\,\Delta t$ using Equations 3.20—3.22
3. Send and receive B components using MPI
4. Update E components from $t = \left(n + \frac{1}{2}\right)\Delta t \Rightarrow \left(n + \frac{3}{2}\right)\Delta t$ using Equations 3.23—3.25
5. Apply current source term
6. Send and receive E components using MPI

4.3 Analysis

The NetCDF file format is used to export data from EMIT-3D (as well as to import background density profiles). This is well suited to large output files and allows parallel output from each process during a run. Since very large 3D datasets are used in a typical simulation (>1 GB per run), only selected field quantities are written to file; this can be done at every timestep or at a specified sampling rate.

In order to further reduce disk usage, output can be restricted to a 2D plane (either xy, xz or yz), a line in a single direction or simply a point. 3D output can also be downsampled spatially; this technique was used when producing output to create animations.

Data analysis was largely carried out using IDL (Interactive Data Language). A set of routines was developed to join up parallel output, calculate time-averaged field quantities and generate plots.

3D animations were created using the open source visualisation tool VisIt. This enabled the propagation of microwaves past inhomogeneities in time to be studied and provided additional physical insight.

Chapter 5

Propagation of microwaves through filamentary density perturbations

5.1 Motivation

While propagation through a homogeneous or slowly-varying monotonic plasma density profile is well understood and can be calculated analytically or using a ray-tracing method, turbulent or otherwise perturbed profiles require detailed numerical modelling using a full-wave method. The EMIT-3D code described in previous chapters is therefore applied to this problem in this chapter, since cases with 3D physics can arise.

The large fluctuations observed in SAMI data (see Subsection 1.3.2) during inter-ELM periods demand explanation. One candidate is the influence of inter-ELM filaments on the mode conversion and propagation of the emission. There is evidence for the presence of filamentary blob structures at the edge of nearly all tokamaks, as well as alternative configurations such as stellarators and reversed-field pinches; they are responsible for a significant fraction of cross-field transport at the edge of fusion-relevant plasmas [11]. They have been observed between ELMs on MAST [12], and since their density range has been measured to be $5 \times 10^{17} - 2 \times 10^{18}$

m^{-3}, some filaments will have peak densities close to or above cutoff, particularly at the lower end of the SAMI frequency range. This chapter quantifies the effect of typical MAST inter-ELM filaments by varying filament parameters to investigate their interactions with microwave beams.

Previous simulations have been carried out to study RF scattering from cylindrical filaments for ion cyclotron resonance frequency (ICRF) and lower hybrid (LH) heating applications using a full-wave method; Myra and D'Ippolito [61] found that, for ICRF fast waves, only a small amount of scattering and thus power loss occurred. However, mode conversion from fast waves into LH slow waves was predicted to be a cause of power loss when the filament scale length was comparable to the slow wave wavelength, although this result was qualitative rather than quantitative due to the breakdown of the expansion used. A more significant degree of scattering was observed with slow waves, with perturbations to the RF fields on the order of a wavelength even when filament radii were much smaller than this.

Other simulations have studied scattering from spherical blobs for EC and LH waves; using Fokker-Planck and ray-tracing methods, Tsironis et al. [62] concluded that, for ITER-relevant parameters and a 170GHz ECCD beam, a blob causing even small-angle scattering could have serious consequences for power deposition at the cyclotron harmonics due to the distances of several metres travelled by the beam. Hizanidis et al. [63] used geometric optics analysis to come to a similar conclusion, with scattering angles of $1^\circ - 4^\circ$ for both O- and X-modes calculated. Ram, Hizanidis and Kominis [64] used a full-wave method to study spherical blob scattering and observed forward scattering effects that were more significant than backscattering, and were enhanced with increasing density and scale length.

Emission can be obliquely incident with a finite width along the filament axis, so this scattering problem is in some respects inherently 3D; this also applies to the use of Doppler reflectometry to observe tokamak filaments [65]. EMIT-3D is therefore used to carry out these simulations in 3D. By comparison with the 2D full-wave code IPF-FDMC [49], the cases in which 3D treatment is required are determined.

5.2 Edge filaments

In general, during tokamak operation, transport of heat and particles across the scrape-off layer (SOL), perpendicular to the magnetic fieldlines, is dominated by non-diffusive transport due to coherent plasma structures variously known as filaments (the nomenclature used here), blobs, intermittent plasma objects (IPOs) and plasmoids [66]. Experimental observation has shown this to be the case for both L- and H-mode discharges (see Section 1.2.1) - for example, probe data from the DIII-D tokamak showed these structures to be responsible for $\sim 50\%$ of transport at all radii for both modes of operation [67]. This section provides a brief summary of filament observations.

5.2.1 L-mode

Filaments during L-mode operation were first observed in the early 1980s, with early studies [68] using fast cameras to image D_α light produced by gas puffing on the ASDEX and DITE tokamaks. This showed the presence of filamentary structures, elongated in the toroidal direction. Observations on the TFTR tokamak characterised these structures in more detail, measuring poloidal spacings of ~ 3 cm for a 0.9 MA discharge and ~ 5 cm for 1.4 MA, both with 5 MW of neutral beam heating power [69]. Furthermore, only small toroidal angles were found between filaments and fieldlines, suggesting that filaments tend to align along the field.

Improvements in diagnostic capabilities allowed, for example, the use of an ultrafast (250 kHz) camera to track the radial motion of filaments on the Alcator C-Mod tokamak [70] during intermittently occuring radial transport events, finding radial velocities of ~ 0.5 km/s. Observations of L-mode filaments were made in spherical as well as large aspect-ratio tokamaks; NSTX in 2001 [71] and later MAST [66]. Filaments on STs were found to be quantitatively similar, with perpendicular spacings of several centimetres and close alignment to the magnetic field [71]. Toroidal velocities were measured at $3 - 5$ km/s [66]. L-mode filament densities have been measured and are typically somewhat low in comparison to the pedestal; on MAST, they are $\sim 6 \times 10^{17} - 5 \times 10^{18}$ m^{-3} [12].

5.2.2 Edge localised modes (ELMs)

Since the first H-mode experiments on ASDEX [6], the improved plasma confinement has consistently been seen to be degraded by fast-growing (~ 200 μs) modes at the edge known as ELMs, causing a periodic relaxation of the edge density gradient and the loss of large quantities of stored energy and particles. The negative effect on tokamak performance alongside the high power loading on the divertor and outer wall has drawn significant research interest to this subject.

Measurements from MAST showed ELMs to be associated with field-aligned filamentary structures [72]. However, these differ significantly from L-mode filaments in their spatial size ($\sim 7.5 - 15$ cm [72]) and density — Thomson scattering data from MAST [73] and DIII-D [74] shows them to have high densities which are comparable to the pedestal, $\sim 2 - 3 \times 10^{19}$ m^{-3}. Fast cameras have been used to track ELM motion and found their toroidal velocity to decrease from 13 to 2 km/s and radial velocity to increase from 2 to 9 km/s as they expand radially over their ~ 200 μs lifetime [73].

5.2.3 Inter-ELM

Recently, the filaments present during H-mode but between ELMs have been investigated experimentally [12]. Compared to L-mode filaments, they have a lower D_α and mean density, but in spatial width and toroidal mode number, they are intermediate between L-mode and ELM filaments. In a similar fashion to L-mode filaments, they are intermittently seen to travel radially outwards at a constant velocity of 1 - 2 km/s. See Figure 5.1 for a comparison.

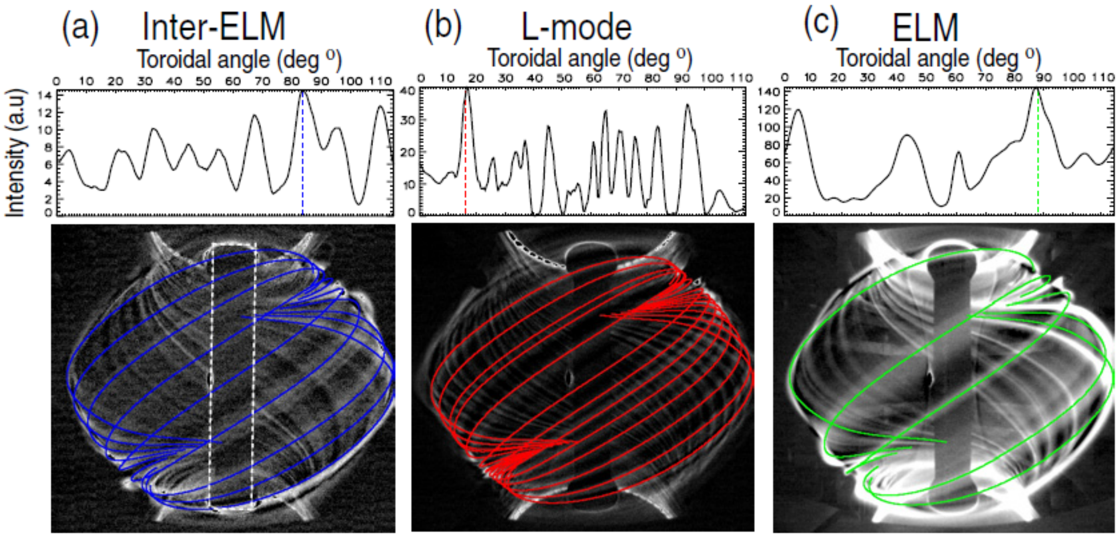

Figure 5.1: Intensity traces of mapped field lines as a function of the toroidal angle spanning the centre column for (a) inter-ELM, (b) L-mode and (c) ELM filaments from the same shot. Beneath these, detected filaments are projected onto the corresponding full view camera images. Reproduced with permission from [12]

5.3 Simulation setup

5.3.1 Geometry

The simulations were carried out with a vacuum background. Onto this was superimposed a filament, modelled as a cylindrical density perturbation with a Gaussian profile, its axis in the x-direction:

$$n_e(y,z) = n_{e,\text{peak}} \exp\left(\frac{-(y-y_0)^2-(z-z_0)^2}{w^2}\right) \tag{5.1}$$

Results were obtained by exciting a linearly polarised (in the x-direction) O-mode beam at the $z = 0$ plane, a distance $z = 7\lambda_0$ from the cylinder axis, where λ_0 is the vacuum wavelength of the incident beam. This was a Gaussian beam with a width of $2\lambda_0$ and its waist located in the antenna plane, hence having the following electric field intensity distribution at $z = 0$:

$$E_x(x, y) = E_0 \exp(\frac{-(x - x_0)^2 - (y - y_0)^2}{(2\lambda_0)^2}) \tag{5.2}$$

Filaments in tokamaks are elongated along the background magnetic field lines [12]. As this investigation concerned the simplest possible case of perpendicular injection onto a filament of an O-mode beam ($\mathbf{E} \parallel \mathbf{B}_0$ and hence polarised parallel to the filament axis, as seen in Equation 5.2), the background magnetic field was neglected for practical benchmarking reasons. In a 2D geometry, this has no effect on the results obtained, since the direction of the oscillating E-field is not affected by the density perturbation.

In order to allow improved benchmarking and comparison between EMIT-3D and IPF-FDMC, the magnetic field is also neglected in the 3D calculations. Its incorporation leads to additional deviation from the 2D results since the wave is no longer a plane wave into the direction of the magnetic field but has a finite extent. Hence, the electric field vector is no longer "forced" to oscillate exactly parallel to B0, but with a finite angle, which results in slightly different scattering. This is a 3D effect which will be explored in future publications.

The simulation was then allowed to run in the time domain, as the beam propagated through the grid and interacted with the density perturbation. It was allowed to run until reaching a steady state (wave fields were monitored over time to ensure a steady and converged solution), typically after $\sim$ 3000 timesteps, the scattered electric field was summed over several cycles at the x-y backplane (also $z = 7\lambda_0$ from the cylinder). An RMS value of this field could thus be calculated in order to obtain a power distribution.

A relatively small spatial step of $\Delta x = \lambda_0/50$ was chosen to ensure an accurate description of the interaction with the density gradients within the filament structure. The total grid size used for each scan is stated in the Results section. The timestep is fixed using a stable value of Courant number $C = 0.5$; for a filament density of $n_{e,\mathrm{peak}} = 0.8n_{e,\mathrm{crit}}$ this results in a value of $\Delta t = \tau_p/18$ where τ_p is the plasma period at peak density.

Simulations were run on a computer cluster to make use of the parallel programming features of EMIT-3D. A typical run for 3000 timesteps over 80 parallel processors had a runtime of ~ 8 hours.

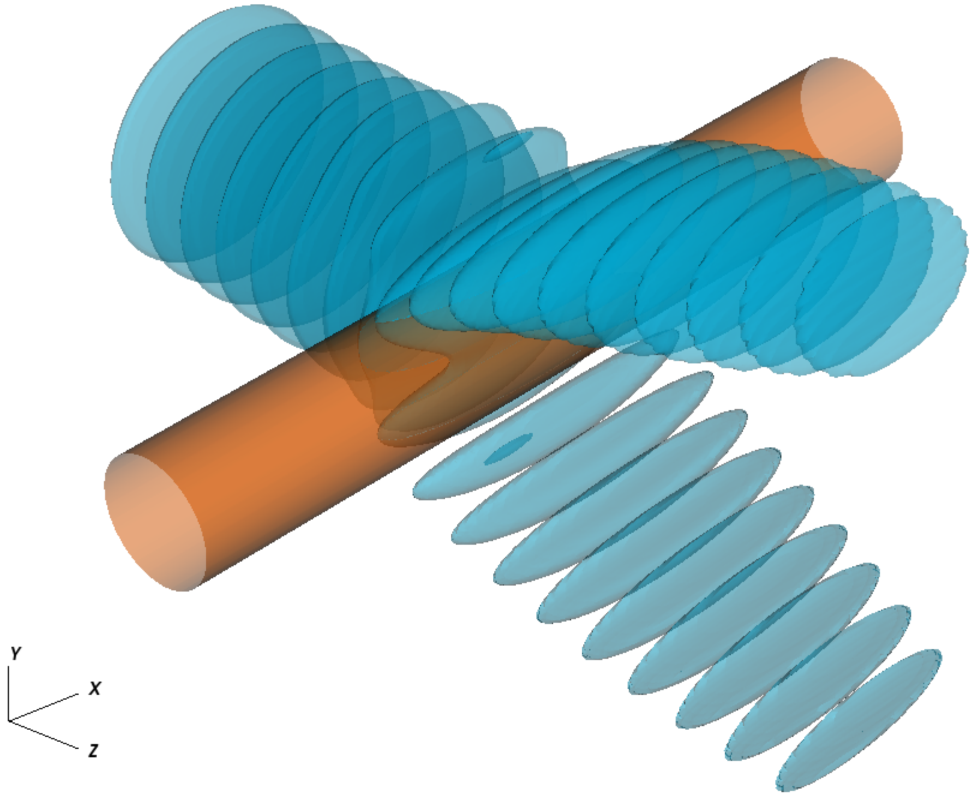

Figure 5.2: 3D surface plot of EMIT-3D output showing simulation setup. Blue: $E_x = 0.41A$ surface of beam, orange: $X = 0.25$ surface of background density. Incident beam is excited at left-hand plane, scattered by filament at centre of domain, then propagates as two scattered beams towards right-hand plane and is absorbed at boundary

5.3.2 Scaling to experiment

To ensure experimental relevance, physical parameters for the investigation were obtained from Ben Ayed *et al.* (2009) [12]. Langmuir probe measurements found that MAST inter-ELM filaments have a density range of $n_e = 5 \times 10^{17} - 2 \times 10^{18}$ m^{-3}. For experimentally relevant frequencies of $10 - 35$ GHz, this corresponds to a range in the parameter $n_{e,\text{peak}} = 0.03 n_{e,\text{crit}} - 1.61 n_{e,\text{crit}}$.

Filament widths, defined in [12] as "twice the difference between the maximum and lowest neighbouring minimum", were measured in the range $w = 5 - 30$ cm, with a peak at 13 cm and mean at 16 cm. Corresponding Gaussian widths are estimated to be around a quarter of this, giving a range of $1.3 - 7.5$ cm. The frequencies of interest correspond to vacuum wavelengths $\lambda_0 = 0.9 - 3.0$ cm, so a range in Gaussian widths of $w = 0.4\lambda_0 - 8.8\lambda_0$ is possible.

5.4 Analysis

To estimate the degree of scattering, the mean μ_P and standard deviation σ_P of the backplane power distribution $P(x, y)$ were calculated in both x- and y-directions as follows (e.g. for y):

$$P_{tot} = \sum_{x_0}^{N_x} \sum_{y_0}^{N_y} P(x, y) \tag{5.3}$$

$$\mu_{P,y} = \frac{1}{P_{\text{tot}}} \sum_{x_0}^{N_x} \sum_{y_0}^{N_y} [y \cdot P(x, y)] \tag{5.4}$$

$$\sigma_{P,y} = \sqrt{\frac{2}{P_{tot}} \sum_{x_0}^{N_x} \sum_{y_0}^{N_y} [(y - \mu_{P,y})^2 \cdot P(x, y)]} \tag{5.5}$$

where N_x, N_y are the total number of gridpoints in the x- and y-directions respectively. These quantities were compared against their values $\mu_{P,\text{vac}}$, $\sigma_{P,\text{vac}}$ for a beam propagating only through vacuum. The point of maximum emission $y_{\max}$

was also recorded. Parameters were scanned through experimentally relevant values over a number of runs, and the degree of scattering quantified.

5.5 Results

5.5.1 Position scan

A grid of $496 \times 1204 \times 736$ gridpoints was used for this scan. The position y_{fil} of the centre of a filament with its axis in the x-direction (normal to beam propagation) was varied relative to the beam axis in the y-direction. The filament's peak electron density was kept constant at $n_{e,\text{peak}} = 0.8 n_{e,\text{crit}}$, and its Gaussian width at $w = 1.0\lambda_0$. Backplane power distributions are plotted in Figure 5.3.

Scattering in this case, as could be expected due to the inherently 2D nature of the problem, was only observed in the y-direction - in the x-direction, the beam profile remained close to the original Gaussian of the source. That is, no scattering out of the plane was observed. The peak σ_P in the y-direction (Figure 5.4), observed when the filament and beam axes coincide, is greater than the result for vacuum by a factor of 3. As their separation increases past $2\lambda_0$, power distributions with $\sigma_P < \sigma_{P,\text{vac}}$ are observed, suggesting that the filament may be acting to focus the beam, although this is only a small effect.

The point of maximum emission y_{max} (Figure 5.5) was maximally displaced by a filament centred on the beam axis, with two equal maxima located at $y = \pm 3.88\lambda_0$. As the filament moved away, this became a single maximum which returned towards, and then slightly beyond, the centre point at larger separations. A single beam was recovered, but its shape was still influenced by the presence of the filament, with a dual-lobed structure as can be seen in Figure 5.3 for $y_{\text{fil}} = 4\lambda_0$.

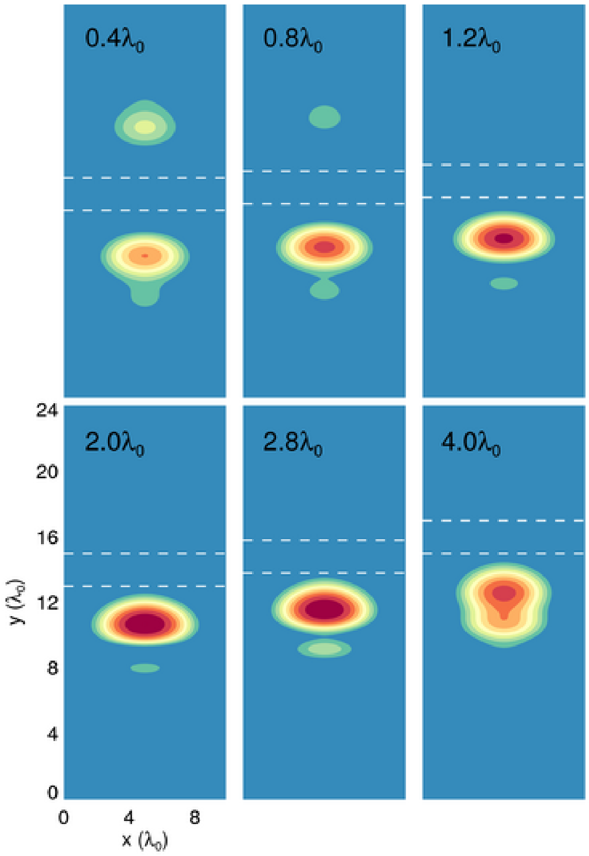

Figure 5.3: Distribution of $\langle E^2 \rangle$ ($\propto$ power) on backplane for position scan. y_{fil} shown on each plot. Dashed lines indicate the $\frac{1}{e}$ extent of the filament density projected onto the backplane. Contours on a log scale. Spatial coordinates shown on axes of lower left image

As the separation increased past $4\lambda_0$, the lower emission lobe became more intense than the upper and hence a discontinuity is seen in the plot of $y_{\max}$. This shows that a filament passing across a beam will in fact cause a series of two perturbations to its maximum, rather than the one which might naively be expected. The greatest value of $y_{\max}$ (with filament aligned to the beam axis) corresponded to a scattering angle of 26°.

This scan was also carried out in 2D using IPF-FDMC for benchmarking and comparison purposes, with all parameters identical ($\Delta x, \Delta t, \lambda_0$ etc.) to enable as close a comparison as possible. 2D results are plotted in black on Figures 5.4 and 5.5. Excellent agreement is shown; while it is exact for $y_{\max}$, a small discrepancy in calculated σ_P is observable for larger scattering angles. However, this is due to necessary differences in the method of analysis between 2D and 3D cases rather than numerical differences.

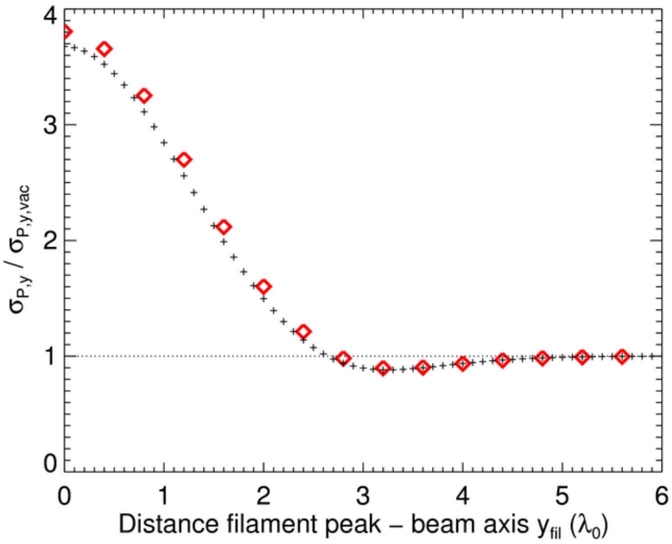

Figure 5.4: Standard deviation $\sigma_{P,y}$ in y-direction for position scan. Dashed line for case without filament. Red diamonds: EMIT-3D, black crosses: IPF-FDMC

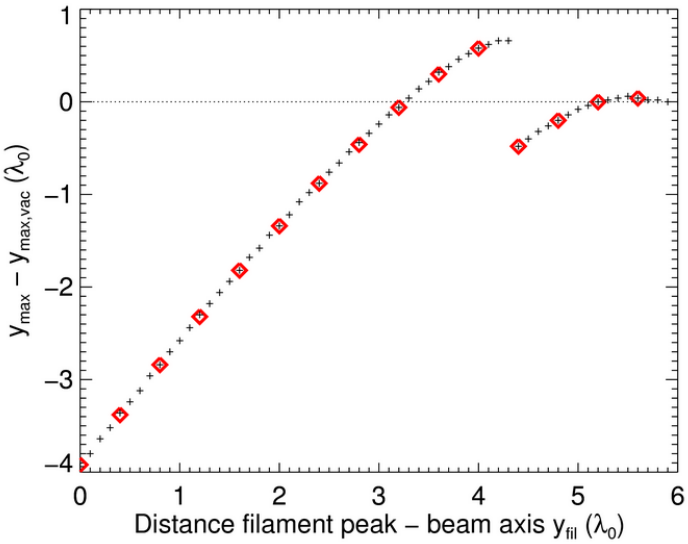

Figure 5.5: Shift of maximum emission point y_{max} in y-direction for position scan. Dashed line for case without filament. Red diamonds: EMIT-3D, black crosses: IPF-FDMC

5.5.2 Density scan

Again, a grid of 496 × 1204 × 736 gridpoints was used. The filament position was held constant on the beam axis and $n_{e,\text{peak}}$ varied through experimentally relevant values. Again, the scattering observed was 2D in nature — see Figure 5.6. The standard deviation σ_P (Figure 5.7) increased as the density was increased while still below cutoff, reaching a maximum with $n_{e,\text{peak}} = n_{e,\text{crit}}$. As the peak density rose above cutoff, the degree of scattering saturated and remained nearly constant, as did the position of the symmetric emission maxima (Figure 5.8). A maximum scattering angle of 32° was not exceeded with increasing $n_{e,\text{peak}}$.

However, the total power reaching the backplane was significantly decreased. Below cutoff, a smaller decrease of total power by $\sim 9\%$ was observed due to the beam having scattered beyond the maximum y-extent of the computational domain. As cutoff was reached and exceeded at the filament centre and backscattering began to play a significant role, the total backplane power decreased to $\sim 40\%$ of its original value.

Again, excellent agreement of EMIT-3D with IPF-FDMC is seen in Figures 5.7 and 5.8.

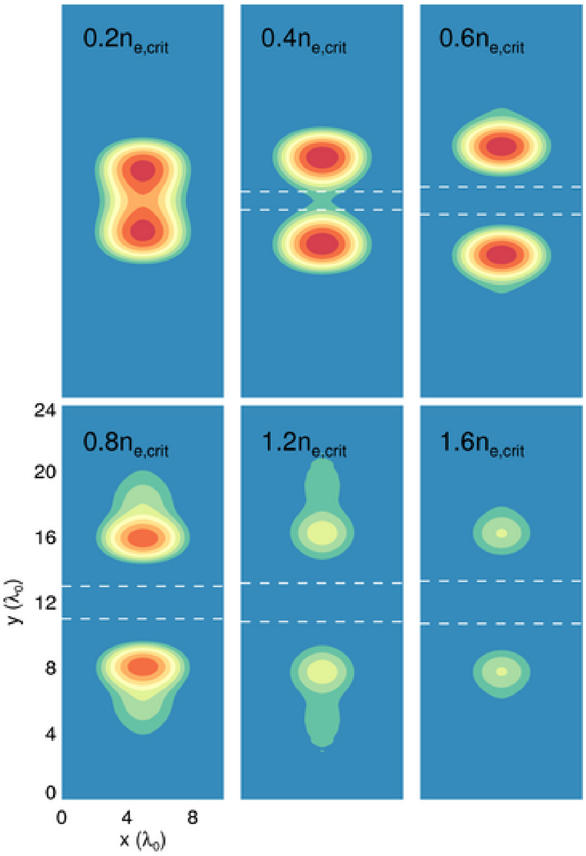

Figure 5.6: As Figure 5.3 for filament density scan. $n_{e,\text{peak}}$ shown in terms of $n_{e,\text{crit}}$. Dashed lines at density previously shown, $0.8n_{e,\text{crit}}/e$ (not visible for $n_{e,\text{peak}} = 0.2n_{e,\text{crit}}$ since this density is not reached). Contours on a log scale. Spatial coordinates shown on axes of lower left image

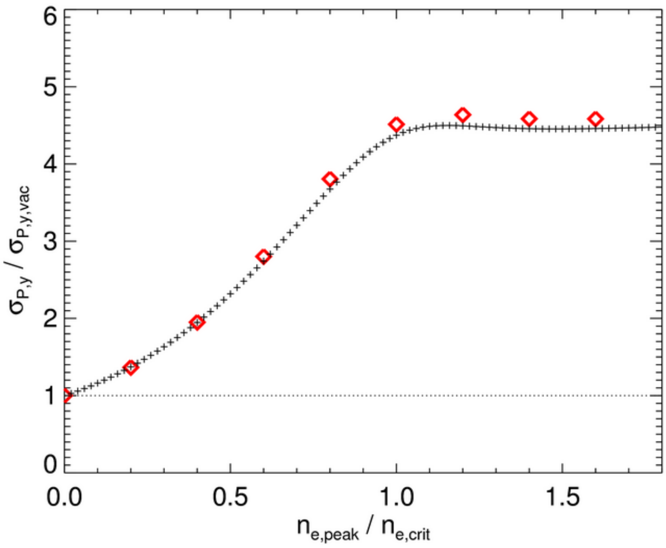

Figure 5.7: Standard deviation $\sigma_{P,y}$ in y-direction for density scan. Red diamonds: EMIT-3D, black crosses: IPF-FDMC

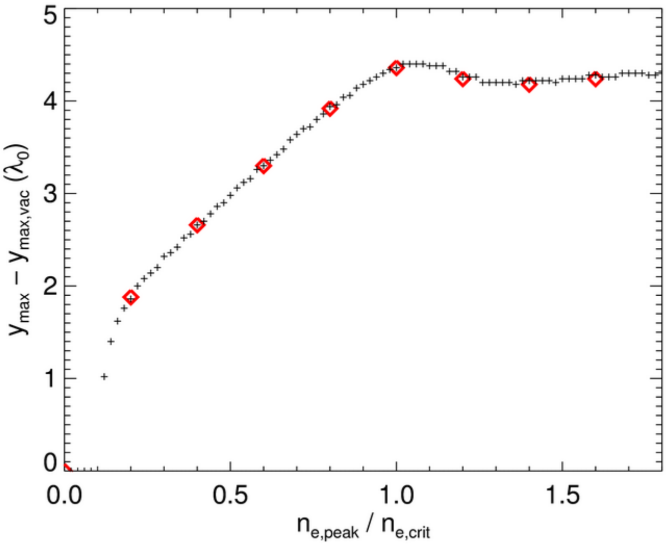

Figure 5.8: Shift of maximum emission point $y_{\max}$ in y-direction for density scan. Red diamonds: EMIT-3D, black crosses: IPF-FDMC

5.5.3 Width scan

The grid dimensions remained at $496 \times 1204 \times 736$ gridpoints. The Gaussian width w of the filament was varied from $0 - 2.5\lambda_0$, with fixed peak density $n_{e,\text{peak}} =$

$0.8n_{e,\mathrm{crit}}$ (see Figure 5.9). For $w < 0.3\lambda_0$, almost no effect on $y_{\max}$ was observed (see Figure 5.11); however, a large increase in σ_y (see Figure 5.10) was observed for $w > \lambda_0$, with the point of maximum emission also diverging from the mean. A scattering angle of 47° was observed at $w = 2.5\lambda_0$, and this continued to increase for wider filaments.

Excellent agreement between codes was again observed.

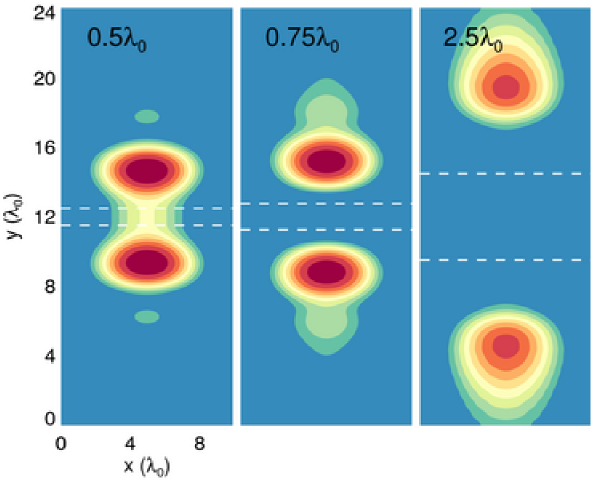

Figure 5.9: As Figure 5.3 for width scan. Widths shown in units of λ_0. Contours on a log scale. Spatial coordinates shown on axes of leftmost image

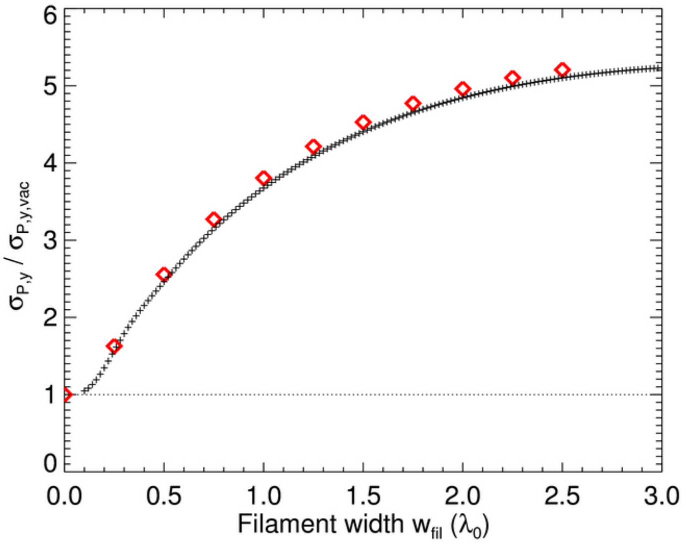

Figure 5.10: Standard deviation $\sigma_{P,y}$ in y-direction for width scan. Red diamonds: EMIT-3D, black crosses: IPF-FDMC

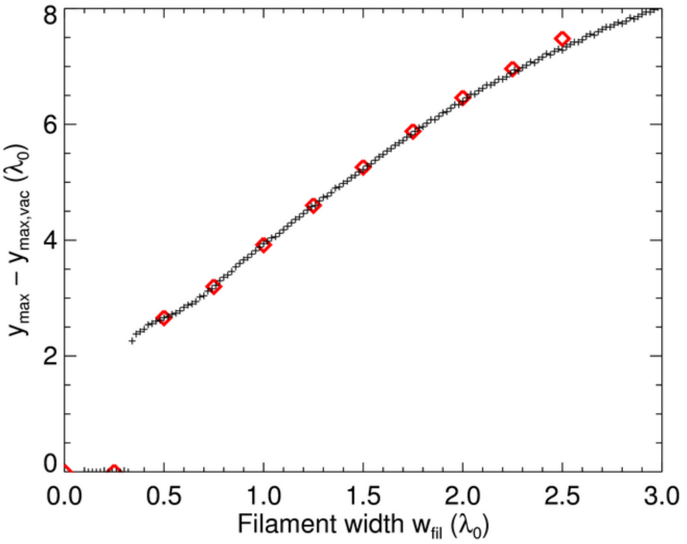

Figure 5.11: Shift of maximum emission point $y_{\max}$ in y-direction for width scan. Red diamonds: EMIT-3D, black crosses: IPF-FDMC

5.5.4 Angular scan

For this scan, a change in the dimensions of the grid to 605 × 1000 × 736 was made in order to fully capture the backplane distribution. The incident angle to the normal, θ_i, of the beam on the filament in the x-z plane was varied between $0° - 80°$ (Figure 5.12). As for the position scan, filament density and width were held constant at $n_{e,\mathrm{peak}} = 0.8 n_{e,\mathrm{crit}}$ and $w = 1.0\lambda_0$.

For as simple a picture of this scattering effect as possible, consistency was maintained with the earlier scans by keeping $\mathbf{B}_0 = 0$. A test run was carried out with a finite $\mathbf{B}_0$ along the filament axis, but only small deviations were observed from the unmagnetised result. A more sophisticated analysis of the magnetised 3D scattering effect is outside the scope of this chapter but is a future topic for investigation with EMIT-3D.

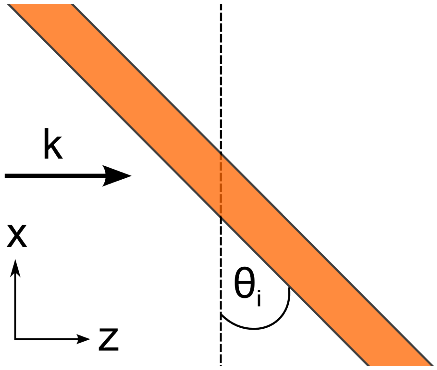

Figure 5.12: Schematic of angular scan in xz plane. Filament tilted at angle θ_i is shown in orange, k is wavevector of incident beam

As the beam moved away from normal incidence, it encountered an increasingly shallow density gradient and so refractive effects began to dominate over scattering. This resulted in a rotation of the emission patterns, with the two spots coalescing into a single maximum for large angles - see Figure 5.13.

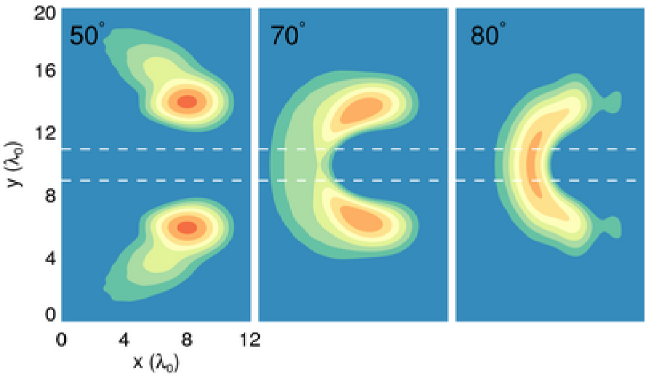

Figure 5.13: As Figure 5.3 for angular scan. Incident angles in x-z plane shown. Contours on a log scale. Spatial coordinates shown on axes of leftmost image

Although the maximum emission point $y_{\max}$ shifted in both x- and y-directions, the scattering angle only increases slightly (29° − 31°). This is an example of a genuinely 3D effect.

The effect of oblique incidence on the beam's wavefront can be observed in more detail from the 3D plots in Figures 5.14 and 5.15 — compare these images to Figure 5.2. Figure 5.14 shows the leading wavefronts beginning to distort and rotate as the beam first encounters the density perturbation at an angle of 50°. Figure 5.15 shows a frame from a later timestep, as the beam has propagated past the perturbation. Splitting into two beams, as well as rotation, has occurred and the shift of beam power in the rightwards direction (from the viewpoint into the negative z-direction shown) along the filament axis is observable.

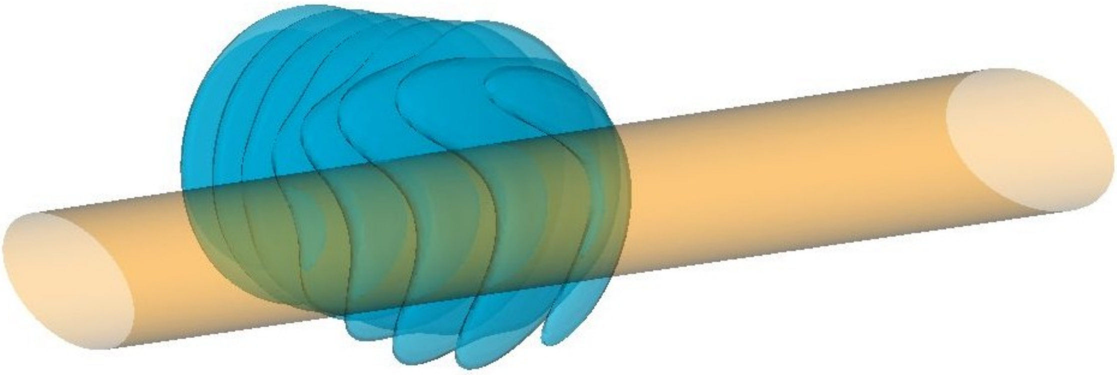

Figure 5.14: 3D surface plot of EMIT-3D output at 50° angle of incidence, early timestep — E-field and n_e contours plotted as for Figure 5.2.

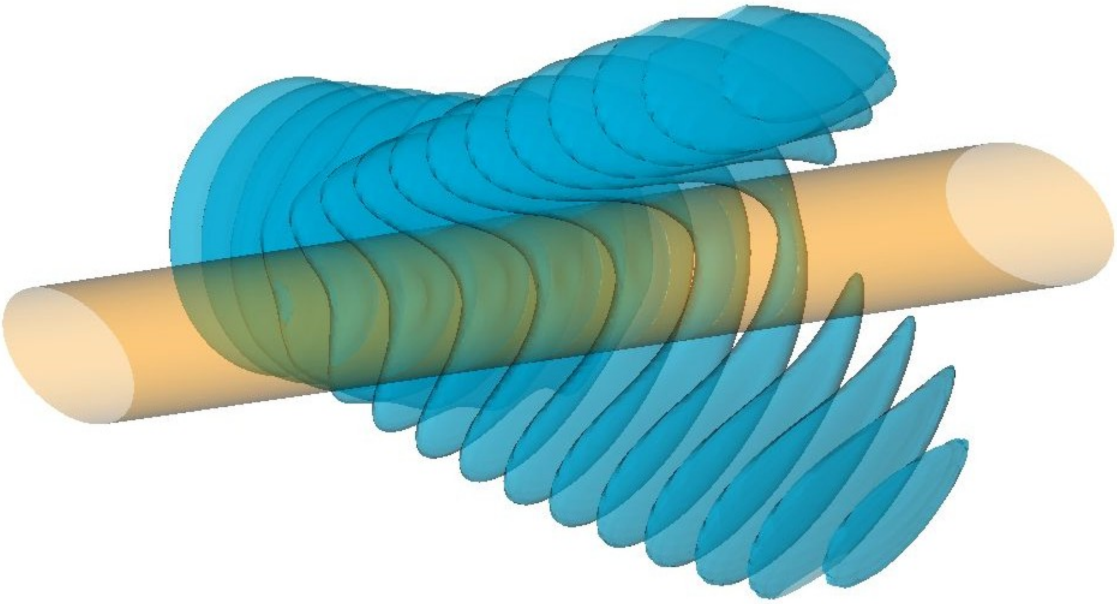

Figure 5.15: 3D surface plot of EMIT-3D output at 50° angle of incidence, later timestep — E-field and n_e contours plotted as for Figure 5.2.

5.6 Discussion

These results show the synergistic effects of two filament parameters, density and width, on the observed scattering angle. While filaments with widths of several times the beam wavelength can cause large deviations at higher frequencies (e.g. a filament of Gaussian width 2.5cm, close to the mean width for MAST, will scatter a 30 GHz beam by 47°), filament density becomes an important effect at lower frequencies, even for underdense filaments (e.g. a filament of peak density 1.0×10^{18} m^{-3}, again typical for MAST, will scatter a 10 GHz beam by 26°).

In comparison to the results discussed earlier from the previous studies [61] - [64], scattering angles are around an order of magnitude larger; however, the beam wavelengths studied here are also an order of magnitude larger and on the order of the filament width and so this result is not unexpected; MAST, rather than ITER parameters were investigated here. In agreement with [64], forward scattering was found to be more significant than backscattering in causing power loss, unless the filament is overdense. An important difference in simulation setup is the use in this chapter of Gaussian-profiled filaments, as opposed to the step-function in density used in previous work; more detailed comparison would require a similar profile to be used in EMIT-3D.

It is therefore shown that filamentary plasma structures can have a significant influence on the propagation of microwaves across a broad frequency spectrum, with consequences for both electron cyclotron diagnostics and heating. Since spherical tokamaks maintain plasma densities comparable to other tokamaks with a lower magnetic field and thus have lower electron cyclotron frequencies, these effects can be particularly important. In particular, inter-ELM filaments on MAST could be a source of fluctuation for the SAMI diagnostic, although further simulation and experimental comparison are required to quantify such a link.

By comparison with IPF-FDMC, the cases in which 2D simulation is justified have been determined. For normal incidence, minimal out-of-plane scattering was observed from EMIT-3D, verifying that 2D simulation, with its reduced computational time, is valid in this case. However, for oblique incidence, which is generally the case for emission diagnostics, 3D effects become important.

Chapter 6

Propagation of microwaves through turbulence

6.1 Motivation

The presence of turbulence in both the core and edge of a tokamak plasma has been measured experimentally many times [13] (see e.g. Figure 6.1). Since turbulence manifests in a tokamak as an ensemble of eddies extended along fieldlines, as opposed to a single scattering structure, its effect on an incident microwave beam will clearly differ from the cases explored in Chapter 5.

The performance of microwave emission diagnostics will be limited when edge turbulence is present; the defocusing caused affects both propagation and more complicated processes such as mode conversion [33]. Further, applications requiring a focused microwave beam such as EC heating and current drive can be impacted. It is therefore necessary to improve our understanding of this subject.

In this chapter, a full-wave study of microwave propagation through a realistic turbulent layer is carried out. This extends the previous chapter's investigation of microwave scattering from a single plasma filament or blob, and obtains important new results characterising turbulent scattering.

Previous attempts have been made to quantify the scattering effect of a turbulent layer on a microwave beam. An analytical example is that presented by Sysoeva et

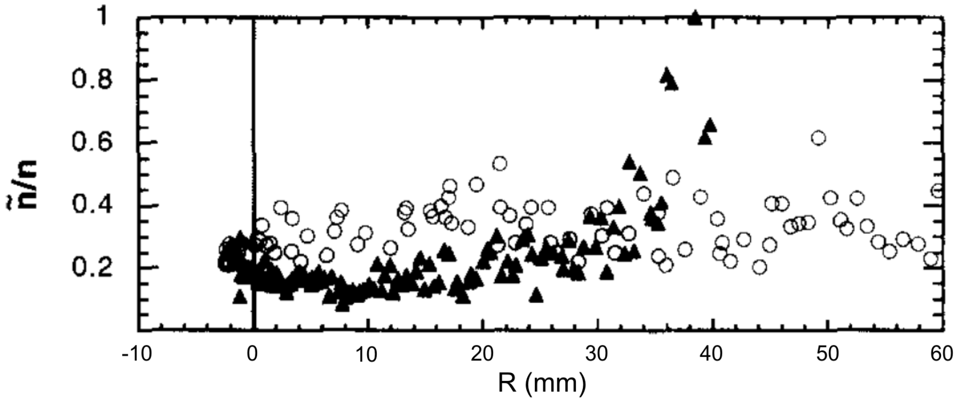

Figure 6.1: Fluctuation amplitude by radius [75] — measured on the DIII-D tokamak using a reciprocating Langmuir probe. Ratio of fluctuation amplitude to radius plotted against minor radius with respect to separatrix. Circles - L-mode, triangles - ELM-free H-mode

al. [76]; this derives an expression for the angular broadening of an O-mode beam travelling through a turbulent layer. In this chapter, to investigate the interactions between more realistic tokamak edge turbulence, a commonly-recognised turbulence model is solved numerically and used to initialise a set of EMIT-3D simulations.

A key result is the relative length scale at which microwave propagation will be most severely affected by turbulence. By varying the size of the turbulent structures between simulations, the relationship between beam wavelength and eddy size is explored.

6.2 Incorporating turbulent profiles

6.2.1 Artificial turbulence

Previous attempts to incorporate turbulent backgrounds into a microwave propagation model have relied on a statistical description (e.g. [33], [76]). A probability density function is used to approximate a region of turbulence with a desired energy spectrum and correlation length.

This approach can generate useful results but nonetheless remains somewhat ‘artificial’ and has clear deficiencies if a realistic picture of microwave propagation through a turbulent layer is to be obtained. A more rigorous approach is desired, in which turbulent density profiles can be used which are known to closely match edge turbulence in a tokamak.

6.2.2 Real turbulence

In a new approach, a turbulence code can be used to simulate realistic tokamak edge turbulence. The BOUT++ code [77] provides a flexible framework in which multiple fluid models can be implemented and is used in this work.

The Hasegawa—Wakatani model [78] is used for tokamak edge turbulence simulations. It describes electrostatic resistive drift wave turbulence and simulates the coupling between vorticity and density. A density gradient drives the evolution of turbulent eddies from an initially unperturbed plasma with a constant background magnetic field.

The following set of fluid equations are used:

$$\frac{\partial \zeta}{\partial t} + \{\varphi, \zeta\} = \alpha(\varphi - n) \tag{6.1}$$

$$\frac{\partial n}{\partial t} + \{\varphi, n\} = \alpha(\varphi - n) - \kappa \frac{\partial \varphi}{\partial y} \tag{6.2}$$

where φ is potential, $\zeta = \nabla^2 \varphi$ is the vorticity, $\alpha = -T_e/(\eta n_0 \omega_{ci} e^2)\frac{\partial^2}{\partial z^2}$ is the adiabacity operator describing the parallel electron response and $\kappa = -\frac{\partial}{\partial x} \log n_0$ is the strength parameter, determined by the background density gradient. As usual, the Poisson bracket

$$\{a, b\} = \frac{\partial a}{\partial x}\frac{\partial b}{\partial y} - \frac{\partial a}{\partial y}\frac{\partial b}{\partial x}$$

These equations are typically solved numerically using a suitable code.

6.3 EMIT-3D simulations using turbulence

To obtain usable data for microwave-turbulent scattering interaction simulations, a 2D BOUT++ simulation using the Hasegawa-Wakatani model described above was carried out. A value of $\kappa = 1$ (see 6.2) is specified, producing the density gradient which drives the turbulence, and the adiabacity operator $\alpha = 0.5$. Initial perturbations consisting of a mix of mode numbers with pseudo-random phases are applied, iterations are begun and the mean turbulent energy increases over time; after a sufficient number of timesteps, the turbulence saturates and the mean turbulent energy no longer grows. The simulation is allowed to run until this point is reached, and then continues running while a series of snapshots are taken of the resulting turbulent eddies.

At each of these snapshots, turbulent density fluctuation data, with values both positive (accumulation) and negative (rarefaction) is written to an output array (plotted in Figure 6.2). This data can then be used as an input background density profile for an EMIT-3D simulation by superimposing these eddies onto a homogeneous plasma background. Although a gradient in plasma density was necessary in order to drive the turbulence in BOUT++, a homogeneous plasma background is used here in order to focus only on characterising the scattering effect.

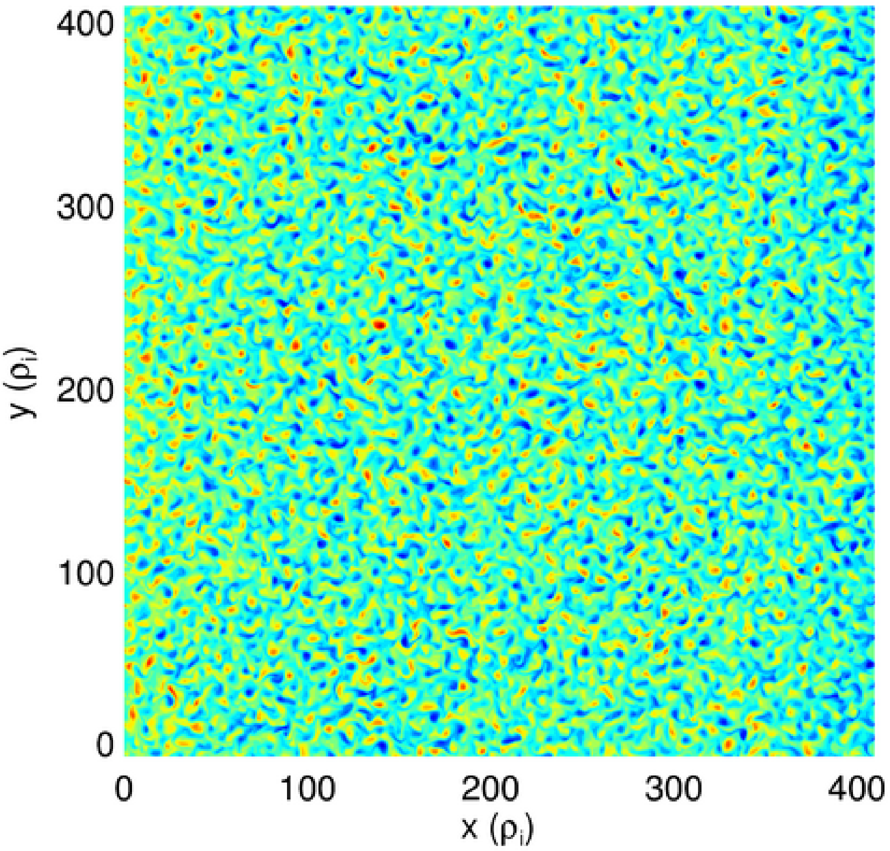

Figure 6.2: Full extent of BOUT++ turbulent simulation using Hasegawa-Wakatani model. Red: increase in density, blue: decrease in density

First, the BOUT++ output data is interpolated to the EMIT-3D grid. This is the point at which an important parameter can be set; the ratio of ion Larmor radius to the beam vacuum wavelength (ρ_i/λ_0). This gives a measure of the turbulent scale length; by varying this parameter, the effect of different turbulent structure sizes on a beam can be investigated.

Only a portion of the full simulated domain shown in Figure 6.2 is required for each EMIT-3D simulation. A window function using hyperbolic tangents is applied in order to select a turbulent region of given width:

$$n_e(y,z) = n_0 + A_{\text{fluc}} n_{\text{fluc}}(y,z) \frac{(\tanh(z - z_a) + 1)(\tanh(z_b - z) + 1)}{4} \tag{6.3}$$

where $n_{\text{fluc}}(y,z)$ is the turbulent fluctuation data from file, A_{fluc} is the fluctuation amplitude with respect to the background density and z_a and z_b are the start and end points in the z-direction of the turbulent layer. The fluctuations were simply extended in the x-direction, as tokamak turbulence is extended along fieldlines.

By varying A_{fluc} at this stage, the fluctuation amplitude can easily be scaled.

6.4 Results and interpretation

A set of EMIT-3D simulations were carried out using this turbulence data. Example views in the yz plane can be seen in Figures 6.3, 6.5, 6.7 and 6.9. Each of these shows a window of a single given turbulence snapshot (plotted in red and green contours) with a microwave beam (electric field value out of the page in background contour plot) propagating across it. Each plot is at a different representative value of ρ_i/λ_0 and the change in structure size from one simulation to the next depending on this parameter can be seen.

In order to quantify the structure size, autocorrelation calculations on the BOUT++ datasets were carried out. Average turbulent structure size (s), defined as the average distance between minima in density, and ion Larmor radius (ρ_i) were found to have a linear relationship, allowing the following scaling to be used:

$$s = 1.59\rho_i \tag{6.4}$$

Data is therefore plotted in terms of structure size rather than ρ_i as it is a more meaningful physical parameter from the perspective of a microwave interaction study.

In the simulations carried out, the background density $n_0 = 0.5n_{e,\text{crit}}$. The fluctuation amplitude A_{fluc} was selected such that $(\tilde{n})_{\text{RMS}}/n = 0.02$; the RMS value of the fluctuation amplitude was 2% of the background density. As in the previous chapter, Courant number $S = 0.5$, vacuum wavelength λ_0 is 50 gridpoints and since an O-mode wave is launched with $\mathbf{E} \parallel \mathbf{B}_0$, the background magnetic field can be neglected.

The distances $z_a = 1\lambda_0$, $z_b = 4\lambda_0$; that is, the beam propagates through a layer of homogeneous plasma of thickness λ_0, through a turbulent layer of thickness $3\lambda_0$ and through another layer of homogeneous plasma of thickness λ_0 before having its electric field value recorded at the backplane.

After allowing simulations to reach a steady state, an averaging technique over several wave periods is applied to the electric field values at the backplane as in Chapter 5. This results in a backplane distribution of the time-averaged electric field value, which can be further analysed.

Example backplane (xy) plots of E can be seen in Figures 6.4, 6.6, 6.8 and 6.10, showing the shift in beam power in both dimensions as opposed to the unperturbed case. Each of these corresponds to the proceeding yz plane plot.

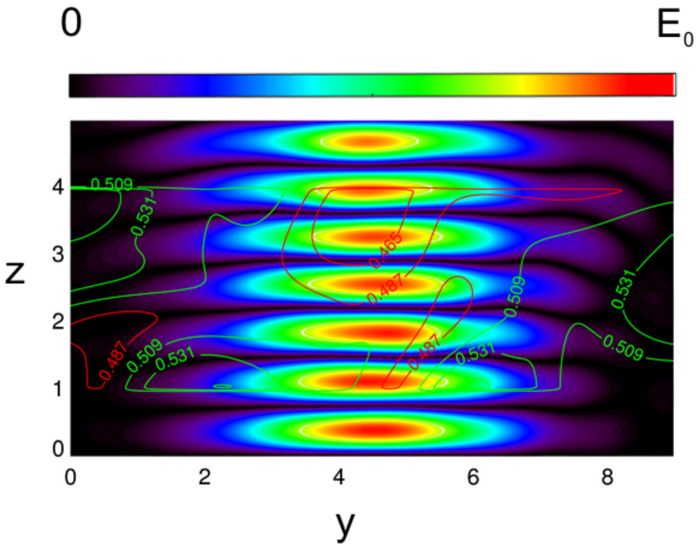

Figure 6.3: yz-plane view of turbulent scattering simulation with $\rho_i = 0.5\lambda_0$. Absolute E-field values of microwave beam plotted in background; density perturbation contours in foreground (green - positive, red - negative). Axes normalised to λ_0

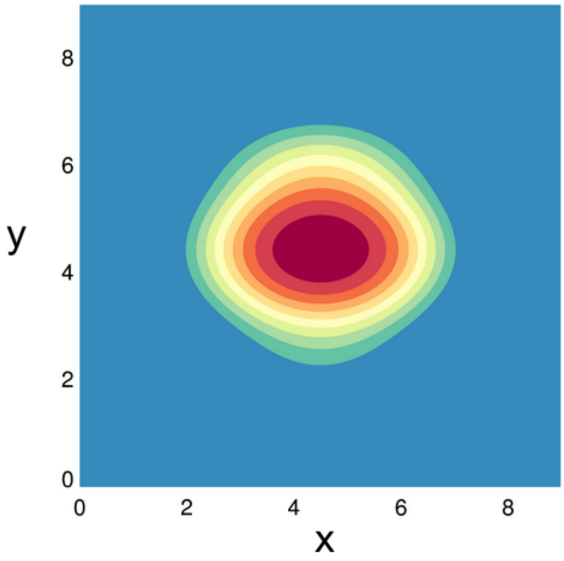

Figure 6.4: Backplane (xy) view of turbulent scattering simulation with $\rho_i = 0.5\lambda_0$. Time-averaged value of E-field is plotted. Axes normalised to λ_0

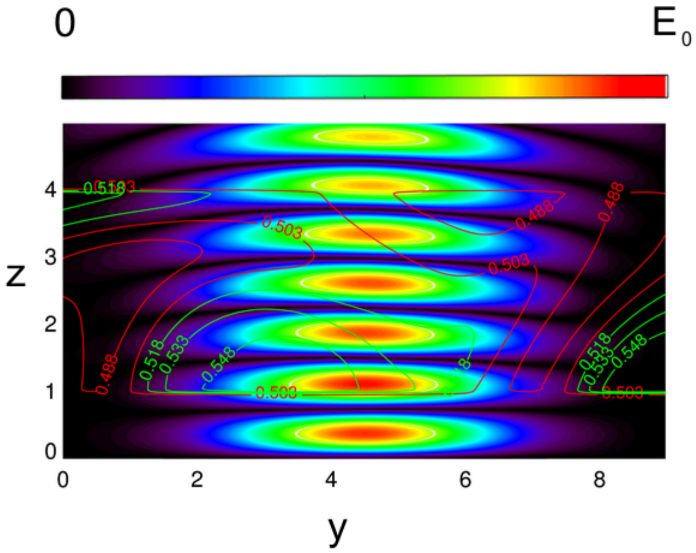

Figure 6.5: yz-plane view of turbulent scattering simulation with $\rho_i = 0.75\lambda_0$. Absolute E-field values of microwave beam plotted in background; density perturbation contours in foreground (green - positive, red - negative). Axes normalised to λ_0

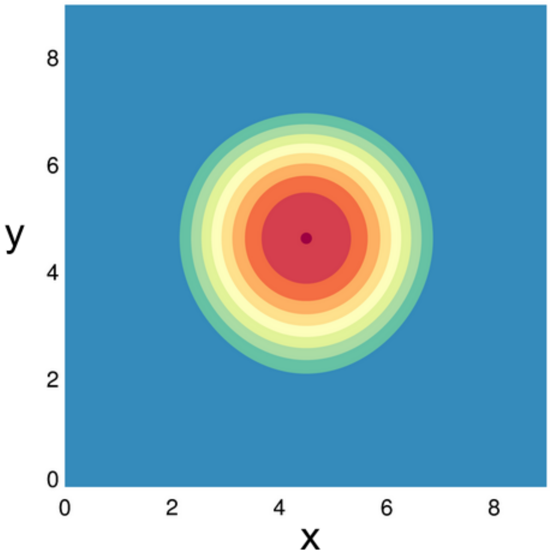

Figure 6.6: Backplane (xy) view of turbulent scattering simulation with $\rho_i = 0.75\lambda_0$. Time-averaged value of E-field is plotted. Axes normalised to λ_0

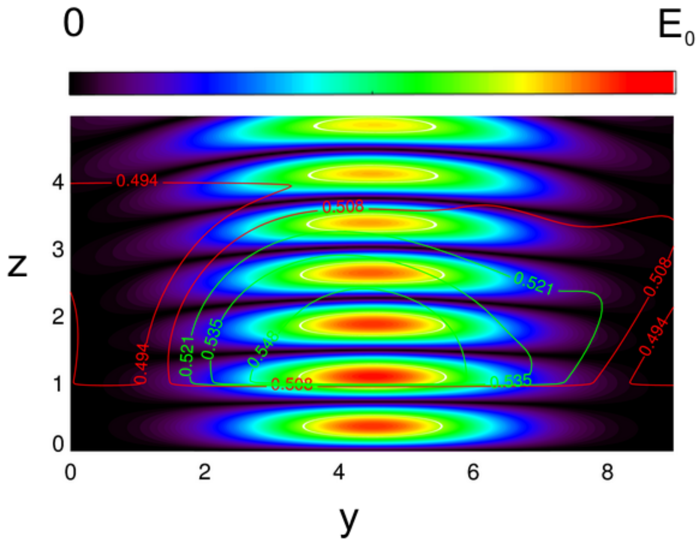

Figure 6.7: yz-plane view of turbulent scattering simulation with $\rho_i = 1\lambda_0$. Absolute E-field values of microwave beam plotted in background; density perturbation contours in foreground (green - positive, red - negative). Axes normalised to λ_0

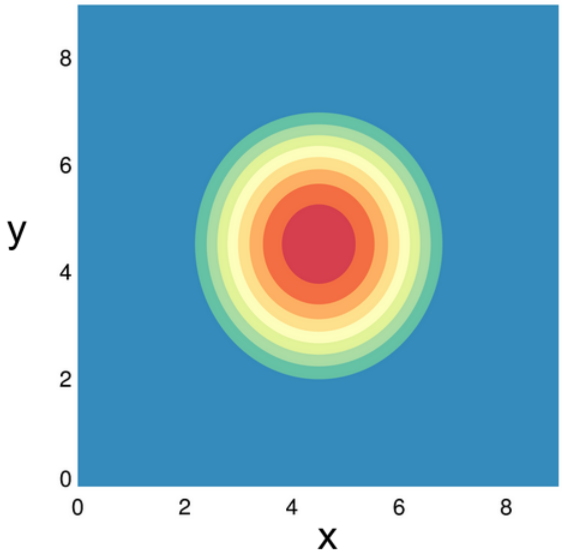

Figure 6.8: Backplane (xy) view of turbulent scattering simulation with $\rho_i = 1\lambda_0$. Time-averaged value of E-field is plotted. Axes normalised to λ_0

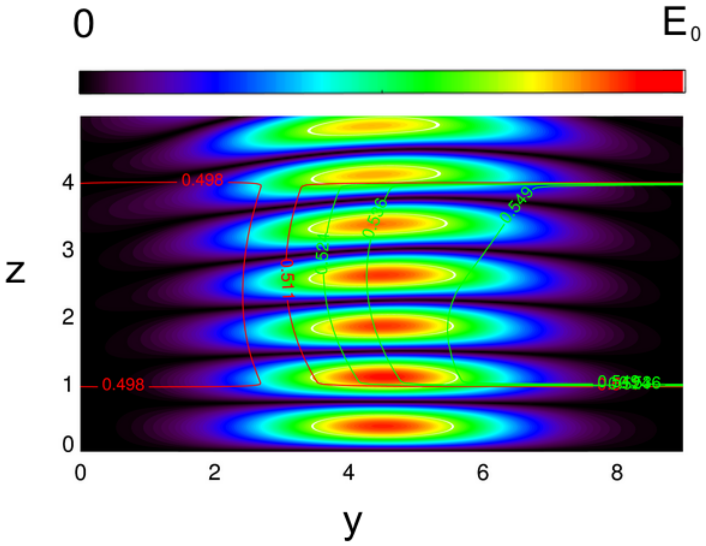

Figure 6.9: yz-plane view of turbulent scattering simulation with $\rho_i = 2\lambda_0$. Absolute E-field values of microwave beam plotted in background; density perturbation contours in foreground (green - positive, red - negative). Axes normalised to λ_0

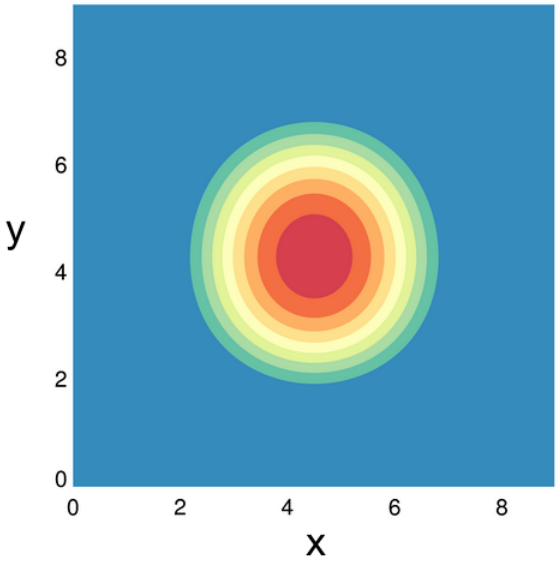

Figure 6.10: Backplane (xy) view of turbulent scattering simulation with $\rho_i = 2\lambda_0$. Time-averaged value of E-field is plotted. Axes normalised to λ_0

These results were obtained for a range of ρ_i (and thus s). At each value, a set of simulations were carried out each using separate turbulent snapshots, each sufficiently different from the last to approximate randomness. This gives a dataset for analysis.

At the backplane, a value of χ^2 is calculated for each of 7 snapshots at each value of ρ_i:

$$\chi^2 = \sum_x \frac{(E - E_{\text{flat}})^2}{E_{\text{flat}}} \tag{6.5}$$

where E_{flat} is the time-averaged electric field distribution for a beam propagating through an unperturbed plasma. This provides a measure of the difference between the scattered and unscattered distributions (see Figure 6.11).

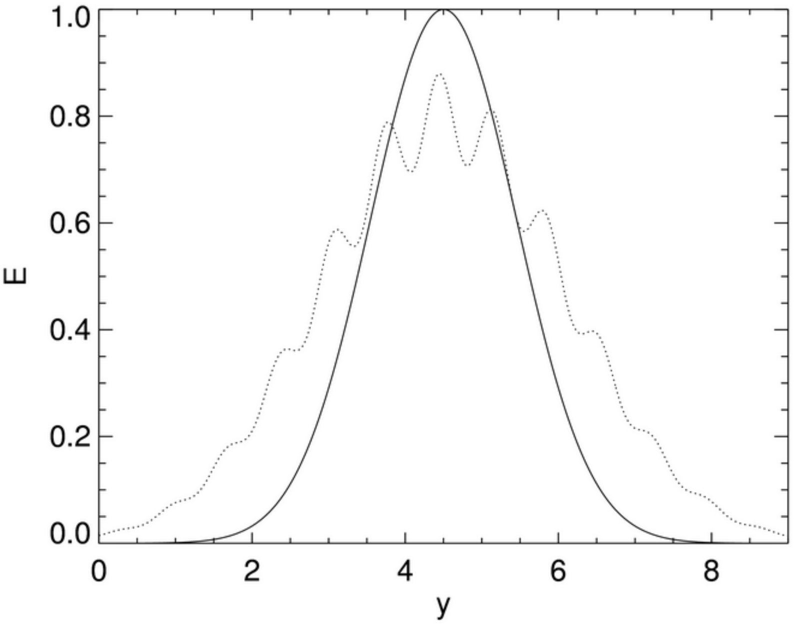

Figure 6.11: Sketch of line plot at centre of backplane showing two time-averaged E-field distributions; unperturbed distribution E_{flat} (solid line) and scattered distribution E (dotted line).

χ^2 is then averaged across all snapshots. This provides us with a measure of the shift in beam shape away from that observed in homogeneous plasma; a higher average χ^2 corresponds to greater defocusing (although, in principle, it could also correspond to greater focusing, observation of the beam pattern showed a spreading rather than focusing effect in all cases).

This averaged value is plotted in Figure 6.12, with χ^2 normalised to its maximum value.

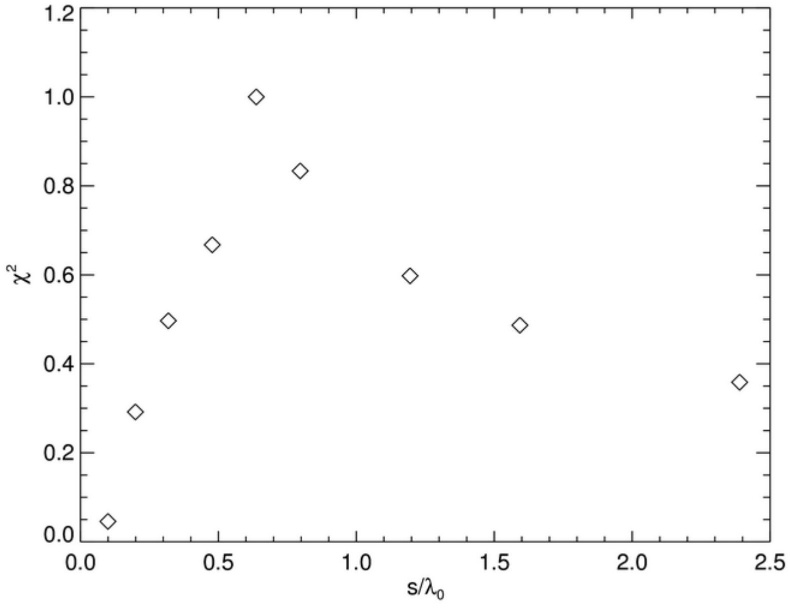

Figure 6.12: χ^2 plotted against structure size normalised to vacuum wavelength s/λ_0

Sufficient timeslices have been used that the error bars on this graph are small.

A peak in χ^2 is thus observed where structure size $s = 0.64\lambda_0$; that is, the effect of turbulence on microwave scattering is greatest in this case. Away from this scale length, χ^2 decreases. If plotted with a logarithmic x-axis as in Figure 6.13, this fall-off in either direction appears to be linear.

It is expected that turbulent structures with a size comparable to the vacuum wavelength will have the greatest defocusing effect on a beam, and this is borne out by this result. However, the greatest effect appears when the size is somewhat

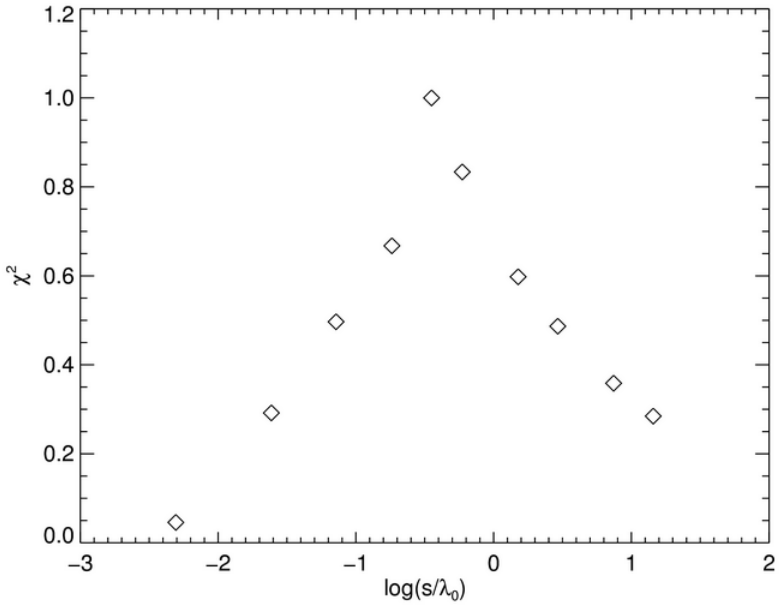

Figure 6.13: χ^2 plotted against logarithm of structure size normalised to vacuum wavelength $\log(s/\lambda_0)$

less than a whole wavelength, giving a distribution which is noticeably skewed away from (s/λ_0) being unity.

The width at which χ^2 falls to 50% of its maximum value is $1.8\log(s/\lambda_0)$. This gives a quantitative measure of the defocusing effect on a microwave beam that would be expected from a turbulent layer of known structure size, allowing an estimation of the likely impact on a diagnostic or heating system.

A characterisation of the interactions between microwave beams in plasma with regions of realistic turbulence has thus been made across a range of turbulent scale lengths. The χ^2 distribution shown in Figure 6.13 is valid for a layer several wavelengths thick of low amplitude turbulence; an increase in the severity of the defocusing effect can be expected at some of the higher turbulent amplitudes known to be present in the tokamak edge, and for thicker layers. However, although the maximum value of χ^2 may be higher in these cases, a similar distribution is expected. The dependence of its skew on these profile parameters is not known.

A broader parameter scan is left to future work at this stage (discussed in more detail in the following chapter, alongside other topics). This will allow this characterisation to be extended.

Chapter 7

Conclusions and future work

In this thesis, a set of related problems involving the propagation of a microwave beam through plasma inhomogeneity were simulated for the first time; these involved both a single plasma filament and a region of coherent plasma turbulence. The effects of this inhomogeneity were quantified across a broad range of parameters and their expected ramifications for experimental applications of high-frequency EM radiation in tokamak plasmas discussed. Strong scattering and defocusing effects were observed which could substantially affect the performance of microwave emission diagnostics, current drive and heating on tokamaks.

In order to carry out these simulations, a new 3D full-wave cold plasma code, EMIT-3D, was developed and tested, using a new numerical scheme which is shown to be conditionally stable under all physical simulation parameters. This provides a flexible simulation framework in which to investigate a range of EM propagation, scattering and refraction phenomena in magnetised plasmas of arbitrary background electron density and magnetic field profiles. After further validation, it will also permit mode conversion studies.

These findings are summarised in this chapter, and future plans for further work using EMIT-3D are presented, including some additional algorithmic development.

7.1 Filament scattering

The results obtained in Chapter 5 show the synergistic effects of two plasma filament parameters, density and width, on the observed microwave scattering angle. While filaments with widths of several times the beam wavelength can cause large deviations at higher frequencies (e.g. a filament of Gaussian width 2.5cm, close to the mean width for MAST, will scatter a 30 GHz beam by 47°), filament density becomes an important effect at lower frequencies, even for underdense filaments (e.g. a filament of peak density 1.0×10^{18} m^{-3}, again typical for MAST, will scatter a 10 GHz beam by 26°).

It is therefore shown that filamentary plasma structures can have a significant influence on the propagation of microwaves across a broad frequency spectrum, with consequences for both electron cyclotron diagnostics and heating. Since spherical tokamaks maintain plasma densities comparable to other tokamaks with a lower magnetic field and thus have lower electron cyclotron frequencies, these effects can be particularly important. In particular, inter-ELM filaments on MAST could be a source of fluctuation for the SAMI diagnostic, although further simulation and experimental comparison are required to quantify such a link.

By comparison with IPF-FDMC, the cases in which 2D simulation is justified have been determined. For normal incidence, minimal out-of-plane scattering was observed from EMIT-3D, verifying that 2D simulation, with its reduced computational time, is valid in this case. However, for oblique incidence, which is generally the case for emission diagnostics, 3D effects become important.

7.2 Turbulence

The results obtained in Chapter 6 demonstrate the broadening effect on microwave beams caused by realistic edge turbulence. Output from a Hasegawa-Wakatani fluid model of plasma turbulence implemented in the BOUT++ code was used to initialise a set of microwave scattering simulations using EMIT-3D. The deformation away from an unperturbed beam was measured quantitatively for each case of a beam propagating through a turbulent layer.

This effect was investigated across a range of turbulent scale lengths in order to understand the role played by the structure size relative to wavelength. The defocusing effect on a beam was found to strongly depend on this parameter; the average χ^2 for a perturbed beam was found to peak for eddy sizes comparable to but somewhat smaller than the vacuum wavelength ($s = 0.64\lambda_0$); as the logarithm of the structure size either decreased or increased away from this maximum, the effect was found to decrease in an approximately linear fashion with a full width at half maximum of $1.8\log(s/\lambda_0)$.

For emission diagnostics such as SAMI, the turbulent structures with sizes of several cm (hence on the order of λ_0) present at the edge could therefore cause a significant effect, with shifts in beam shape and wavevector occurring as the edge turbulence evolves. This occurs even with a low fluctuation amplitude relative to background density. This effect can further influence the propagation of EC heating and current drive.

7.3 Future code development

EMIT-3D is an ongoing project and will continue to develop. Its 3D geometry allows the investigation of effects such as magnetic shear [30] and asymmetry of the mode conversion efficiency [56] in regimes where the density scale length $L_{n_e} = \frac{n_0}{|\nabla n_0|} \simeq \lambda_0$.

Beyond the present form of the code, there are potential future modifications which will allow investigation of a broader range of topics. Several of these paths are outlined here.

7.3.1 Incorporating background electron flows

7.3.1.1 Motivation

The algorithm heretofore presented relies on the assumption that background currents or flows do not exist within the plasma; that is, that $\mathbf{J}_0 = 0$. However, while this assumption is valid for special cases, it is not generally so; a tokamak plasma typically has a significant toroidal current, even in edge regions, and may contain electron flows.

In some cases, a background current is necessary simply for self-consistency within the model; if a non-homogeneous background magnetic field with a finite curl is present, $\mathbf{J}_0$ is required in order to satisfy the zero-order Ampère's Law:

$$\mathbf{J}_0 = \frac{\nabla \times \mathbf{B}_0}{\mu_0} \tag{7.1}$$

If the magnetic field scale length $L_s \gg \lambda_0$, this term is too small to affect a propagating wave and can be neglected. However, for background magnetic field profiles with strong spatial variations such that $L_s \simeq \lambda_0$, it becomes necessary.

One example of such a case requiring a $\mathbf{J}_0$ term for self-consistency is the simulation of the effect of magnetic shear on mode conversion. This was predicted analytically by Cairns and Lashmore-Davies [30] to have a significant effect on the mode conversion efficiency when the magnetic shear scale length approaches the density scale length. Since strongly sheared fields can be present at the tokamak edge, this effect is of significant interest and thus it is desirable to have the option of including a background current in EMIT-3D if it is to be verified with full-wave simulation.

Further to this, the presence of electron flows in the tokamak plasma can also give rise to a $\mathbf{J}_0$. Work by Jia and Gao [79] indicates that this effect can also strongly influence mode conversion efficiency.

In this section, the numerical method developed in Chapter 4 is modified to include $\mathbf{J}_0$. This new modification could be directly implemented in EMIT-3D in order to carry out full-wave simulations to investigate these effects.

7.3.1.2 Algorithmic details

If $\mathbf{J}_0 \neq 0$, the linearised first-order equation of electron motion becomes:

$$\frac{\partial \mathbf{J}_1}{\partial t} = \varepsilon_0 \omega_{pe}^2 \mathbf{E}_1 - \omega_{ce} \mathbf{J}_1 \times \hat{\mathbf{b}}_0 - \frac{e}{m} \mathbf{J}_0 \times \mathbf{B}_1 - \nu \mathbf{J}_1 \tag{7.2}$$

and hence the newly arisen $\mathbf{J}_0 \times \mathbf{B}_1$ term must be incorporated into the FDTD model. In order to include this term, the methodology derived in Chapter 4 must be modified.

First, this equation is rewritten in matrix form as before. Subscripts are dropped so that $\mathbf{J}, \mathbf{E}, \mathbf{B}$ are all first-order quantities.

$$\dot{\mathbf{J}}(t) = P\mathbf{J}(t) + \varepsilon_0 \omega_{pe}^2 \mathbf{E}(t) + R\mathbf{B}(t) \tag{7.3}$$

where

$$P = \begin{bmatrix} -\nu & -b_z\omega_{ce} & b_y\omega_{ce} \\ b_z\omega_{ce} & -\nu & -b_x\omega_{ce} \\ -b_y\omega_{ce} & b_x\omega_{ce} & -\nu \end{bmatrix} \quad , \quad \hat{\mathbf{b}}_0 = (b_x, b_y, b_z)$$

and

$$R = \begin{bmatrix} 0 & -J_{0,z} & J_{0,y} \\ J_{0,z} & 0 & -J_{0,x} \\ -J_{0,y} & J_{0,x} & 0 \end{bmatrix}$$

This can now be integrated as before with the use of an integrating factor:

$$\begin{aligned}\mathbf{J}(t) &= e^{P(t-t_0)}\mathbf{J}(t_0) + \varepsilon_0\omega_{pe}^2\int_{t_0}^{t} e^{P(t-\tau)}\mathbf{E}(\tau)d\tau \\ &+ \int_{t_0}^{t} e^{P(t-\tau)}R\mathbf{B}(\tau)d\tau \end{aligned} \tag{7.4}$$

Following the previous derivation, we wish to obtain a discretised form by removing both $\mathbf{E}$ and $\mathbf{B}$ from their convolutions. This can be carried out as before using the midpoint approximations that $\mathbf{E}, \mathbf{B}$ are constant over the interval $[t_0, t]$:

$$\begin{aligned}\mathbf{J}^{n+1} &= e^{P\Delta t}\mathbf{J}^{n} + \varepsilon_0\omega_{pe}^2 P^{-1}(e^{P\Delta t} - \mathbf{I})\mathbf{E}^{n+1/2} \\ &+ P^{-1}(e^{P\Delta t} - \mathbf{I})R\mathbf{B}^{n+1/2} \end{aligned} \tag{7.5}$$

However, since $\mathbf{B}$ is calculated in phase with $\mathbf{J}$, i.e. at $t = (0, 1, 2, ...)\Delta t$, a value of $\mathbf{B}$ at $t = (\frac{1}{2}, \frac{3}{2}, \frac{5}{2}, ...)\Delta t$ is not available.

A solution to this is to replace $\mathbf{B}^{n+1/2}$ with an average of $\mathbf{B}^{n}$ and $\mathbf{B}^{n+1}$, giving the discretised form:

$$\begin{aligned}\mathbf{J}^{n+1} &= e^{P\Delta t}\mathbf{J}^{n} + \varepsilon_0\omega_{pe}^2 P^{-1}(e^{P\Delta t} - \mathbf{I})\mathbf{E}^{n+1/2} \\ &+ P^{-1}(e^{P\Delta t} - \mathbf{I})R(\frac{\mathbf{B}^{n} + \mathbf{B}^{n+1}}{2}) \end{aligned} \tag{7.6}$$

This update can be carried out without the code's memory requirements being increased since storage of multiple steps is not required simultaneously. A value of current density $\mathbf{J}^{\text{int}}$, which is intermediate between $\mathbf{J}^n$ and $\mathbf{J}^{n+1}$, is introduced and these equations obtained:

$$\begin{aligned} \mathbf{J}^{\text{int}} = e^{P\Delta t}\mathbf{J}^n &+ \varepsilon_0\omega_{pe}^2 P^{-1}(e^{P\Delta t} - \mathbf{I})\mathbf{E}^{n+1/2} \\ &+ \frac{1}{2}P^{-1}(e^{P\Delta t} - \mathbf{I})R\mathbf{B}^n \end{aligned} \tag{7.7}$$

$$\mathbf{J}^{n+1} = \mathbf{J}^{\text{int}} + \frac{1}{2}P^{-1}(e^{P\Delta t} - \mathbf{I})R\mathbf{B}^{n+1} \tag{7.8}$$

These equations can therefore be incorporated into the standard FDTD update algorithm as follows (cf. Subsection 4.2.2):

1. Update J components from $t = n\Delta t$ to intermediate value J^{int} using Equation 7.7
2. Update B components from $t = n\Delta t \Rightarrow (n+1)\,\Delta t$ using Equations 3.20—3.22
3. Update J components from intermediate value J^{int} to $t = (n+1)\,\Delta t$ using Equation 7.8
4. Send and receive B components using MPI
5. Update E components from $t = \left(n + \frac{1}{2}\right)\Delta t \Rightarrow \left(n + \frac{3}{2}\right)\Delta t$ using Equations 3.23—3.25
6. Apply current source term
7. Send and receive E components using MPI

The numerical development described here was carried out during this PhD project; however, its implementation into the code remains future work.

7.3.2 Warm plasma terms

The full O-X-B conversion process is of interest for future simulation work, with applications to EBW heating and current drive as well as diagnostics. To simulate Bernstein modes, a cold plasma model is not sufficient and warm terms must be included. The approach used by Köhn *et al.* (2008) [49], in which a correction is added to the dielectric tensor of a cold-plasma model, is limited to investigating EBWs near the upper hybrid resonance since it relies on a low-order expansion [50]. To move away from this region, it would be necessary to expand terms of the hot plasma dispersion relation to arbitrary order; it is not clear that it is possible to do so in the case of an FDTD code.

An alternative approach may be necessary to allow Bernstein waves to propagate into the core of the plasma. It is likely that a fully kinetic method such as a particle-in-cell (PIC) code may be required; PIC codes have already seen success in simulation of astrophysical B-X conversion [80] and have much promise for application to fusion plasmas when used in conjunction with massively parallel computing.

7.3.3 Integration

The integration of the FDTD code EMIT-3D with another numerical method such as ray/beam tracing could result in powerful optimisation and so the development of a suite of complementary codes is a long-term goal for this project.

The two codes could operate together in order to divide up a single simulation into the numerical work most appropriate for each. For example, a 3D beam tracing code could track the trajectory of a Gaussian beam through underdense plasma, in regions where gradients in refractive index are shallow enough for the WKB approximation to be valid. When a cutoff is approached and full-wave treatment becomes necessary, the wavevector $\mathbf{k}$ of each ray in the beam can be provided to the

FDTD module and a matching condition applied. The simulation can then continue using the more computationally expensive FDTD module.

For a discussion of this approach in the ICRF regime see Petrov et al. [81]; future application to simulations of EC waves is a promising area for development of EMIT-3D.

References

[1] J.D. Lawson. *Proc. Phys. Soc. B*, 70:6, 1957.

[2] J. Wesson. *Tokamaks (Third edition)*. Clarendon Press, Oxford, 2004.

[3] A. Sykes et al. *Plasma Phys. Control. Fusion*, 39:B247, 1997.

[4] Y-K.M. Peng and D.J. Strickler. *Nucl. Fusion*, 26:769, 1986.

[5] B. Lloyd et al. *Plasma Phys. Control. Fusion*, 46:B477, 2004.

[6] F. Wagner et al. *Phys. Rev. Lett.*, 49:1408, 1982.

[7] F. Wagner et al. *Phys. Rev. Lett.*, 53:1453, 1984.

[8] M. Greenwald et al. *Nucl. Fusion*, 37:793, 1997.

[9] A. Loarte et al. *Phys. Scripta*, T128:222, 2007.

[10] G. Federici, A. Loarte, and G. Strohmayer. *Plasma Phys. Control. Fusion*, 45:1523, 2003.

[11] D.A. D'Ippolito, J.R. Myra, and S.J. Zweben. *Phys. Plasmas*, 18:060501, 2011.

[12] N. Ben Ayed et al. *Plasma Phys. Control. Fusion*, 51:035016, 2009.

[13] S.J. Zweben et al. *Plasma Phys. Control. Fusion*, 49:S1, 2007.

[14] B.D. Scott. *New J. Phys.*, 4:52.1, 2002.

[15] D. Chenna Reddy and T. Edlington. *Rev. Sci. Instrum.*, 67:462, 1996.

[16] H. Park et al. *Rev. Sci. Instrum.*, 75:3787, 2004.

[17] G.S. Yun et al. *Rev. Sci. Instrum.*, 81:10D930, 2010.

[18] J.E. Boom et al. *Nucl. Fusion*, 51:103039, 2011.

[19] V.F. Shevchenko, R.G.L. Vann, S.J. Freethy, and B.K. Huang. *J. Instrum.*, 7:P10016, 2012.

[20] V.F. Shevchenko, M. De Bock, S.J. Freethy, A.N. Saveliev, and R.G.L. Vann. *Fusion Sci. Technol.*, 59:663, 2011.

[21] K.G. Budden. *Radio Waves in the Ionosphere.* Cambridge University Press, Cambridge, 1961.

[22] K. Davies. *Ionospheric Radio.* Short Run Press Ltd., Exeter, 1990.

[23] E.V. Appleton. *Wireless Section, P. I. Elec. Eng.*, 7:257, 1932.

[24] W.M. Hooke, F.H. Tenney, M.H. Brennan, H.M. Hill Jr, and T.H. Stix. *Phys. Fluids*, 4:1131, 1961.

[25] R. Fitzpatrick. *The Physics of Plasmas.* Lulu, 2008.

[26] T.H. Stix. *Waves in Plasmas.* Springer-Verlag, New York, 1992.

[27] P.C. Clemmow and J.P. Dougherty. *Electrodynamics of Particles and Plasmas.* Addison-Wesley, Reading, MA, 1990.

[28] C. Laviron, A. J. H. Donné, M. E. Manso, and J. Sanchez. *Plasma Phys. Control. Fusion*, 38:905, 1996.

[29] R.J. Akers et al. *Nucl. Fusion*, 40:1223, 2000.

[30] R.A. Cairns and C.N. Lashmore-Davies. *Phys. Plasmas*, 7:4126, 2000.

[31] V.F. Shevchenko. *Plasma Phys. Rep.*, 26:1000, 2000.

[32] I.B. Bernstein. *Phys. Rev.*, 109:10, 1958.

[33] H.P. Laqua et al. *Phys. Rev. Lett.*, 78:3467, 1997.

[34] J. Urban et al. *Nucl. Fusion*, 51:083050, 2011.

[35] R. Prater. *Phys. Plasmas*, 11:2349, 2004.

[36] H.J. Hartfuss. *Plasma Phys. Control. Fusion*, 40:A231, 1998.

[37] W. Pfister R.J. Marcou and J.C. Ulwick. *J. Geophys. Res.*, 63:315, 1958.

[38] B.D. McVey. *Nucl. Fusion*, 19:461, 1979.

[39] F. de Luca and C. Maroli. *J. Plasma. Phys.*, 20:299, 1978.

[40] J. Urban et al. *J. Plasma Fusion Res. Ser.*, 8:1153, 2009.

[41] R.V. Budny et al. *Nucl. Fusion*, 52:023023, 2012.

[42] J.C. Wright et al. *Phys Plasmas*, 11:2473, 2004.

[43] S.A. Cummer. *IEEE Trans. Antennas Propag.*, 45:392, 1997.

[44] R.J. Luebbers, F. Hunsberger, and K.S. Kunz. *IEEE Trans. Antennas Propag.*, 39:29, 1991.

[45] D.F. Kelley and R.J. Luebbers. *IEEE Trans. Antennas Propag.*, 44:792, 1996.

[46] L. Song, Z. Shuangying, and L. Shaobin. *Plasma Sci. Technol.*, 7:3122, 2005.

[47] J.H. Irby, S. Horne, I.H. Hutchinson, and P.C. Stek. *Plasma Phys. Control. Fusion*, 35:601, 1993.

[48] L. Xu and N. Yuan. *IEEE Antennas Wireless Propag. Lett*, 5:335, 2006.

[49] A. Köhn et al. *Plasma Phys. Control. Fusion*, 50:085018, 2008.

[50] A.K. Ram and S.D. Schultz. *Phys. Plasmas*, 7:4092, 2000.

[51] C. Tsironis, T. Samaras, and L. Vlahos. *IEEE Trans. Antennas Propag.*, 56:2988, 2008.

[52] A. Taflove and S.C. Hagness. *Computational Electrodynamics: The Finite-Difference Time Domain Method.* Artech House Publishers, Boston, MA, 2000.

[53] K.S. Yee. *IEEE Trans. Antennas Propag.*, 14:302, 1966.

[54] J.B. Schneider. Understanding the finite-difference time-domain method, 2010.

[55] A. Kyriacou. Yeecell01.jpg, December 2008.

[56] E.D. Gospodchikov, A.G. Shalashov, and E.V. Suvorov. *Plasma Phys. Control. Fusion*, 48:869, 2006.

[57] J-P Bérenger. *J. Comput. Phys*, 114:185, 1994.

[58] W.C. Chew and W.H. Weedon. *Microw. Opt. Techn. Let.*, 7:599, 1994.

[59] J.G. Charney, R. Fjörtoft, and J. von Neumann. *Tellus*, 2:237, 1950.

[60] J.A. Pereda et al. *IEEE Trans. Microw. Theory Techn.*, 49:377, 2001.

[61] J.R. Myra and D.A. D'Ippolito. *Phys. Plasmas*, 17:102510, 2010.

[62] C. Tsironis et al. *Phys Plasmas*, 16:112510, 2009.

[63] K. Hizanidis et al. *Phys. Plasmas*, 17:022505, 2010.

[64] A.K. Ram, K. Hizanidis, and Y. Kominis. *Phys. Plasmas*, 17:022505, 2010.

[65] V.V. Bulanin et al. *Tech. Phys. Lett.*, 37:340, 2011.

[66] A. Kirk et al. *Plasma Phys. Control. Fusion*, 48:B433, 2006.

[67] J. Boedo et al. *Phys. Plasmas*, 8:4826, 2001.

[68] D.H.J. Goodall. *J. Nucl. Mater.*, 111 — 112:11, 1982.

[69] S.J. Zweben and S.S. Medley. *Phys. Fluids B*, 1:2058, 1989.

[70] S.J. Zweben et al. *Phys. Plasmas*, 9:1981, 2002.

[71] R.J. Maqueda et al. *Rev. Sci. Instrum.*, 72:931, 2001.

[72] A. Kirk et al. *Phys. Rev. Lett.*, 92:245002, 2004.

[73] A. Kirk et al. *Phys. Rev. Lett.*, 96:185001, 2006.

[74] D.L. Rudakov et al. *Nucl. Fusion*, 45:1589, 2005.

[75] R.A. Moyer, J.W. Cuthbertson, T.E. Evans, G.D. Porter, and J.G. Watkins. *J. Nucl. Mater.*, 241-243:633, 1997.

[76] E.V. Sysoeva et al. *AIP Conf. Proc.*, 1580:522, 2014.

[77] B.D. Dudson, M.V. Umansky, X.Q. Xu, P.B. Snyder, and H.R. Wilson. *Comput. Phys. Commun.*, 180:1467, 2009.

[78] R. Numata, R. Ball, and R.L. Dewar. *Phys. Plasmas*, 14:102312, 2007.

[79] G-Z. Jia and Z. Gao. *Phys. Plasmas*, 18:104511, 2011.

[80] S. Saito and J.I. Sakai. *Astrophys. J.*, 616:L179–L182, 2004.

[81] Yu. Petrov, A. Bécoulet, and I. Monakhov. *Phys. Plasmas*, 7:911, 2000.